# ION-COUPLING DURING COLLISIONLESS MAGNETIC RECONNECTION: CAUSES AND CONSEQUENCES

by

Prayash Sharma Pyakurel

A dissertation submitted to the Faculty of the University of Delaware in partial fulfillment of the requirements for the degree of Doctor of Philosophy in Physics

Summer 2019

# ION-COUPLING DURING COLLISIONLESS MAGNETIC RECONNECTION: CAUSES AND CONSEQUENCES

by

Prayash Sharma Pyakurel

Approved: _____
Edmund R. Nowak, Ph.D.
Chair of the Department of Physics and Astronomy

Approved: _____
John Pelesko, Ph.D.
Dean of the College of Arts and Sciences

Approved: _____
Douglas J. Doren, Ph.D.
Interim Vice Provost for Graduate and Professional Education and
Dean of the Graduate College

I certify that I have read this dissertation and that in my opinion it meets the academic and professional standard required by the University as a dissertation for the degree of Doctor of Philosophy.

Signed: _____

Michael Shay, Ph.D.
Professor in charge of dissertation

I certify that I have read this dissertation and that in my opinion it meets the academic and professional standard required by the University as a dissertation for the degree of Doctor of Philosophy.

Signed: _____

William Matthaeus, Ph.D.
Member of dissertation committee

I certify that I have read this dissertation and that in my opinion it meets the academic and professional standard required by the University as a dissertation for the degree of Doctor of Philosophy.

Signed: _____

Bennett Maruca, Ph.D.
Member of dissertation committee

I certify that I have read this dissertation and that in my opinion it meets the academic and professional standard required by the University as a dissertation for the degree of Doctor of Philosophy.

Signed: _____

James MacDonald, Ph.D.
Member of dissertation committee

I certify that I have read this dissertation and that in my opinion it meets the academic and professional standard required by the University as a dissertation for the degree of Doctor of Philosophy.


Signed: _____

Paul Cassak, Ph.D.
Member of dissertation committee

# DEDICATION

To my Sister - Roshani Sharma.

## ACKNOWLEDGEMENTS

First, I would like to express my gratitude to my advisor Professor Michael Shay. This would not have been possible without your help and guidance. Second, I thank my dissertation committee members - Professors Matthaeus, Maruca, MacDonald and Cassak - for carefully reviewing this dissertation. Third, I am indebted to my girlfriend-Graciela Perez for her love and support. Lastly, to all the UD professors who have made physics fun and to all the friends that always make it better. Thank you!

# TABLE OF CONTENTS

**Chapter**

# LIST OF TABLES

# LIST OF FIGURES

# ABSTRACT

Magnetic reconnection efficiently converts magnetic energy into particle kinetic energy. The energy release by magnetic reconnection is important for a wide range of systems, such as astrophysical, laboratory and space plasmas. The main focus of this thesis is to study and understand the magnetic reconnection phenomena found in Earth's magnetosphere. With the aid of supercomputers and massively multi-parallel particle-in-cell simulations, magnetic reconnection is explored from first-principle calculations. First, in anti-parallel reconnection, the propagation and damping of Hall magnetic fields are consistent with the linear Landau damping associated with kinetic Alfvén waves (KAW). The findings are extrapolated to the parameters observed in the Earth's magnetotail and the solar corona and their implications are presented. Second, we perform simulations motivated by Magnetospheric MultiScale (MMS) Mission observations in the Earth's magnetosheath. We study the coupling of ions during collisionless magnetic reconnection with simulations initialized with the parameters observed by MMS. In large guide-field and high-beta plasmas, we find that the transition from ion-coupled to electron-only reconnection is gradual as the reconnection domain size decreases. The scaling of the ion outflow velocity with exhaust width during the electron-only to ion-coupled transition is found to be consistent with a theoretical model of a newly reconnected field line. For fully ion-coupled reconnection, we find that magnetic bubble length scales of tens of ion inertial lengths are required. Third, we extend this study of electron-only reconnection to three-dimensions (3D). It is found that magnetic reconnection in 3D enhances the parallel electric field, allowing faster reconnection than the traditional 2.5D configuration. The simple Sweet-Parker scaling analysis is extended in the 3D configuration to explain the net mass flux loss in the direction perpendicular to the reconnection plane, which suggests a new and simple

mechanism for the faster magnetic reconnection typically observed in the turbulent magnetosheath.

# Chapter 1

# INTRODUCTION

## 1.1 Magnetic Reconnection

Magnetic reconnection is a process that is ubiquitous throughout the universe in ionized gases containing embedded magnetic fields [Burch et al., 2019]. This phenomenon covert magnetic energy to kinetic energy of charged particles. They have been associated with phenomena such as solar flares and auroras [Hones, 1980, Nishida et al., 1981, Baker et al., 1996, Amari et al., 2014]. Magnetic reconnection efficiently releases magnetic energy accumulated suddenly or over time.

The origins of magnetic reconnection are tied to the study of the space weather system. The space weather system consists of the Sun and the planets that interact with the Sun's continuous stream of plasma known as the solar wind. The study of space weather begins with the study of the interior of the Sun. The release of the energy from the Sun's hot core makes it way out into the interplanetary space. Here at Earth, we eventually receive a small amount of the released plasmas. This has a dramatic effect on our atmosphere and the space environment we inhabit. A historically well-known observation of disturbances in Earth's atmosphere due to solar activity is the "Carrington event" [Carrington, 1859, Hodgson, 1859]. The geomagnetic storm disrupted telegraph communications and auroral precipitation was seen as far south as Cuba [Cliver and Svalgaard, 2004]. The exact cause of the solar flares remained elusive for long after the Carrington event. In 1947, Giovanelli observed that solar flares had collocated oppositely aligned magnetic fields associated with them [Giovanelli, 1947]. James Dungey proposed that the null point was a topological change of magnetic fields where the magnetic field strength vanishes and allows oppositely aligned magnetic

field lines to reconnect [Dungey, 1953, 1958]. Around the same time, P.A. Sweet at a Stockholm symposium in 1956 proposed that the initial conditions necessary for the null-points were governed by plasma dynamics far away from the null points [Sweet, 1958]. E.N. Parker incorporated ideas presented by Sweet at the symposium and thereafter proposed a well known steady state scaling analysis of what is called Sweet-Parker reconnection [Parker, 1957]. Although a solid framework of magnetic reconnection was established, Harry Petschek came up with another explanation that released magnetic energy on a much faster time scale. The Sweet-Parker scaling analysis of magnetic reconnection gives time scales of energy to be released much faster than simple diffusion. However, it still did not give time scales of minutes-hours generally observed. In this model, microscopic Sweet-Parker layer is embedded in a much larger magnetic reconnection region, where the inflowing plasmas are processed away from the dissipation region allowing the plasma to accelerate in the outflowing region [Petschek, 1964]. Outside the diffusion region, magnetic energy is converted due to the formation of a standing slow shock rather than diffusion. A schematic difference between classical Sweet-Parker reconnection and Petschek reconnection is shown in Figure 1.1. Using 2D incompressible resistive magnetohydrodynamics (MHD), Dieter Biskamp [Biskamp, 1986] numerically showed that Syrovatsky's [Syrovatsky, 1971] theory of neutral current sheet formation was generally in agreement with computer simulations rather than Petschek's slow shock model. Petschek reconnection on the other hand only persists so long as resistivity is enhanced locally, also dubbed as anomalous resistivity [Ugai and Tsuda, 1977].

There has been progress in understanding the generation of fast reconnection when non-MHD terms are included to break the frozen-in constraint. The non-MHD Hall term decouples electrons and ions. The dispersive behavior of the Hall term gives the rate of energy release during magnetic reconnection to be fast enough without the need to invoke anomalous resistivity [Aydemir, 1992, Mandt et al., 1994, Horiuchi and Sato, 1994, Biskamp et al., 1995, Ma and Bhattacharjee, 1996, Shay et al., 1998, Birn
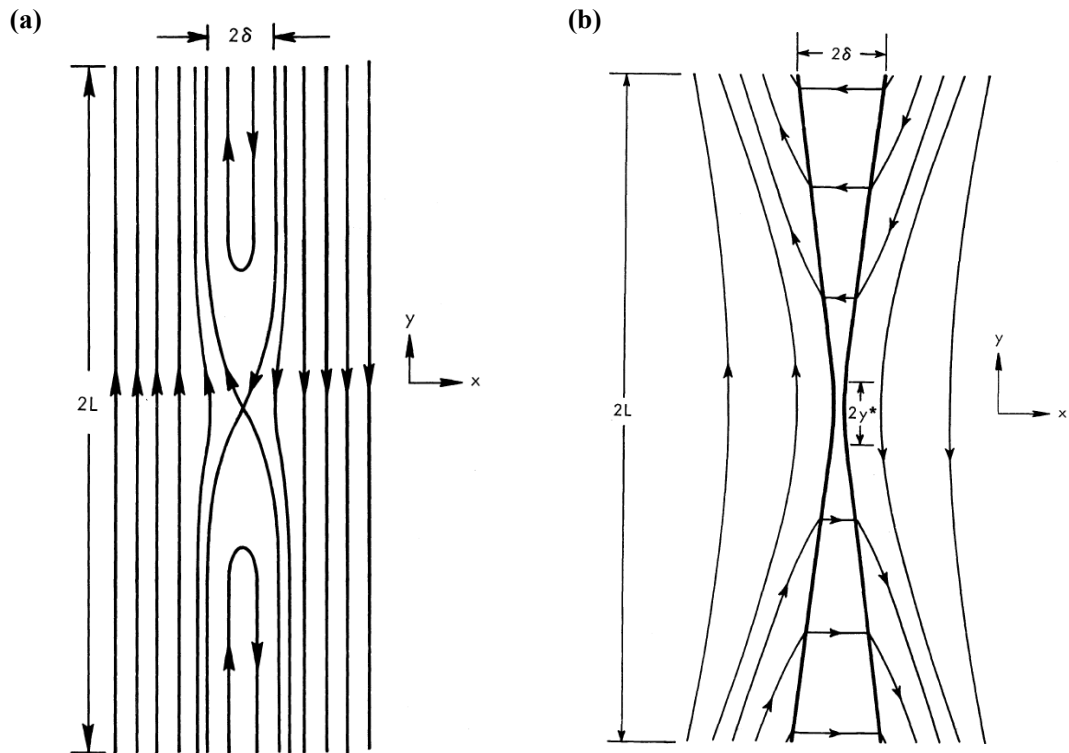
**Figure 1.1:** (a) Sweet-Parker magnetic reconnection: Oppositely aligned magnetic field lines reconnect at the x-point driving plasma in the $\pm$ y-direction. (b) Petschek reconnection: Plasmas are driven by the oppositely reconnected magnetic field line with standing slow shocks (shown by thick black lines) outside the diffusion region. The length of the diffusion region is $2y^*$. It is much shorter than in Sweet-Parker reconnection. Reprinted from Petschek [1964].
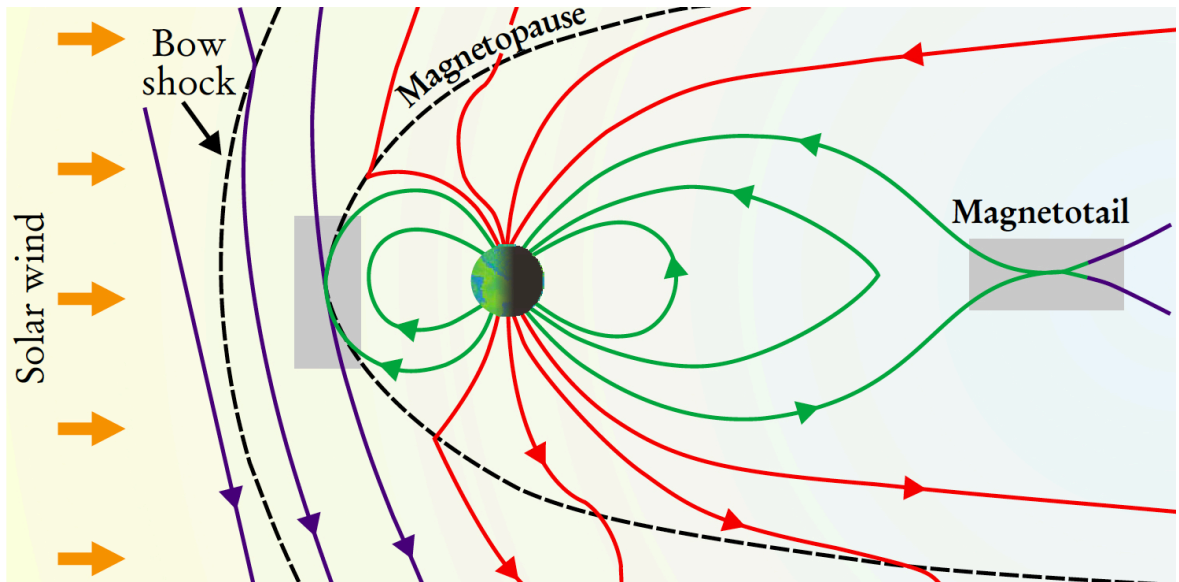
**Figure 1.2:** The shaded rectangular boxes show the location of magnetic reconnection. The Sun's magnetic fields shown in blue lines reconnect with Earth's magnetic fields (green lines) at the magnetopause (the inner dashed black line boundary). On the night side, Earth's magnetic fields are pushed together to form magnetic reconnection in the magnetotail. Not drawn to scale. Reprinted from Day [2001].

et al., 2001, Shay et al., 2001a][1].

## 1.2   Observations of Magnetic Reconnection

As mentioned in the previous section, the Sun is the main driver of the space weather. The volatility of the sun ejecting plasma is tied to its periodic solar cycle that occurs over a roughly 11 year period. Even in its quiet times, the Sun expels hot high-speed charged particles. Roughly, the Sun's magnetic field polarity changes about every 11 years. However, the solar wind contains a lot of transient structures which change the magnitude and direction of magnetic fields on shorter time scales (minutes to hours) at Earth. This has profound effect on Earth's magnetospheric

---

[1] There have been other numerous studies where the Hall term is either absent [Bessho and Bhattacharjee, 2005, Hesse and Zenitani, 2007, Daughton and Karimabadi, 2007, Swisdak et al., 2008] or inactive [Liu et al., 2014, Stanier et al., 2015, Cassak et al., 2015]. These studies also consistently find fast reconnection.

environment. Earth's magnetosphere is illustrated as in Figure 1.2 for southward interplanetary magnetic fields. One of the first in-situ observations of magnetopause reconnection was recorded by *ISEE* satellites (spacecraft 1 and 2) [Paschmann et al., 1979], an event measured in a region in the left gray rectangular box in Figure 1.2. In the magnetotail (right rectangular box in Figure 1.2), possible magnetic reconnection spacecraft observations were made a few years earlier [Hones et al., 1976, Frank et al., 1976]. *In-situ* observations in the magnetopause of both bi-directional outflow jets from magnetic reconnection was found in 1998 using three spacecraft - The Equator-S, Geotail and Wind [Phan et al., 2000]. A year later in 1999, in-situ observations of bi-directional jets in the magnetotail were verified too [Oieroset et al., 2001]. These observations confirmed the existence of the ion-diffusion region and Hall-currents associated to fast reconnection which further suggests that anomalous resistivity does not play any role, rather the particles are demagnetized by the gyro motions in spaces with low magnetic field strengths and large gradients in the magnetic fields [Nagai et al., 2001]. In recent years, Cluster observations have been instrumental in measuring reconnection events at spatial and temporal scales ranging from electron scales up to 1au $\sim$ 150 million kilometers. A detailed structure of the electron diffusion region was captured by Cluster [Phan et al., 2007]. Ion diffusion and separatrix regions were reported in Vaivads et al. [2004], and Khotyaintsev et al. [2006] and mechanisms of particle acceleration were presented in Wygant et al. [2005], Cattell et al. [2005], Drake et al. [2006], Imada et al. [2007], and Chen et al. [2008]. One key limitation of *in-situ* spacecraft observation is the availability of measurement only at a few spatial points. Hence, it is necessary to use other measurement techniques to see the effects of reconnection. Using Cluster and images of aurora, Frey et al. [2003] were able to show the continuity of reconnection for many hours. On the other hand, this quasi-steady reconnection does not always persist, as reconnection can have transient feature based on solar wind conditions [Khotyaintsev et al., 2004]. Magnetic reconnection between the magnetosheath and the magnetopause/magnetospheric boundary layer with
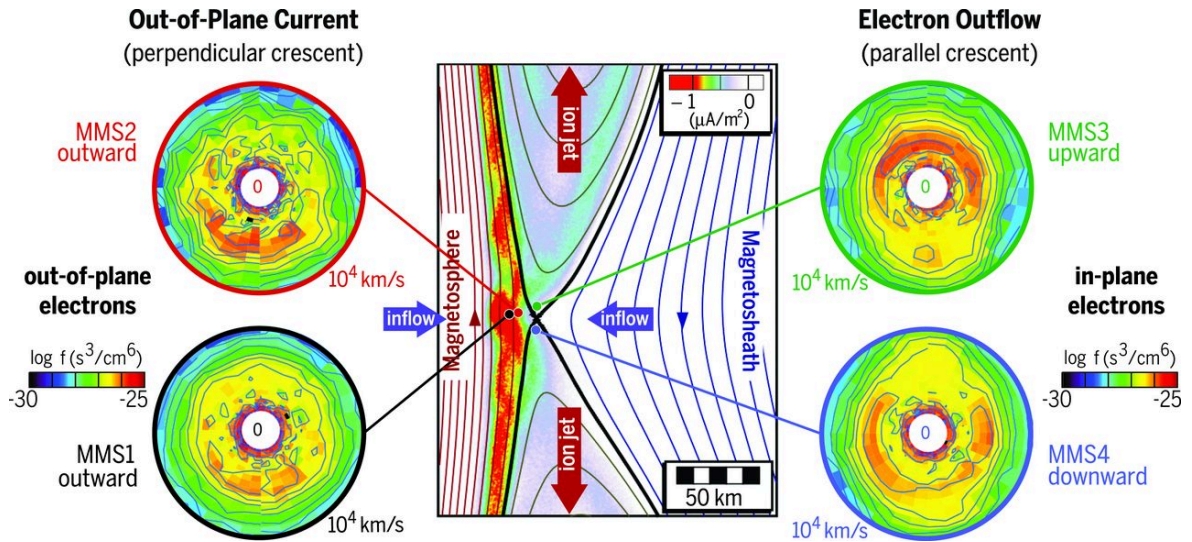
**Figure 1.3:** NASA's Magnetospheric MultiScale (MMS) Mission: The four circles show the distribution functions of electrons close to the x-line. They range from velocities 0 to $10^4$ km/s. In the center is a figure taken from a simulation initialized with parameters observed by MMS. The red vertical area within this plot is the current into the page, hence giving crescent like electron structure on the top-left circle. Similarly, circular panels on the right side are taken in the outflowing region. Reprinted from Burch et al. [2016].

guide-field has also been observed [Retinò et al., 2005] and the existence of reconnection in the solar wind using ACE, WIND and Cluster spacecraft, observed an x-line of at least 390 Earth radii [Phan et al., 2006]. A year later, it was also shown that magnetic reconnection is present in turbulent plasmas in the magnetosheath [Retinò et al., 2007, Gosling et al., 2007]. Their length scales however are much smaller (few electron skin depths) than the ones found in the solar wind. Since then, the launch of the MMS spacecraft has provided unprecedented three-dimensional measurements of electron distributions functions as time scales as short as 7.5 milliseconds and ion distribution functions with 37.5 milliseconds resolution [Burch et al., 2016, Rager et al., 2018]. In the turbulent magnetosheath, standard magnetic reconnection that couples both ions and electrons was found by Vörös et al. [2017]. Magnetic reconnection had also been suggested to play a major role in dissipation of energy at kinetic scales [Servidio et al., 2009, Retinò et al., 2007, Sundkvist et al., 2007, Haggerty et al., 2017]. In this scenario, many small-scale current sheets were expected to contain electron jetting due to reconnected magnetic field lines, namely the existence of "electron-only" magnetic reconnection. Electron-only reconnection remained elusive until it was found in the magnetosheath with no ion bi-directional jets [Phan et al., 2018]. To illustrate MMS's measurement capability, in Figure 1.3 electron distribution functions close to the x-line are shown. Crescent structure of the electron distribution functions in spacecraft observations had never been previously observed and could be inferred only from particle-in-cell simulations [Hesse et al., 2014][2].

## 1.3    Frozen-in Plasma

In a perfectly conductive plasma, the magnetic lines of force are attached to the ionized gas and actively participate in the streaming motions of charged particles[3].

---

[2] A detailed picture of meandering particle orbits is found in Speiser [1965]. An interesting feature of parallel crescent structures of the electron distribution functions is that they have yet to be found in simulations.

[3] Only valid in ideal MHD where the gyroradius tends to zero.
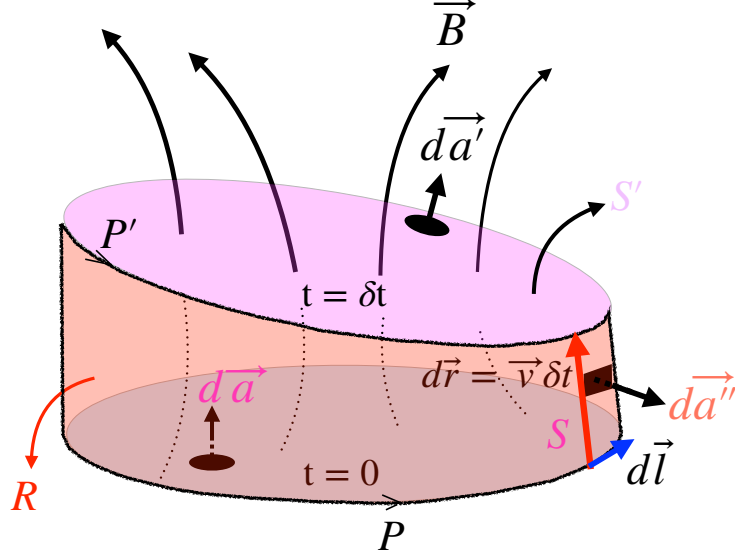
**Figure 1.4:** The loop $P$ bounding surface $S$ moves by distance $d\vec{r} = \vec{v}(\vec{r}, t)\delta t$ in time interval $\delta t$ making a tubular surface area $R$ shown by the shaded region in orange-tan.

A plasma is considered frozen-in if the magnetic flux through a closed loop within the fluid remains constant as the loop gets carried along by the fluid. According to Alfvén [Alfvén, 1942], each line of force is associated with the plasma density due to its mass to which the line of force is linked [Fermi, 1949]. Using this view, it can be shown that the propagation velocity of the Alfvén wave is $v_A = B/\sqrt{4\pi n m_i}$, where $B$ is the magnitude of magnetic field, $n$ is density and $m_i$ is ion mass. Therefore, a frozen-in plasma with bent magnetic field lines may exhibit Alfvénic propagation. The frozen-in theorem is best described by deriving it. We follow a loop moving with the plasma flow. Every point $\vec{r}(t)$ in this loop moves at a velocity $\vec{v}$, mathematically written as $\vec{v}(\vec{r}, t) = \frac{d\vec{r}}{dt}$, where $t$ is time. The total magnetic flux through the surface $S$ (loop $P$) at time $t$ is $\Phi(t) = \int_S \vec{B}(\vec{r}, t) \cdot d\vec{a}$ and the flux at a later time $t + \delta t$ through the surface $S'$ (loop $P'$) is $\Phi(t + \delta t) = \int_{S'} \vec{B}(\vec{r}, t + \delta t) \cdot d\vec{a'}$, where $S'$ is the surface of the loop after time $\delta t$ as shown in Figure 1.4 by the shaded pink region. The change in magnetic flux

through the loop is given by

$$\delta\Phi = \int_{S'} d\vec{a'} \cdot \vec{B}(t + \delta t) - \int_S d\vec{a} \cdot \vec{B}(t). \tag{1.1}$$

Using $\vec{\nabla} \cdot \vec{B} = 0$, we also have the following condition

$$-\int_S d\vec{a} \cdot \vec{B}(t + \delta t) + \int_{S'} d\vec{a'} \cdot \vec{B}(t + \delta t) + \int_R d\vec{a''} \cdot \vec{B}(t + \delta t) = 0, \tag{1.2}$$

where $R$ is the area swept by loop $P$ after time $\delta t$ as shown in Figure 1.4. Substituting Equation 1.2 in Equation 1.1, we get

$$\delta\Phi = \int_S d\vec{a} \cdot \vec{B}(t + \delta t) - \int_R d\vec{a''} \cdot \vec{B}(t + \delta t) - \int_S d\vec{a} \cdot \vec{B}(t). \tag{1.3}$$

Substituting for $\vec{da''} = -\vec{v}\delta t \times d\vec{l}$ and using a Taylor expansion about $t$, we get

$$\delta\Phi = \int_S d\vec{a} \cdot \frac{\partial \vec{B}}{\partial t} \delta t + \int \oint_P \vec{v}\delta t \times d\vec{l} \cdot \vec{B}. \tag{1.4}$$

The second term on the R.H.S of Equation 1.4 reduces to $\delta t \oint_P \vec{v} \times d\vec{l} \cdot \vec{B}$. Also note that any change in $\vec{B}$, in this term, is second order in $\delta t$. And we have,

$$\frac{\delta\Phi}{\delta t} = \int_S d\vec{a} \cdot \frac{\partial \vec{B}}{\partial t} + \oint_P \vec{v} \times d\vec{l} \cdot \vec{B}$$

$$\frac{d\Phi}{dt} = \int_S d\vec{a} \cdot \frac{\partial \vec{B}}{\partial t} - \oint_P d\vec{l} \cdot \vec{v} \times \vec{B}, \tag{1.5}$$

where we have used $\delta t \to 0 \Rightarrow \frac{\delta\Phi}{\delta t} \to \frac{d\Phi}{dt}$. The rest follows using Faraday's law and Stokes' theorem. Thus, we finally have

$$\frac{d\Phi}{dt} = -\int_S \nabla \times (c\vec{E} + \vec{v} \times \vec{B}) \cdot \hat{n} \; da \tag{1.6}$$

$$\frac{d\Phi}{dt} = \frac{d}{dt} \int_S \hat{n} \cdot \vec{B} \; da = -\oint_l (c\vec{E} + \vec{v} \times \vec{B}) \cdot d\vec{l}, \tag{1.7}$$

where $\vec{E}$ is the electric field and $\hat{n}$ is the unit vector pointing in the same direction as $d\vec{a}$. $\frac{d}{dt} \int_s \hat{n} \cdot \vec{B} da$ in Equation 1.7 is the rate of change of total magnetic flux going through the surface $S$ and the term $\vec{E} + \frac{\vec{v}}{c} \times \vec{B}$ is $\eta\vec{J}$ in resistive MHD. If $\eta = 0$ then total flux is constant in time which precisely describes Figure 1.4. Therefore in ideal-MHD,
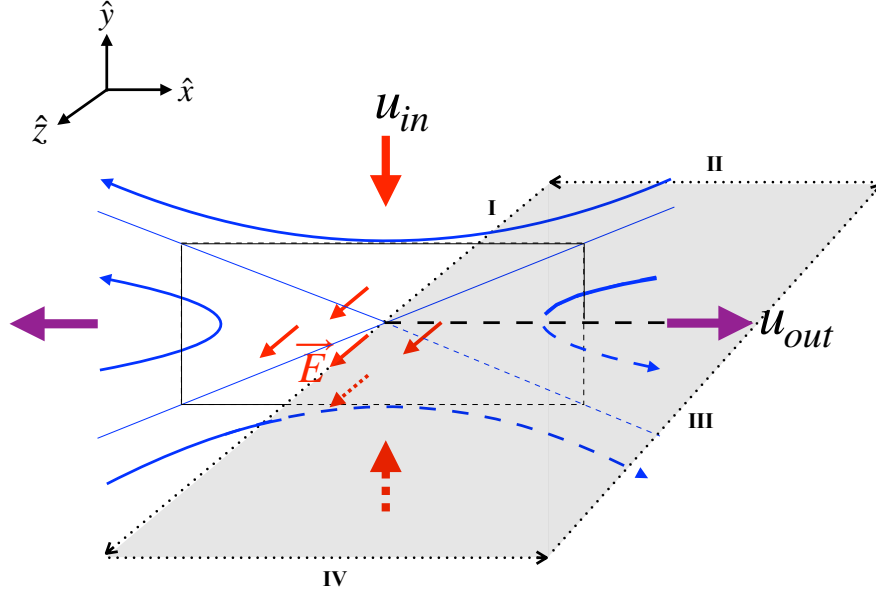
**Figure 1.5:** Reconnecting electric field $E_z$ is red and the magnetic field lines are blue. The shaded plane lies in xz-plane. Dashed arrows are below the plane.

magnetic fields do not diffuse and flux is conserved. Unsurprisingly, plasmas are not perfect conductors. Magnetic reconnection is possible when the frozen-in constraint is no longer valid. Magnetic reconnection can be viewed as a break down of ideal-MHD where the topology of magnetic field changes at the x-point.

## 1.4 Magnetic Topology

In 2D model, the magnetic field strength goes to zero at the null points classified as X-points and O-points. X-points and O-points are critical points of the z-component of the magnetic vector potential $\psi$ (defined in Section 1.7.1) - saddle point and relative extrema, respectively.

## 1.5 Definition of Reconnection Rate in 2D

In steady-state anti-parallel magnetic reconnection, the reconnection rate is calculated by estimating the out of plane electric field $E_z$ at the x-point (coordinate system

shown in Figure 1.5). $E_z$ is calculated from the rate at which magnetic flux flows into or away from the x-point. Faraday's law reads

$$\frac{d\phi_B}{dt} = -c \oint \vec{E} \cdot d\vec{l} \tag{1.8}$$

where $\phi_B$ is the total magnetic flux through a loop, $\vec{E}$ is the electric field, $t$ is time and $c$ is the speed of light. We employ this formula around a loop as shown in Figure 1.5. The integration along the loop is divided into four segments. Segment III can be extended all the way where the magnetic flux is not changing. Its contribution is dropped. Segments II and IV cancel because of uniformity in $\hat{z}$-direction in 2D. With only segment I remaining, Equation 1.8 is written as

$$\frac{1}{h}\frac{d\phi_B}{dt} = \frac{\partial}{\partial t}\int B_y dx = -cE_z \tag{1.9}$$

where $h$ is the length of segment I. Since $E_z$ is directly proportional to the rate of change of the total flux in 2D, it is used as a measure of reconnection rate[4].

## 1.6 Steady-State Reconnection

While performing magnetic reconnection simulation, 2.5 dimensions convention is often used to reduce computational expense. This means that the spatial domain is confined to a plane ($xy$-plane in this thesis) and fields are defined to have direction in all directions ($xyz$). Assuming no change along $z$-direction, we have, $\partial_z = 0$. Here we elaborate the mechanism of magnetic reconnection in steady-state. In steady-state, $\frac{\partial}{\partial t} = 0$ is assumed. If one were to take a snapshot of the dynamics at an earlier time in steady-state and compare it to the present time, no difference in dynamics are found. The continuity equation for the density $n$ is

$$\frac{\partial n}{\partial t} + \vec{\nabla} \cdot (n\vec{u}) = 0 \tag{1.10}$$

---

[4] $E_z$ is typically normalized to the upstream magnetic field and the outflow velocity to get the normalized reconnection rate.
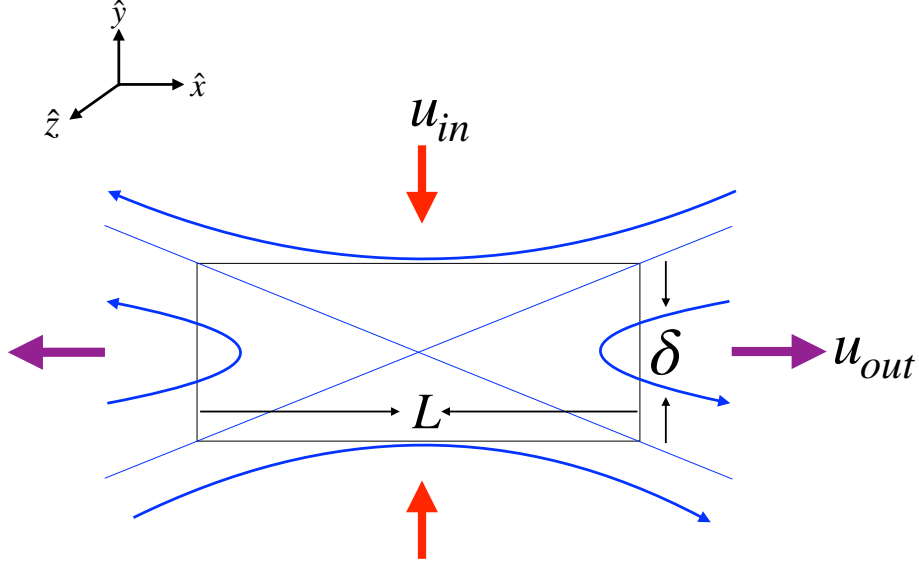
**Figure 1.6:** Plasma flowing in and out of the diffusion box in magnetic reconnection.

We further assume incompressibility and since $\frac{D}{Dt} = 0$, we have $\vec{\nabla} \cdot \vec{u} = 0$. This implies,

$$u_{in} = \frac{\delta}{L} u_{out} \tag{1.11}$$

where $u_{in} \sim u_y$ is the inflowing plasma speed and $u_{out} \sim u_x$ is the outflowing plasma speed. The derivation of Equation 1.11 is shown in Section 1.7.1. Similarly, using $\vec{\nabla} \cdot \vec{B} = 0$,

$$B_y = \frac{\delta}{L} B_x \tag{1.12}$$

where $B_x$ is the horizontal component of magnetic field just upstream of the diffusion box and $B_y$ is the vertical component of the magnetic field just outside the outflow region of the diffusion box. From the force balance equation

$$nm\frac{d\vec{u}}{dt} = -\nabla(P + \frac{B^2}{8\pi}) + \frac{\vec{B} \cdot \nabla \vec{B}}{4\pi}, \tag{1.13}$$

the convective term on the left side of Equation 1.13 balances the curvature term of the magnetic field on the right side to generate exhaust flows. We take the $x$-component and scale it. This gives

$$m_i n_o \frac{u_x^2}{L} \sim \frac{1}{4\pi} \frac{B_y B_x}{\delta}, \tag{1.14}$$

$$u_x^2 \sim \frac{B_x^2}{4\pi m_i n_0} \frac{L}{\delta} \frac{B_y}{B_x}, \tag{1.15}$$

$$u_{out} \sim c_{Aup}, \tag{1.16}$$

where $u_x = u_{out}$ and $c_{Aup} = \frac{B_x}{\sqrt{4\pi m_i n_0}}$. Upstream of the diffusion box ideal-MHD is valid. Ohm's law in ideal-MHD is simply

$$\vec{E} \sim -\frac{\vec{u}}{c} \times \vec{B}. \tag{1.17}$$

$B_y \sim 0$ in the upstream region, thus the $z$-component of Equation 1.17 is

$$E_z \sim \frac{u_{in} B_x}{c}. \tag{1.18}$$

The reconnection rate is generally defined in 2D as

$$u_{in} \sim c \frac{E_z}{B_x} \sim c_{Aup} \frac{\delta}{L}. \tag{1.19}$$

Note that $E_z$ in the vicinity of x-line is space independent if the system is locally in steady-state. This can be inferred when segment III is brought close to segment I in Figure 1.5. The magnetic flux does not change in time in the loop integral.

So far we have just defined the reconnection rate and have not assumed what breaks the frozen-in constraint. If the frozen-in constraint is broken solely due to $\eta \vec{J}$, then it is often referred as collisional Sweet-Parker reconnection. The Ohm's law in non-ideal MHD is given by

$$\vec{E} + \frac{\vec{u} \times \vec{B}}{c} = \eta \vec{J}. \tag{1.20}$$

Inside the diffusion region, $\vec{E} = \eta \vec{J}$ because $|\vec{B}|$ is small and the $z$-component of the electric field is

$$E_z = \eta J_z. \tag{1.21}$$

13

The current in the diffusion region is calculated using Ampère's law which gives

$$J_z = \frac{cB_x}{4\pi\delta}. \tag{1.22}$$

Using Equations 1.18, 1.21 and 1.22, we get

$$u_{in} \sim \frac{\eta c^2}{4\pi\delta} \tag{1.23}$$

Substituting Equation 1.19 in Equation 1.23, we get the reconnection rate for collisional Sweet-Parker reconnection as

$$u_{in} \sim \sqrt{\frac{\eta c^2 c_{Aup}}{4\pi L}} \tag{1.24}$$

which depends on resistive term $\eta$ and the length of the diffusion region.

## 1.7 Collisionless Hall Reconnection: Effect of Dispersive Wave Physics on Electron Diffusion Region

Above we describe the physics of dissipation mechanisms that drives magnetic reconnection using the Sweet-Parker analysis, where the collisional term in the Ohm's law $\eta\vec{J}$ plays the role of dissipation. In this section, we explore other terms in Ohm's law that break the frozen-in constraint.

### 1.7.1 Whistler Dynamics

We start by calculating the $z$-component of the vector potential $\vec{A}$, which is defined as $\vec{B} = \vec{\nabla} \times \vec{A}$. Expanding this relation in 2D, we get

$$\vec{B} = \frac{\partial A_z}{\partial y}\hat{x} - \frac{\partial A_z}{\partial x}\hat{y} + \left[\frac{\partial A_y}{\partial x} - \frac{\partial A_x}{\partial y}\right]\hat{z}. \tag{1.25}$$

Substituting $A_z = -\psi$, the magnetic field in this reduced system can be defined as:

$$\vec{B} = -\frac{\partial\psi}{\partial y}\hat{x} + \frac{\partial\psi}{\partial x}\hat{y} + \left[\frac{\partial A_y}{\partial x} - \frac{\partial A_x}{\partial y}\right]\hat{z} \tag{1.26}$$

Finally, we have

$$\vec{B} = B_z\hat{z} + \hat{z} \times \vec{\nabla}\psi, \tag{1.27}$$

14

where $B_z = \frac{\partial A_y}{\partial x} - \frac{\partial A_x}{\partial y}$. In the electron diffusion region, the dynamics of electrons are important while ions have negligible effects. Therefore, the current is carried mostly by electrons in the electron diffusion region (EDR) where the ions are present as a neutralizing background. This assumption is neatly written as $\vec{J} \cong -\frac{4\pi ne}{c}\vec{v}_e$ and thus we have

$$\vec{v}_e \cong -\frac{c}{4\pi ne}(\vec{\nabla} \times \vec{B}) \tag{1.28}$$

$$= -\frac{c}{4\pi ne}(\vec{\nabla} \times \vec{z} + \hat{z}\nabla^2\psi). \tag{1.29}$$

Using the electron momentum equation [Vasyliunas, 1975], we get

$$\vec{E} = -\frac{m_e}{e}\frac{d\vec{v}_e}{dt} - \frac{\vec{v}_e}{c} \times \vec{B} - \vec{\nabla} \cdot \overleftrightarrow{P}_e/ne \tag{1.30}$$

where $\overleftrightarrow{P}_e$ is the pressure tensor.

Here we explain previous important findings that are related to each term in Equation 1.30. The first term on the right of Equation 1.30 is the electron inertia term. The second term is essentially the Hall term disguised as $\frac{1}{4\pi ne}\vec{J} \times \vec{B}$. The last term, i.e., the electron pressure tensor term, can be decomposed into the diagonal and the off diagonal terms. The convective term of the electron inertial term can be neglected close to the X-line because the local velocity is close to zero (particles meander and the bulk velocity averages out to zero) and the non-gyrotropic pressure is equal to the reconnection electric field [Vasyliunas, 1975, Lyons and Brown, 1990, Hesse and Winske, 1993, 1998]. The convective term becomes important away from the x-line [Pritchett and Coroniti, 2004, Drake et al., 2005]. Note that, if one were to use Ohm's law of the form $\vec{E} = -\frac{\vec{v}_e}{c} \times \vec{B} - \vec{\nabla}P_e/ne$, where $P_e$ is the diagonal part of the pressure tensor, it would still be possible to show that electrons are frozen-in and therefore reconnection would not be viable in this model. This is essentially because the heat conduction of electron is really fast, see [Cowley, 2006]. The Hall term is what we are interested in as it describes physics outside the electron diffusion region

but inside the ion diffusion region (IDR). Further away from the ion diffusion region, MHD is valid. Using Faraday's law

$$\frac{\partial \vec{B}}{\partial t} = \vec{\nabla} \times (\vec{v}_e \times \vec{B}) \tag{1.31}$$

$$= \nabla_\perp \times [(\vec{v}_{e\perp} + v_{ez}\hat{z}) \times \vec{B}] \tag{1.32}$$

where the $\perp$ motion is used as perpendicular to $\hat{z}$. The $\perp$ component of Equation 1.32 is,

$$\frac{\partial}{\partial t}(\hat{z} \times \vec{\nabla}\psi) = \vec{\nabla}_\perp \times [\vec{v}_{e\perp} \times (\hat{z} \times \vec{\nabla}\psi)]. \tag{1.33}$$

Using $\hat{z} \times \vec{\nabla}\psi = -\nabla_\perp \times \hat{z}\psi$, Equation 1.33 gives

$$\frac{\partial \psi}{\partial t} = -[\vec{v}_{e\perp} \times (\hat{z} \times \vec{\nabla}\psi)] \tag{1.34}$$

$$= -\vec{v}_{e\perp} \cdot \vec{\nabla}\psi \tag{1.35}$$

$$= -\vec{v}_e \cdot \vec{\nabla}\psi. \tag{1.36}$$

Lastly, expanding Equation 1.31,

$$\frac{\partial B_z}{\partial t} = \left[ (\vec{\nabla} \cdot \vec{B} + \vec{B} \cdot \vec{\nabla})\vec{v}_e - (\vec{\nabla} \cdot \vec{v}_e + \vec{v}_e \cdot \vec{\nabla})\vec{B} \right] \cdot \hat{z} \tag{1.37}$$

Using incompressibility $\vec{\nabla} \cdot \vec{v}_e = 0$ and $\vec{\nabla} \cdot \vec{B} = 0$ and after some algebra $\{(\vec{v}_e \cdot \vec{\nabla})\vec{B}\} \cdot \hat{z} = 0$, Equation 1.37 simplifies to,

$$\frac{\partial B_z}{\partial t} = (\vec{B} \cdot \vec{\nabla})v_{ez} \tag{1.38}$$

The dynamical whistler equations are given by Equations 1.29, 1.36 and 1.38. These dynamical equations are well documented in previous works [Mandt et al., 1994, Biskamp et al., 1997, Shay and Drake, 1998]. Below we use scaling analysis using these dynamical equations to find the reconnection rate of collisionless Hall reconnection.

The $x$-component of Equation 1.29 is

$$v_{ex} = -\frac{c}{4\pi n e}\frac{\partial B_z}{\partial y} \sim \frac{c}{4\pi n e}\frac{B_z}{\delta}. \tag{1.39}$$
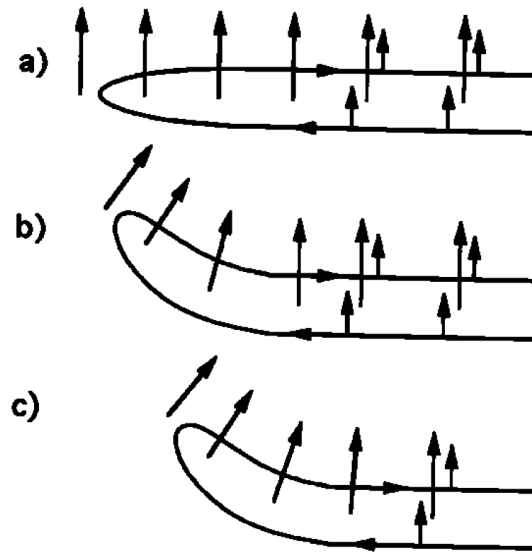
**Figure 1.7:** (a) Newly reconnected magnetic field lines in the reconnecting plane (xy). Analogous to perturbed field line in Figure 2.5 in Chapter 2. Electron flows of black arrows here are represented by light blue in Figure 2.5. (b) The electron flows drag the field line creating perturbed magnetic field in z-direction. The newly reconnected magnetic field line is bent with large exhaust velocity. (c) $v_{ex}$ convects the field line away from the null point. Reprinted from Mandt et al. [1994].
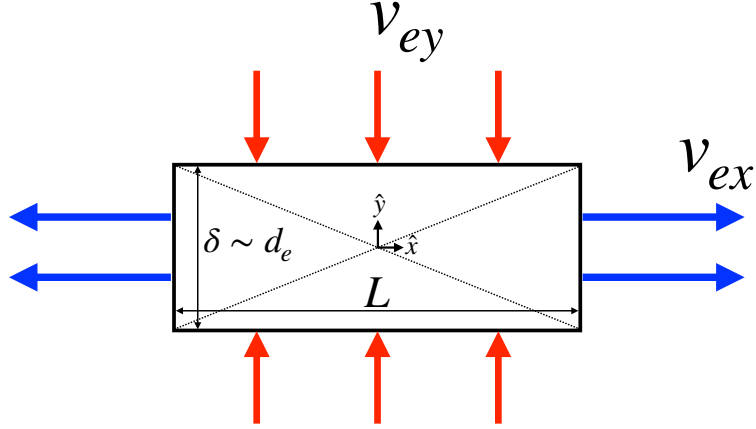
**Figure 1.8:** Schematic of electron diffusion region. The width is denoted by length $L$ and the height by $\delta$. The inflowing electrons $v_{ey}$ are shown in red arrows and the outflowing (exhaust) $v_{ex}$ are shown in blue arrows. Standing whistler wave dynamics play important role just outside the diffusion region.

The convection time out of the dissipation region in Figure 1.8 is given by $\Delta t = L/v_{ex}$. $B_y \frac{\partial V_{ez}}{\partial y} \sim 0$ because the diffusion region's thickness is defined as the thickness of out-of-plane current and noting that $B_y$ is an order of magnitude smaller than $B_x$. Hence, Equation 1.38 scales like $B_x \frac{v_{ez}}{L}$. Combining these relations, we get

$$B_z v_{ex} \sim B_x v_{ez} \tag{1.40}$$

The $z$-component of Equation 1.29 is given by

$$v_{ez} \sim \frac{c}{4\pi n e} \frac{B_x}{\delta}. \tag{1.41}$$

Substituting Equation 1.39 and 1.41 in Equation 1.40, we get $B_x \sim B_z$ and $v_{ex} \sim v_{ez}$. The incompressibility condition $\vec{\nabla} \cdot \vec{v}_e \sim 0$ using the divergence theorem gives $\oint_S \vec{v}_e \cdot d\vec{a} = 0$, where $S$ is the surface area with $\hat{n}$ specifying the direction as shown in
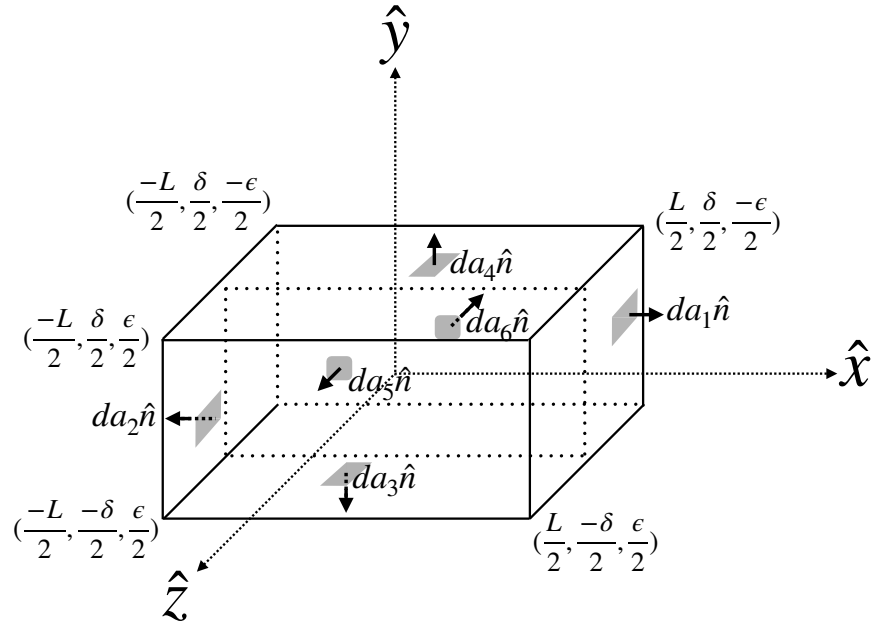
**Figure 1.9:** Diffusion region is extended in the z-axis with total thickness $\epsilon$ represented by dotted black rectangle in the center of the box. Inflowing electrons above the diffusion region points in $-\hat{y}$ direction and $+\hat{y}$ below the diffusion region. Similarly, outflowing electrons points in $+\hat{x}$ to the right and $-\hat{x}$ to the left.

Figure 1.9. Expanding $\oint_S \vec{v}_e \cdot d\vec{a}$,

$$\int \vec{v}_e \cdot da_1(\hat{x}) + \int \vec{v}_e \cdot da_2(-\hat{x}) + \int \vec{v}_e \cdot da_3(-\hat{y})$$

$$+ \int \vec{v}_e \cdot da_4(\hat{y}) + \int \vec{v}_e \cdot da_5(\hat{z}) + \int \vec{v}_e \cdot da_6(-\hat{z}) \quad (1.42)$$

The last two terms in 1.42 cancel each other out. Clearly, $\vec{v}_e$ at $x = \frac{L}{2}$ points in the $+\hat{x}$ direction and so on. Equation 1.42 turns into

$$\int_{-\epsilon/2}^{\epsilon/2} \int_{-\delta/2}^{\delta/2} v_{ex} \; dy \; dz \; |_{x=L/2} + \int_{-\epsilon/2}^{\epsilon/2} \int_{-\delta/2}^{\delta/2} v_{ex} \; dy \; dz \; |_{x=-L/2}$$

$$- \int_{-\epsilon/2}^{\epsilon/2} \int_{-L/2}^{L/2} v_{ey} \; dx \; dz \; |_{y=-\delta/2} - \int_{-\epsilon/2}^{\epsilon/2} \int_{-L/2}^{L/2} v_{ey} \; dx \; dz \; |_{y=\delta/2} \quad (1.43)$$

The integral along $z$-axis gives a factor of $\epsilon$ that is eliminated from $\vec{\nabla} \cdot \vec{v}_e \sim 0$. Thus, we've shown that

$$v_{ex}\delta \sim v_{ey}L$$

$$v_{ex}\delta \sim v_{in}L \quad (1.44)$$

We have derived a simple continuity equation that can be deduced by inspecting the structure of the dissipation region. Using $v_{ex} \sim v_{ez}$, Equation 1.44 and Equation 1.41, we get

$$v_{in} \sim v_{ex}\frac{\delta}{L} \sim v_{ez}\frac{\delta}{L} = d_e^2 \frac{\Omega_{e,up}}{L} \quad (1.45)$$

where, $\Omega_{e,up} = \frac{eBx}{m_e c}$ is based on the upstream magnetic field ($B_x$) and $d_e = c/\omega_{pe}$. The reconnection rate defined here as $v_{in}$ does not depend on $\delta$[5]. This expression holds true even if $\delta \to 0$. Therefore, the dynamics of the dissipation region and the mechanism that breaks the ideal MHD frozen-in constraint on the electrons has no impact on the reconnection rate [Mandt et al., 1994, Shay and Drake, 1998]. The standing whistler wave structure also explains the generation of quadrupolar Hall magnetic field in reconnection. The bending of the magnetic field lines as it propagates away from

---

[5] Normalized reconnection rate is $\frac{v_{in}}{v_{ex}} = \frac{v_{in}}{v_{out}} \sim \frac{\delta}{L}$

the diffusion region is shown in Figure 1.7. Since whistlers tilt the magnetic field line and $B_z$ is $\frac{\pi}{2}$ out of phase from the reconnecting magnetic field $B_x$, the quadrupolar $B_z$ structure is a result of whistler dynamics. The relation between $B_x$ and $B_z$ is similar to a plot shown in Figure 2.10(c) in Chapter 2. One can easily verify this result by inserting whistler dispersion relation in Equation 2.23.

### 1.7.2  Kinetic Alfvén Wave Dynamics

Kinetic Alfvén waves are associated with magnetic reconnection in the presence of a guide field[6]. One key signature is that the electron density perturbation is enhanced oppositely in the region of the quadrupolar Hall magnetic field [Kleva et al., 1995, Drake, 1995]. Even without an imposed guide field, magnetic reconnection can be understood as coupling to KAWs when significant out-of-plane magnetic field is generated along the separatrices [Shay et al., 2001b, Pyakurel et al., 2018]. The dynamical equations for KAWs are discussed below. Using the same form of magnetic field discussed in Section 1.7.1, we have

$$\nabla_\parallel = \hat{b} \cdot \vec{\nabla} = b_x \frac{\partial}{\partial x} + b_y \frac{\partial}{\partial y}, \tag{1.46}$$

where $\hat{b} = \frac{\vec{B}}{B}$. The definition from Equation 1.26 gives us

$$\nabla_\parallel = \frac{1}{B} \left[ -\frac{\partial \psi}{\partial y} \frac{\partial}{\partial x} + \frac{\partial \psi}{\partial x} \frac{\partial}{\partial y} \right] \tag{1.47}$$

$$= \frac{\hat{z}}{B} \times \vec{\nabla}\psi \cdot \vec{\nabla}. \tag{1.48}$$

For simplicity, in the guide field limit along the separatrices away from the electron diffusion region, we assume that the ions respond through polarization drift. Outside the diffusion region, overall dynamics of ions are governed by $\vec{E} \times \vec{B}$ drift motion. In this limit, the ion dynamics are electrostatic, $\vec{E} = -\vec{\nabla}\phi$, and $\vec{v}_\perp = c\frac{\vec{B} \times \vec{\nabla}\phi}{B^2}$ where $\phi$ is the electrostatic potential. The divergence of this motion is approximately zero. Using the continuity equation of ions, it can be shown that $\vec{E} \times \vec{B}$ drift does

---

[6] Guide field is the presence of $B_z$ initially along $z$-direction with the coordinate system shown in Figure 1.5.

not contribute to any change in density. Thus, any change in density must come from polarization drift[7]. The in-plane electric field component $E_y$ is large and its full derivative in time is what constitutes of the polarization drift motion. It is

$$\vec{v}_p = -\frac{c}{\omega_c B}\frac{d\vec{E}_\perp}{dt}.$$ (1.49)

In steady state, $\frac{d}{dt} = \vec{v}\cdot\vec{\nabla}$. The ions drift into the inflowing region. As the $\vec{E}\times\vec{B}$ drift increases in the exhaust region, this energy comes from the polarization drift. The linearized continuity equation of ions is $\frac{\partial n_i}{\partial t} + \vec{\nabla}\cdot(n_i\vec{v}_i) = 0$. Rearranging this continuity equation, we have $\frac{dn_i}{dt} = -n_i\vec{\nabla}\cdot\vec{v}_i$. The linearized form of this equation is

$$\frac{dn_i}{dt} = -n_0\vec{\nabla}\cdot\vec{v}_i.$$ (1.50)

Also, $\vec{\nabla}_\perp\phi = \vec{\nabla}\phi - \hat{b}(\hat{b}\cdot\vec{\nabla})\phi = -\vec{E}_\perp$. Substituting this relation and Equation 1.49 in Equation 1.50, we get density perturbation from the drift polarization as

$$n_i \sim \frac{n_0 c}{\Omega_{i,z}}\frac{1}{B_z}\nabla_\perp^2\phi,$$ (1.51)

where $\Omega_{i,z} = \frac{eB_z}{m_i c}$.

For simplicity, we include the resistive term in Ohm's law and ignore the inertial term in Equation 1.30. We also assume isotropic pressure and isothermal equation of state. The parallel electric field is given by

$$E_\parallel = \eta J_\parallel - \frac{T_e}{n_0 e}\nabla_\parallel n.$$ (1.52)

Taking the dot product of $\vec{E} = \vec{\nabla}\phi + \frac{1}{c}\frac{\partial\vec{A}}{\partial t}$ with $\hat{b}$ and noting that $|B_z|$ is large, $E_\parallel = \frac{1}{c}\frac{\partial\psi}{\partial t}$. Using Ampère's law and once again the definition of $\vec{B}$, $J_\parallel = \frac{c}{4\pi}\nabla^2\psi$. Substituting the parallel electric field and current in Equation 1.52, we get one of the dynamical equations that govern KAWs as

$$\frac{d\psi}{dt} + c\rho_s^2\nabla_\parallel\nabla^2\phi - \frac{\eta c^2}{4\pi}\nabla^2\psi = 0.$$ (1.53)

---

[7] This approximation is only valid so long as $T_e \sim T_i$. If $T_i \gg T_e$, two-fluid approximation is required which is described in Chapter 2

22

where $\rho_s = \frac{\sqrt{T_e/m_i}}{\Omega_{i,z}}$ The other dynamical equation of kinetic Alfvén waves is found by taking the $z$-component of the curl of the momentum equation shown in Equation 1.13. The curl of the pressure terms vanish, and we have $\vec{\nabla} \times (\vec{B} \cdot \vec{\nabla}) \vec{B} = -\vec{\nabla} \times (\vec{B} \times (\vec{\nabla} \times \vec{B}))$. Also noting that $\vec{\nabla} \times \vec{B} = \hat{z} \nabla^2 \psi$ and $\vec{\nabla} \times (\vec{z} \times \vec{\nabla} \phi) = \hat{z} \nabla^2 \phi$, we get

$$B_z \frac{c}{c_{A,z}^2} \frac{d\nabla^2 \phi}{dt} = -\vec{\nabla} \times \left[ \hat{z} \times \vec{\nabla} \psi \times \hat{z} \nabla^2 \psi \right] \tag{1.54}$$

$$= -\vec{\nabla}(\nabla^2 \psi) \times \vec{\nabla} \psi \tag{1.55}$$

$$= -B_z \left[ \frac{\partial \psi}{\partial y} \frac{\partial}{\partial x} - \frac{\partial \psi}{\partial x} \frac{\partial}{\partial y} \right] \nabla^2 \psi \tag{1.56}$$

The second dynamical equation is

$$\frac{d\nabla^2 \phi}{dt} = \frac{c_A^2}{c} \nabla_{\parallel} (\nabla^2 \psi) \tag{1.57}$$

Linearizing Equations 1.53 and 1.57, we get

$$\omega^2 = k_{\parallel}^2 c_A^2 (1 + k_{\perp}^2 \rho_s^2) \tag{1.58}$$

which has an extra added term with shear Alfvén waves when $k_{\perp} \rho_s > 1$. This scaling of KAWs comes into play when $k_{\perp} \rho_s \gtrsim 1$, and we find that the scale length of the ion-diffusion region is $\rho_s \sim \rho_i$ if $T_e \sim T_i$. As is seen in Chapter 4, in the large guide-field limit and $\beta \sim 1$, the scaling of reconnection rate is about $\sim 0.1 c_A$ for fully ion coupled reconnection. We further explore the length scales of the ion-diffusion region in the guide-field case at which the ions couple to magnetic reconnection in later chapters. Further, the dynamics of KAWs on the electron diffusion region is similar to whistlers in the sense that the reconnection rate does not depend on $\delta$.

Building on previous work on whistlers, we formally derive a Sweet-Parker like scaling analysis of the electron diffusion region when guide field is introduced. It serves us with some insightful physical intuition of the diffusion region[8]. For $\beta \ll 1$, the

---

[8] This analysis was formulated by Professor Michael Shay and as far as we know has not been shown in literature.

electrons primarily flow parallel to field lines to create a density perturbation. Using this fact, we have

$$\frac{\partial n_1}{\partial t} \sim n_0 \nabla_\parallel v_{e\parallel}$$
$$\frac{n_1}{n_0} \sim \frac{v_{e\parallel}\Delta t}{L_\parallel}, \tag{1.59}$$

where $\Delta t$ is the time scale associated to the change in density $n_1$ and $L_\parallel$ is the parallel distance. Within the electron diffusion region, $\vec{v}_e \sim \frac{c}{4\pi ne}\vec{\nabla} \times \vec{B}$. The components of $\vec{v}_e$ scale as

$$v_{ex} \sim \frac{c}{4\pi n_0 e}\frac{B_z}{\delta} \tag{1.60}$$

$$v_{ez} \sim \frac{c}{4\pi n_0 e}\frac{B_x}{\delta}. \tag{1.61}$$

The pressure balance equation gives

$$B_z = \frac{4\pi n_1 T}{B_{0z}}. \tag{1.62}$$

Substituting Equation 1.62 into Equation 1.60, we get the following relation:

$$v_{ex} \sim \frac{n_1}{n_0}\frac{c_s^2}{\Omega_{i,z}}\frac{1}{\delta}. \tag{1.63}$$

The density perturbation from Equation 1.59 is replaced in Equation 1.63 and we have

$$v_{ex} \sim d_i^2 \frac{B_x}{B_{0z}}\frac{\Delta t}{L_\parallel}\frac{c_s^2}{\delta^2}, \tag{1.64}$$

where $d_i = \frac{c}{\omega_{pi}}$ and $c_s^2 = \frac{T}{m_i}$. The parallel distance in the guide field is approximately $L\frac{B_{z0}}{B_x}$ where $L$ is the length of the diffusion box as shown in Figure 1.8 and the time taken by the field line to traverse the diffusion region is $\frac{L_\parallel}{v_{ex}}$. Thus, we have

$$v_{ex} \sim \frac{d_i^2}{\delta^2}\frac{B_x^2}{B_{0z}^2}\frac{c_s^2}{v_{ex}}$$
$$v_{ex} \sim \frac{d_i}{\delta}\frac{B_x}{B_{0z}}c_s. \tag{1.65}$$

The reconnection rate takes the form

$$v_{in} \sim \frac{B_x}{B_{0z}}\frac{d_i}{L}c_s, \tag{1.66}$$

which has no dependence on $\delta$, once again.

## Chapter 2

## DISPERSIVE WAVE PHYSICS IN MAGNETIC RECONNECTION AND KINETIC EFFECTS

### 2.1  Two-fluid Linear Waves

In this section, we will use basic linear theory to derive insights into different plasma systems. The first part of this Chapter explores plasmas that are fluid-like. A more detailed kinetic picture of plasma is covered at the end of this Chapter where non-collisional damping is investigated. We adopt a two fluid description to study the plasma waves we are interested in. Alfvén waves, whistler waves and kinetic Alfvén waves are then derived. We choose these waves because their wave properties are often invoked while investigating magnetic reconnection.

The two fluid description can be derived using the electron equation of motion. We follow the blueprint prescribed in Rogers et al. [2001]. The equation governing the motion of electron fluid is

$$\vec{E} = -\frac{m_e}{e}\frac{d\vec{v}_e}{dt} - \frac{\vec{v}_e}{c} \times \vec{B} - \nabla P_e/ne. \tag{2.1}$$

Note that $\vec{v}_e = \vec{v}_i - \frac{\vec{J}}{ne}$. Substituting this in Equation 2.1 while ignoring the ion velocity ($\vec{v}_i \sim 0$) in the first term of the right hand side of the equation, and using Faraday's law gives

$$\frac{\partial \vec{B}}{\partial t} = -\frac{c^2}{\frac{4\pi ne^2}{m_e}}\frac{d}{dt}(\nabla \times (\nabla \times \vec{B})) + \nabla \times (\vec{u} \times \vec{B}) - \frac{e}{mc}\nabla \times ((\nabla \times \vec{B}) \times \vec{B}), \tag{2.2}$$

where $\vec{v}_i = \vec{u}$ and $m_i = m$. The continuity equation is given by

$$\frac{\partial n}{\partial t} + \nabla \cdot (n\vec{u}) = 0. \tag{2.3}$$
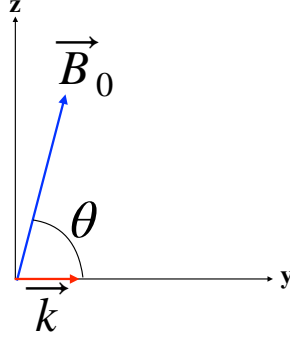
**Figure 2.1:** The wave vector $\vec{k}$ lies in $y$-direction. The background magnetic field $\vec{B}_0$ spans y-z plane.

Lastly, the momentum evolution equation is

$$nm\frac{d\vec{u}}{dt} = -\nabla(P + \frac{B^2}{8\pi}) + \frac{\vec{B}\cdot\nabla\vec{B}}{4\pi}. \tag{2.4}$$

In order to linearize the equations, we assume that the plasma is perturbed around an equilibrium. For example, the fields are perturbed around $\vec{B}_0$ and $\vec{E}_0$ and similarly around $u_0$ and the density $n_0$. Hence, they are written as

$$
\begin{aligned}
\vec{E} &= \vec{E}_0 + \vec{E}_1 = \vec{E}_0 + \tilde{\vec{E}}_1 \exp[i(\vec{k}\cdot\vec{x} - \omega t)] \\
\vec{B} &= \vec{B}_0 + \vec{B}_1 = \vec{B}_0 + \tilde{\vec{B}}_1 \exp[i(\vec{k}\cdot\vec{x} - \omega t)] \\
\vec{u} &= \vec{u}_0 + \vec{u}_1 = \vec{u}_0 + \tilde{\vec{u}}_1 \exp[i(\vec{k}\cdot\vec{x} - \omega t)] \\
n &= n_0 + n_1 = n_0 + \tilde{n}_1 \exp[i(\vec{k}\cdot\vec{x} - \omega t)].
\end{aligned}
\tag{2.5}
$$

To close these system of equations, we assume isothermal equation of state where the ratio of specific heats $\gamma = 1$, giving $P_i = nT_i$ and $P_e = nT_e$[1]. In the frame of equilibrium plasma flows, $\vec{u}_0$ and $\vec{E}_0$ is zero. Without any further loss of generality, we assume that the wave vector is in the $\hat{y}$ direction and the background magnetic field $\vec{B}_0$ is in the $yz$-plane as shown in Figure 2.1.

---

[1] $n_i \sim n_e \sim n$ is assumed.

Substituting Equation 2.5 in Equation 2.2, we get the following equation :

$$-i\omega\vec{B}_1 = id_e^2\omega k^2\vec{B}_1 + i[kB_{0y}\vec{u} - (\vec{k}\cdot\vec{u})\vec{B}_0] + \frac{e}{mc}d_i^2(\vec{k}\times\vec{B}_1)B_{0y}k \tag{2.6}$$

where $d_e = c/\omega_{pe} = c/\sqrt{4\pi n_0 e^2/m_e}$ and $d_i = c/\omega_{pi} = c/\sqrt{4\pi n_0 e^2/m_i}$. Sorting out Equation 2.6 gives us following equations which will come in useful for the construction of the dispersion relation:

$$\begin{aligned}
-i\omega(1 + d_e^2 k^2)\vec{B}_1 &= ikB_{0y}(u_{x1}\hat{x} + u_{y1}\hat{y} + u_{z1}\hat{z}) \\
&\quad - (\vec{k}\cdot\vec{u})(B_{0y}\hat{y} + B_{0z}\hat{z}) \\
&\quad + \frac{e}{mc}d_i^2 kB_{0y}(k_y B_{1z}\hat{x} - k_y B_{x1}\hat{z}).
\end{aligned} \tag{2.7}$$

From the force balance equation 2.4, we have

$$m_i n_0 \omega\vec{u}_1 = -\frac{k}{4\pi}B_{y0}B_{x1}\hat{x} + (Tn_1 + \frac{B_{z0}}{4\pi}B_{z1})k\hat{y} - \frac{k}{4\pi}B_{y0}B_{z1}\hat{z}. \tag{2.8}$$

Lastly, the continuity equation from 2.3 gives

$$n_1 = \frac{n_0}{\omega}k_y u_{y1}. \tag{2.9}$$

Rearranging Equations 2.7 - 2.9, we get a matrix that has the following form:

$$\begin{bmatrix}
-i\omega(1 + d_e^2 k^2) & -\frac{e}{mc}d_i^2 k^2 B_{y0} & -ikB_{y0} & 0 & 0 & 0 \\
\frac{e}{mc}d_i^2 k^2 B_{y0} & -i\omega(1 + d_e^2 k^2) & 0 & ikB_{z0} & -ikB_{y0} & 0 \\
\frac{k}{4\pi}B_{y0} & 0 & mn_0\omega & 0 & 0 & 0 \\
0 & -\frac{k}{4\pi}B_{z0} & 0 & mn_0\omega & 0 & -Tk \\
0 & \frac{k}{4\pi}B_{y0} & 0 & 0 & mn_0\omega & 0 \\
0 & 0 & 0 & -n_0 k & 0 & \omega
\end{bmatrix}
\begin{bmatrix}
B_{x1} \\
B_{z1} \\
u_{x1} \\
u_{y1} \\
u_{z1} \\
n_1
\end{bmatrix}
= \begin{bmatrix} 0 \end{bmatrix}$$

Now that we have derived the full dispersion tensor of the two-fluid model, we are equipped to derive whistler waves and KAWs. Taking the determinant of this matrix gives us the dispersion relation

$$\nu^6 - \left[\frac{c_{mk}^2}{c_{Ak}^2} + \frac{1}{D}\left(1 + \frac{k^2 d_i^2}{D}\right)\right]\nu^4 + \frac{1}{D}\left[\frac{c_{mk}^2}{c_{Ak}^2} + \frac{c_s^2}{c_{Ak}^2}\left(1 + \frac{k^2 d_i^2}{D}\right)\right]\nu^2 - \frac{c_s^2}{D^2 c_{Ak}^2} = 0, \tag{2.10}$$

where $\nu = \frac{\omega}{kc_{Ay}}$, $c_{Ay}^2 = \frac{B_{y0}^2}{4\pi m_i n_0}$, $D = 1 + k^2 d_e^2$, $d_e = \frac{c}{\omega_{pe}}$, $c_A^2 = \frac{B_0^2}{4\pi m_i n_0}$, $c_s^2 = \frac{T_e + T_e}{m_i}$, $c_{mk}^2 = \frac{c_A^2}{D} + c_s^2$ and $c_m^2 = c_A^2 + c_s^2$. We denote $c_{Ay}$ as $c_{Ak}$ interchangeably as $\vec{k}$ points in the $y$-direction. In order to solve Equation 2.10, we simplify it in terms of polynomials of $(\frac{\omega}{\Omega_i})^2$. This equation when expanded takes the following form

$$
\begin{aligned}
A^3 & \\
- \left[ \frac{1}{D cos^2(\theta)} + \frac{\beta}{2cos^2(\theta)} + \frac{1}{D}\left(1 + \frac{k^2 d_i^2}{D}\right) \right] (k^2 d_i^2)cos^2(\theta)A^2 & \\
+ \frac{1}{D}\left[ \frac{1}{D cos^2(\theta)} + \frac{\beta}{2cos^2(\theta)} + \frac{\beta}{2cos^2(\theta)}\left(1 + \frac{k^2 d_i^2}{D}\right) \right] (k^4 d_i^4)cos^4(\theta)A & \quad (2.11) \\
- \frac{\beta}{2D^2}(k^6 d_i^6)cos^4(\theta) & \\
= 0,
\end{aligned}
$$

where $A = (\frac{\omega}{\Omega_i})^2$ and $\beta = \frac{2c_s^2}{c_A^2}$. One can solve the roots of this equation to obtain the value of $\frac{\omega}{\Omega_i}$. Equation 2.10 contains many regimes of waves depending on the propagation angle and the magnetic energy relative to the thermal energy i.e. $\beta$. Parameters chosen for this Chapter are given in Table 2.1. The dispersion curves for

| Case | $\beta$ | $\theta$ | $m_e/m_i$ | $T_e/T_i$ | $\frac{C_m}{C_s}$ | $\frac{C_m}{C_{Ak}}$ | $d_e/d_i$ | Regime |
|------|------|------|---------|---------|-------|-------|-------|-------------------|
| I | 0.1 | 55. | 1/1836 | 1/10 | 14.17 | 1.74 | 42.8 | Whistler only |
| II | 0.1 | 89.0 | 1/1836 | 1/10 | 14.17 | 16.42 | 42.8 | KAW only |
| III | 10 | 55. | 1/1836 | 1/10 | 1.09 | 4.27 | 42.8 | KAW and Whistler |
| IV | 10 | 89.0 | 1/1836 | 1/10 | 1.09 | 40.12 | 42.8 | KAW only |

**Table 2.1:** Plasma parameters for small and large beta with obliquely travelling waves. Real mass ratio is chosen with electrons ten times cooler than ions.

$\beta = 0.1$ and $\beta = 10$ are plotted in Figure 2.2 and 2.3. The dashed curve in Figure 2.2(a) shows whistler waves in the wave number regime $\frac{c_m}{c_s} \ll kd_i \ll \frac{d_i}{d_e}$ bounded by two dotted vertical black lines. On the other hand, the kinetic Alfvén wave dispersion curve is shown by the dashed blue curve existing in $\frac{c_m}{c_s} \ll kd_i \ll \frac{d_i}{d_e}$ in Figure 2.2(b) between two dotted vertical black lines. For large $\beta$, $\beta = 10$, Figure 2.3(a) is shown to have a large range of whistler wave regime. The whistler regime is shown in between the dotted

black lines denoted by $c_m/c_{Ak}$ and $d_i/d_e$. Whistler waves in this parameter regime start at $kd_i \gg 1$. For highly oblique propagation and large $\beta$, shown in Figure 2.3(b), the dashed red line looks like a straight line. This line approaches $kd_i = \frac{d_i}{d_e}$ well before $kd_i = \frac{c_m}{c_{Ak}}$. Hence, whistlers do not exist in this regime. In general, whistlers have very broad frequency spectrum. Kinetic Alfvén waves can also occupy broad spatial scales. Note that the spatial scale of kinetic Alfvén waves is larger than whistler waves.

To derive the whistler waves the following approximations are made. For whistler waves, the phase velocity is larger than the magnetosonic waves given by $(\frac{\omega}{k})^2 \gg c_A^2 + c_s^2$. Further, we know that the whistler wavelength cannot be smaller than electron inertial scale $d_e$ and the wavelength at most can be of ion inertial scale $d_i$. Therefore, we impose $d_e < k^{-1} < d_k$ where $d_k = d_i \frac{c_{Ak}}{c_m} = d_i \frac{\cos(\theta)}{\sqrt{1+\beta/2}}$. Note that, the upper limit of $\frac{c_{Ak}}{c_m}$ is 1. Equating the first and second term of Equation 2.10 and using the approximations discussed above, we get

$$\frac{\omega^2}{k^2 c_{Ay}^2} \approx \frac{c_m^2}{c_{Ay}^2} + k^2 d_i^2. \tag{2.12}$$

The final approximation in Equation 2.12 is $kd_i > \frac{c_m}{c_{Ay}}$ giving us the whistler wave dispersion relation,

$$\frac{\omega}{k} = kd_i c_{Ay} \tag{2.13}$$

The phase velocity of whistlers depends on $k$, making it a dispersive wave. As the wavelength of whistlers become smaller, we expect the wave to propagate faster. Using this dispersion relation, we calculate the parallel ($v_{\|g}$) and perpendicular $v_{\perp g}$ group velocities.

$$v_{\|g} = \frac{\partial \omega}{\partial k_\|} = kd_i c_A + k_\| d_i c_{Ay} \tag{2.14}$$

$$v_{\perp g} = \frac{\partial \omega}{\partial k_\perp} = k_\perp d_i c_{Ay}. \tag{2.15}$$

where $k_\| = k\cos(\theta)$ and $k_\perp = k\sin(\theta)$.
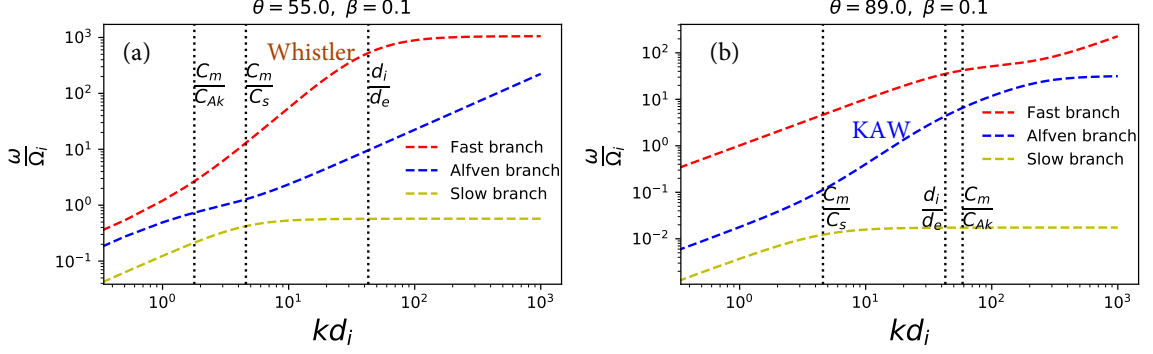
**Figure 2.2:** Dispersion relation for cases I and II shown in Table 2.1. (a) For low $\beta$, kinetic Alfvén waves do not exist for a propagation angle of $\theta = 55$ whereas whistlers exist for this regime occupying broad wavenumber space. (b) KAWs occupy large wavenumber space since, for these plasma parameters, whistlers don't exist.

As noted in Equation 2.14 and Equation 2.15, the perpendicular and the parallel velocities of whistler waves are angle dependent. For oblique propagation, $k \sim k_\perp$ and we get the following group velocities of whistler wave

$$v_{\parallel g} \sim k d_i c_A \tag{2.16}$$

$$v_{\perp g} = \frac{\partial \omega}{\partial k_\perp} = k_\perp d_i c_{Ay} = k_\parallel d_i c_A \sin(\theta) \sim k_\parallel d_i c_A. \tag{2.17}$$

Subsequently, we derive the dispersion relation of kinetic Alfvén waves (KAW). KAWs are more complicated as the electron inertia term and the pressure term in the momentum equation 2.4 contribute to the wave. The phase velocity of KAWs is larger than the Alfvén speed and less than the sound speed, $c_{Ak}^2 \ll \frac{\omega^2}{k^2} \ll c_s^2$. Imposing $k^2 d_e^2 \ll 1$, $\frac{c_s^2}{c_m^2} \ll k^2 d_i^2 \ll \frac{c_m^2}{c_{Ak}^2}$ and equating the second and third terms in Equation 2.10 we obtain

$$\nu^2 \approx \frac{1 + \frac{c_s^2}{c_m^2}(1 + k^2 d_i^2)}{1 + \frac{c_{Ak}^2}{c_m^2}(1 + k^2 d_i^2)}. \tag{2.18}$$

Note that in Equation 2.18, $\frac{c_{Ak}^2}{c_m^2} \gg 1$ and so $\frac{c_{Ak}^2}{c_m^2}k^2d_i^2 \ll 1$. Therefore, the denominator tends to 1. Using these approximations, we finally get the dispersion relation of KAWs as

$$\nu^2 \approx \frac{c_s^2}{c_m^2}k^2d_i^2$$
$$\frac{\omega}{k} = c_{Ay}\frac{c_s}{c_m}kd_i. \tag{2.19}$$

It is seen that KAWs are dispersive like whistler waves. To explore the physics governing KAWs, we invoke eigenvectors calculated from Equations 2.6-2.9. Expressing all the quantities in term of the perturbed magnetic field in the $x$-direction gives us the following eignenvectors. Here, we use normalized quantities where the velocities are normalized to $c_A$, frequency to $\Omega_i$ and magnetic fields to $B_0$.

$$u_{x1} = -kd_iB_{x1}\cos(\theta)/\omega \tag{2.20}$$

$$u_{y1} = \tan(\theta)\frac{i[(kd_i\cos(\theta))^2 - \omega^2 D]}{kd_i[\omega^2 - k^2d_i^2\frac{\beta}{2}]}B_{x1} \tag{2.21}$$

$$u_{z1} = \frac{-i[(kd_i\cos(\theta))^2 - \omega^2 D]}{(kd_i)\omega^2}B_{x1} \tag{2.22}$$

$$B_{z1} = \frac{i[(kd_i\cos(\theta))^2 - \omega^2 D]}{k^2d_i^2\omega\cos(\theta)}B_{x1} \tag{2.23}$$

$$n_1 = \frac{\tan(\theta)}{\omega}\frac{i[(kd_i\cos(\theta))^2 - \omega^2 D]}{[\omega^2 - k^2d_i^2\frac{\beta}{2}]}B_{x1} \tag{2.24}$$

The components of the electric field in the two fluid model can be readily calculated using Ohm's law:

$$E_x = -u_{y1}\sin(\theta) + u_{z1}\cos(\theta) + ikd_i\cos(\theta)B_{x1} \tag{2.25}$$
$$E_y = u_{x1}\sin(\theta) - ikd_i\sin(\theta)B_{z1} - ikd_i\frac{T_e}{T_i}v_{thi}^2n_1 \tag{2.26}$$
$$E_z = -u_{x1}\cos(\theta) + ikd_i\cos(\theta)B_{z1} \tag{2.27}$$
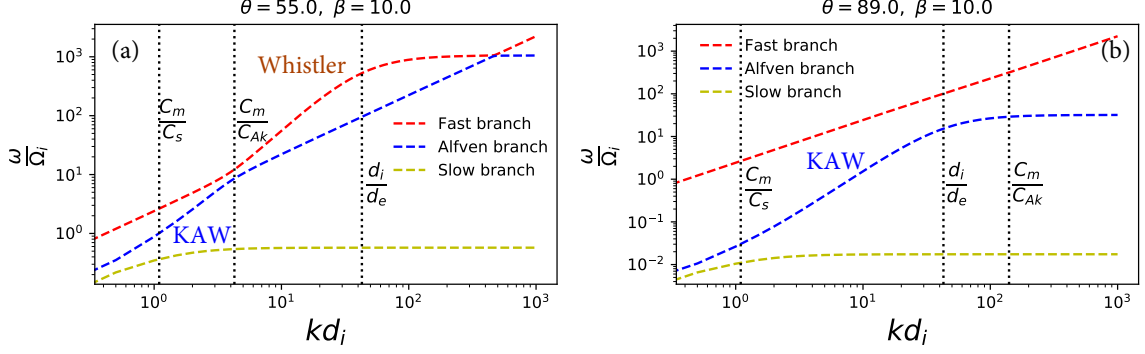
**Figure 2.3:** Dispersion relation for cases III and IV shown in Table 2.1. (a) For large $\beta$ and less oblique waves kinetic Alfvén waves and whistlers both exist occupying broad wavenumber spectrum. (b) For highly oblique wave, whistlers do not exist while KAWs span large range of $kd_i$.

And similarly the electron flows can be written as

$$v_{ex} = u_{x1} - i\ kd_i\ B_{z1} \tag{2.28}$$

$$v_{ey} = u_{y1} \tag{2.29}$$

$$v_{ez} = u_{z1} + i\ kd_i\ B_{x1} \tag{2.30}$$

## 2.2 Comments on full numerical Vlasov linear dispersion solver

We have opted to use open source code the New Hampshire Dispersion Relation Solver (NHDS) [Verscharen et al., 2013] to get solutions of the full linear Vlasov dispersion tensor. The details of the code is beyond the scope of this thesis; nonetheless, it is a great resource for us to understand kinetic effects that are removed from the present two-fluid analysis. The coordinate system used in NHDS is different from our analysis. The coordinate system in our two-fluid analysis was chosen based on magnetic reconnection simulations that will be presented in later Chapters. Therefore, it is important that a correct coordinate transformation be used while comparing our analysis with the results from NHDS. In Figure 2.4, the un-primed coordinate system is for the two-fluid coordinate system and the primed coordinate system is for the NHDS
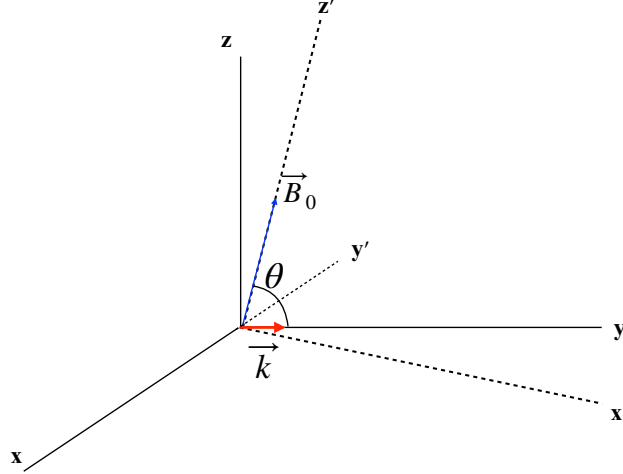
**Figure 2.4:** Primed coordinate system is used by NHDS while the un-primed are for the two-fluid analysis. The background magnetic field $\vec{B}_0$ lies in the $z'$-direction and the wave vector $\vec{k}$ in the $x' - z'$ plane.

coordinate system. Any vector in the primed system can be rotated by using a simple rotation matrix. The rotation matrix $\overleftrightarrow{R}$ is given by

$$\overleftrightarrow{R} = \begin{pmatrix} 0 & -1 & 0 \\ \sin(\theta) & 0 & \cos(\theta) \\ -\cos(\theta) & 0 & \sin(\theta) \end{pmatrix}, \qquad (2.31)$$

where $\theta$ is the angle between the wave vector $\vec{k}$ and the ambient magnetic field $\vec{B}_o$. The analyses presented in Section 2.4 are based on numerical results from NHDS.

### 2.3 Whistler waves

The dynamics of whistler waves are already covered in Michael Shay's thesis (1998). To further examine similarities and differences between whistlers and KAWs, we have included some analysis of whistlers in this thesis as well. For comparison purposes with the KAW, we focus on oblique whistler waves. Note, however, that the basic dynamics of parallel propagating whistlers are essentially the same as the oblique case, although the parameter space where they exist may be different. Whistlers are

# Standing Whistler Wave Schematic
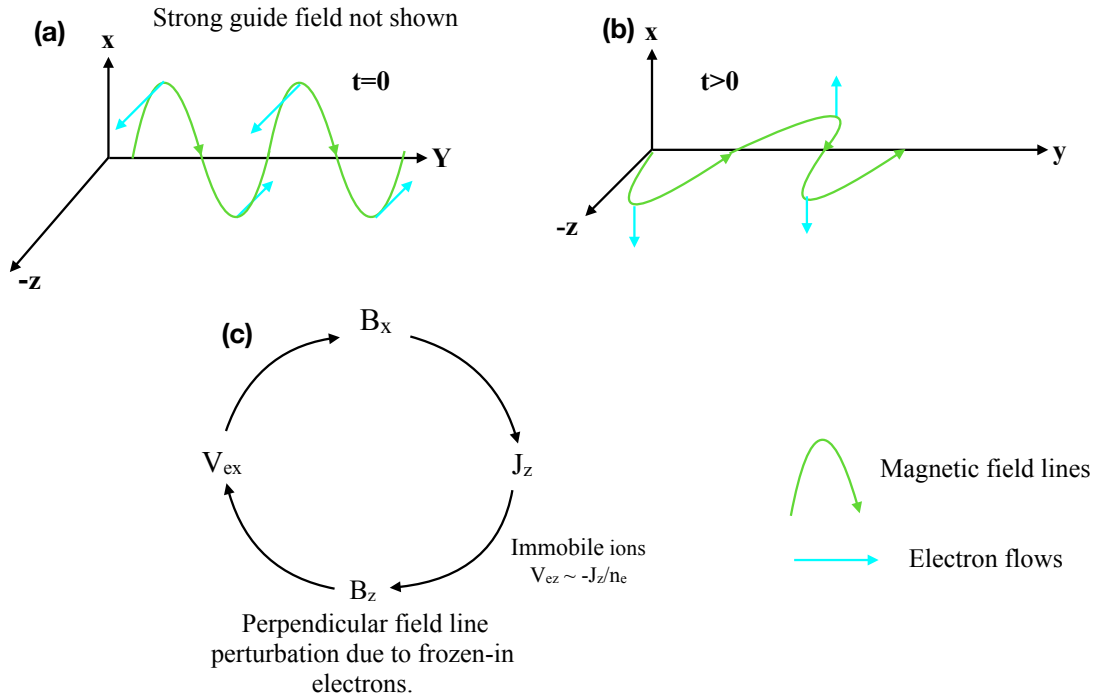


**Figure 2.5:** (a) and (b): The bending of the magnetic field line produces current which in turn induces perturbed magnetic field perpendicular to the plane. Whistlers are circularly polarized. (c) Causality diagram of whistler wave is shown. Electrons are frozen in with negligible pressure perturbation.

inherently three-dimensional. The electron flows being frozen-in to the field creates a perturbation perpendicular to the initial disturbance in the magnetic field, thereby making electrons flow in the perpendicular plane. This makes the wave circularly polarized. Any perturbation in the density is not a primary effect, which means that the dynamics of the force balance equation does not significantly change the propagation properties of the wave. In other words, the dispersion relation of whistlers are not affected. This is one of the main differences between KAWs and whistlers. For low $\beta$ plasma, the density perturbation has a drastic effect on KAWs. An example of whistler waves can be understood physically from Figure 2.5. Suppose a magnetic

field line pointing in the $y$-direction is perturbed in the $x$-direction with an amplitude $B_x$. Due to the bending of the field line, currents are induced in the $z$-direction. At each crest and trough of the wave, the electron flows are in opposite direction. This makes the magnetic field lines twist. This by necessity means a larger perturbation in $z$-component of the magnetic field. Therefore, the standing whistler wave circularly rotates. This standing whistler wave is a combination of two oppositely travelling whistler wave.

## 2.4  Kinetic Alfvén waves

The behaviour of oblique kinetic Alfvén waves (KAW) for large and small $\beta$ are different. For large $\beta$ and large $kd_i$, the dispersion relation of KAW is the same as a whistler. Therefore, separating these waves can be difficult. However, there are other key signature differences between these waves. Total pressure balance holds quite well for all oblique KAWs, while this is not the case for oblique whistlers. The perturbation in the magnetic field can also be different for these waves depending on the $\beta$ regime. Once again, we start by adding perturbation $B_x$ as shown in Figure 2.6. Just like the whistlers, the electron flows bend the field lines but with an added complication of density perturbation. For low $\beta$ KAW, a small $B_z$ perturbation is enough for the density to vary periodically in the wave propagation direction i.e, $y$-direction. The pressure balance in obliquely travelling wave in this thesis, chosen at $\theta = 89^o$, gives very small ion and electron flows in the $y$-direction. The largest electron flows are mostly in the parallel direction along $\hat{z}$. The causality diagrams for the kinetic Alfvén wave are shown in Figure 2.6.

Two-fluid approximation gives excellent agreement when compared to its kinetic counterpart. The results of the comparison of the electric field and pressure balance are shown in Figure 2.7. The electric field rotating in the $xz$-plane is highly elliptical in this parameter regime. Arbitrary $1^{st}$ and $2^{nd}$ points denoted by $*$ and $\cdot$ in blue and red colors are picked very close to each other. This determines the direction of rotation of electric field about y-axis. It is right handed if one were to look at the $\vec{k}$ direction.

# Standing Kinetic Alfven Wave Schematic

Low Beta: Strong guide field along z not shown
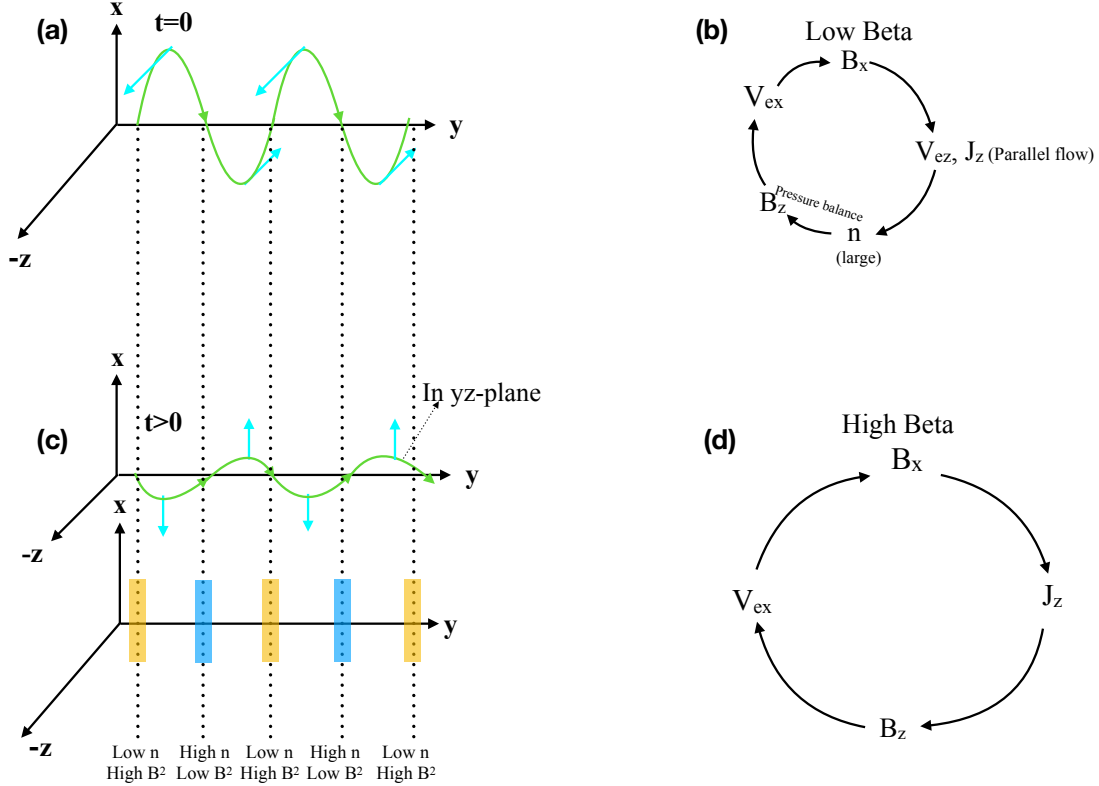


**Figure 2.6:** (a) Electrons flow parallel to magnetic field lines, i.e, in the $yz$-plane. Since they are frozen-in they also drag the field lines along x producing $B_x$. (c) $B_z$ is induced because of the current in $x$-direction. Ions flow along $y$ to counter the density drop to balance magnetic pressure. Causality diagrams of standing kinetic Alfvén waves (KAW) for low and high $\beta$ are shown in (b) and (d), respectively. Note that this illustration is a standing wave. KAWs are elliptically polarized, however their behavior can be different depending on plasma beta. KAWs have approximate pressure balance and $B_x$ and $B_z$ are phase shifted by $\frac{\pi}{2}$. For high $\beta$ plasma, this density perturbation is not so large, however for low beta plasma, density perturbation can be significant. High $\beta$ KAWs qualitatively behave like whistlers.

We find that the total pressure in the two-fluid model is nearly constant whereas the full-kinetic dispersion deviates slightly from the two-fluid model.

Though the behaviour of KAWs look very similar in the two-fluid analysis and the full Vlasov dispersion solver, there are some very important distinctions when it comes to analyzing the response of ions. This is seen in Figures 2.7, 2.8, 2.9, 2.11 and 2.12. It is clear using both kinetic and two-fluid models from these figures that the electron flows are primarily parallel to magnetic field and the ion response is perpendicular in the low $\beta$ regime. In the high $\beta$ regime, ions primarily flow parallel to the magnetic field too. One key difference that deserves a second look is shown in Figure 2.14 for large $\beta$. It is clear that the ion flow for large $\beta$ (Case IV) decreases much faster than the low $\beta$ (Case II). In other words, the ions are demagnetized earlier in high beta case. The scale that two-fluid analysis separates MHD and kinetic Alfvén waves is when $kd_i = \frac{c_m}{c_s}$. This scale is very close to $k_\perp \rho_i = 1$ for the low $\beta$ case which is shown in Figure 2.13. On the other hand, $kd_i = \frac{c_m}{c_s}$ does not accurately describe the transition of MHD to kinetic Alfvén waves in high $\beta$ plasma, also apparent in Figure 2.14.

## 2.5 Landau Damping

Landau damping is a collisionless damping mechanism exhibited in plasmas. This mechanism is particularly interesting because techniques from complex analysis are used to recover the the damping rates of plasma waves [Landau, 1946]. It was experimentally verified in 1964 by Malmberg and Wharton [1964]. Before we dive into the mathematical formulation of Landau damping, it is helpful to develop some basic physical intuition of this particular mechanism. The damping of plasma waves happen in the fields, both for the electric and magnetic fields. Therefore, a very simple question arises as to where does the energy stored in fields transfer too. It is the particles that gain energy and thereby increases kinetic energy. Another similar damping is called the cyclotron resonance when the Doppler-shifted frequency $\omega - k_\parallel v_\parallel$ is equal to an integer multiple of gyro-frequency $\Omega_c$.
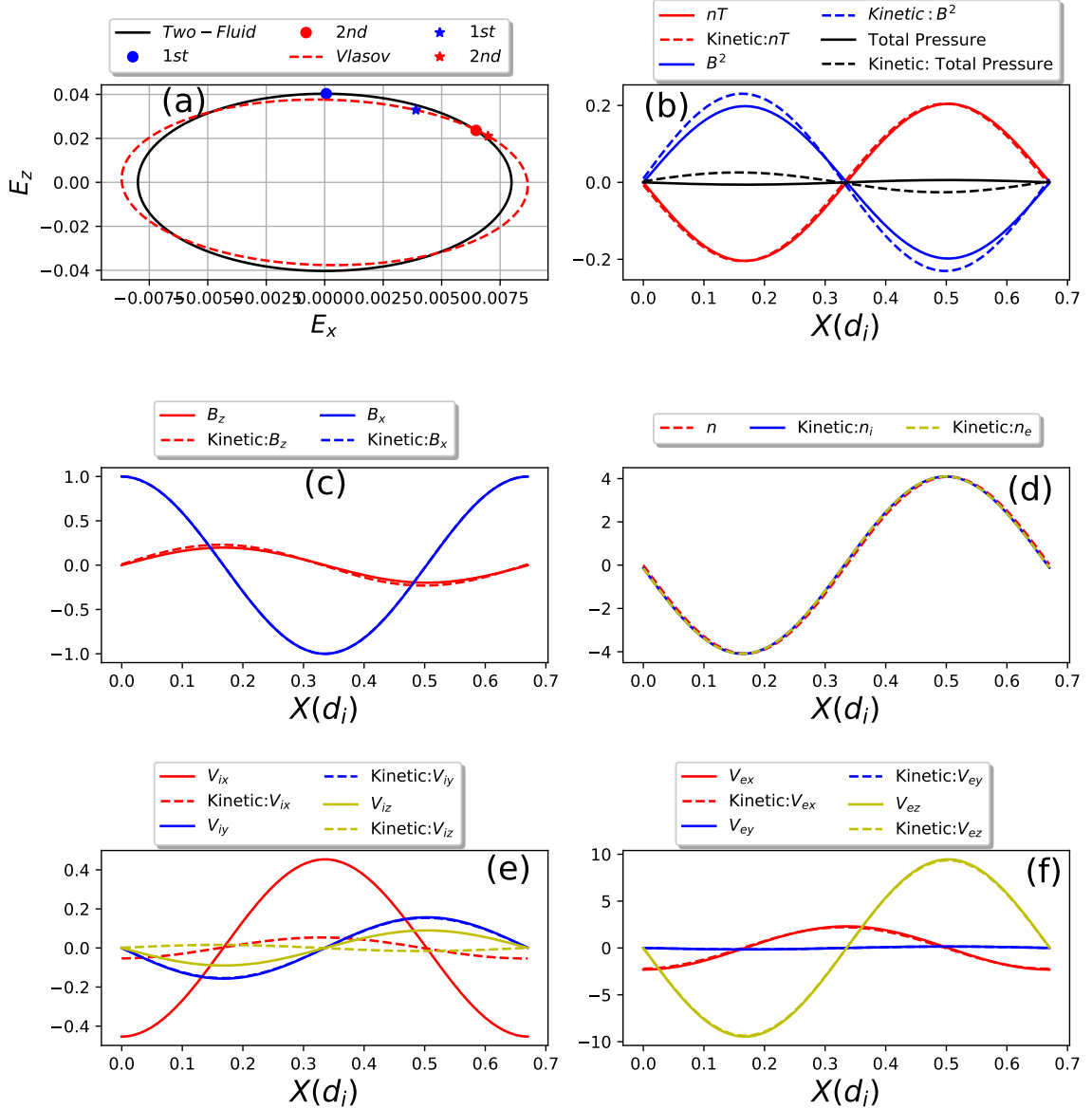
**Figure 2.7:** Case II: Wave number $kd_i = 9.36$ is chosen such that Equation 2.19 matches with the dashed blue curve in Figure 2.2(b) within the KAW regime. (a) $x$ and $y$ components of electric field are plotted along horizontal and vertical axis as a function of $x/d_i$. The range of $x/d_i$ is defined by $2\pi/kd_i$. (b)Pressure balance holds more-or-less in both models. (c) The perturbation of the magnetic field in the $z$-direction is small compared to the $x$-direction. (d) The density perturbation is quite large for this parameter regime. (e) Ion velocities of each component. Except for $y$ and $z$ components, the fluid model and the kinetic model differ significantly, however, they have the same order of magnitude. (f) Electron velocities for both the models are similar.
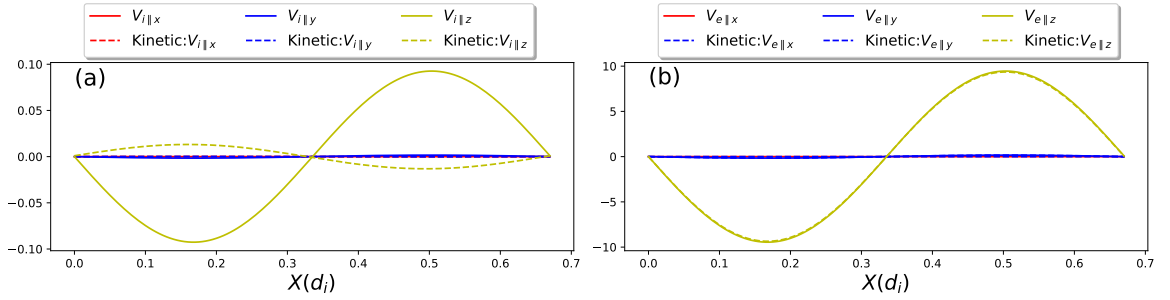
**Figure 2.8:** Case II: Components of parallel flows are shown. (a)Largest parallel flows are in the $z$-direction. (b) Electron flows are primarily in the z-direction.
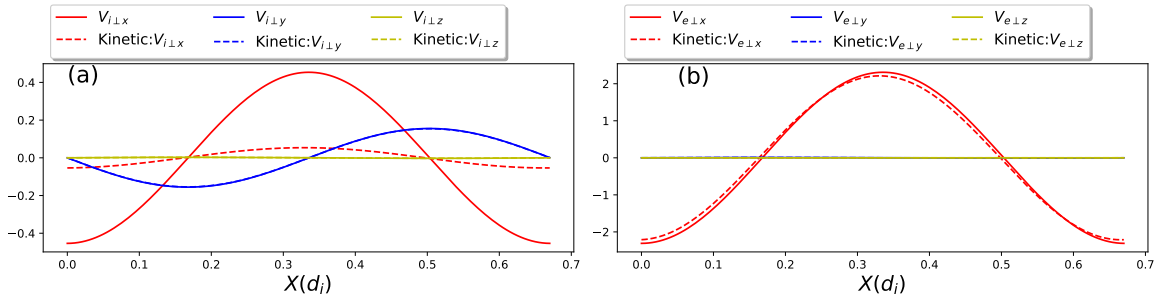


**Figure 2.9:** Case II: Components of perpendicular flows are shown. (a) The largest ion flows are in the $x$ and $y$-directions. The kinetic calculation shows that $v_{i\perp y}$ is the largest flow whereas two-fluid model shows in the $x$-direction. (b) Most perpendicular electron flows are in the $x$-direction
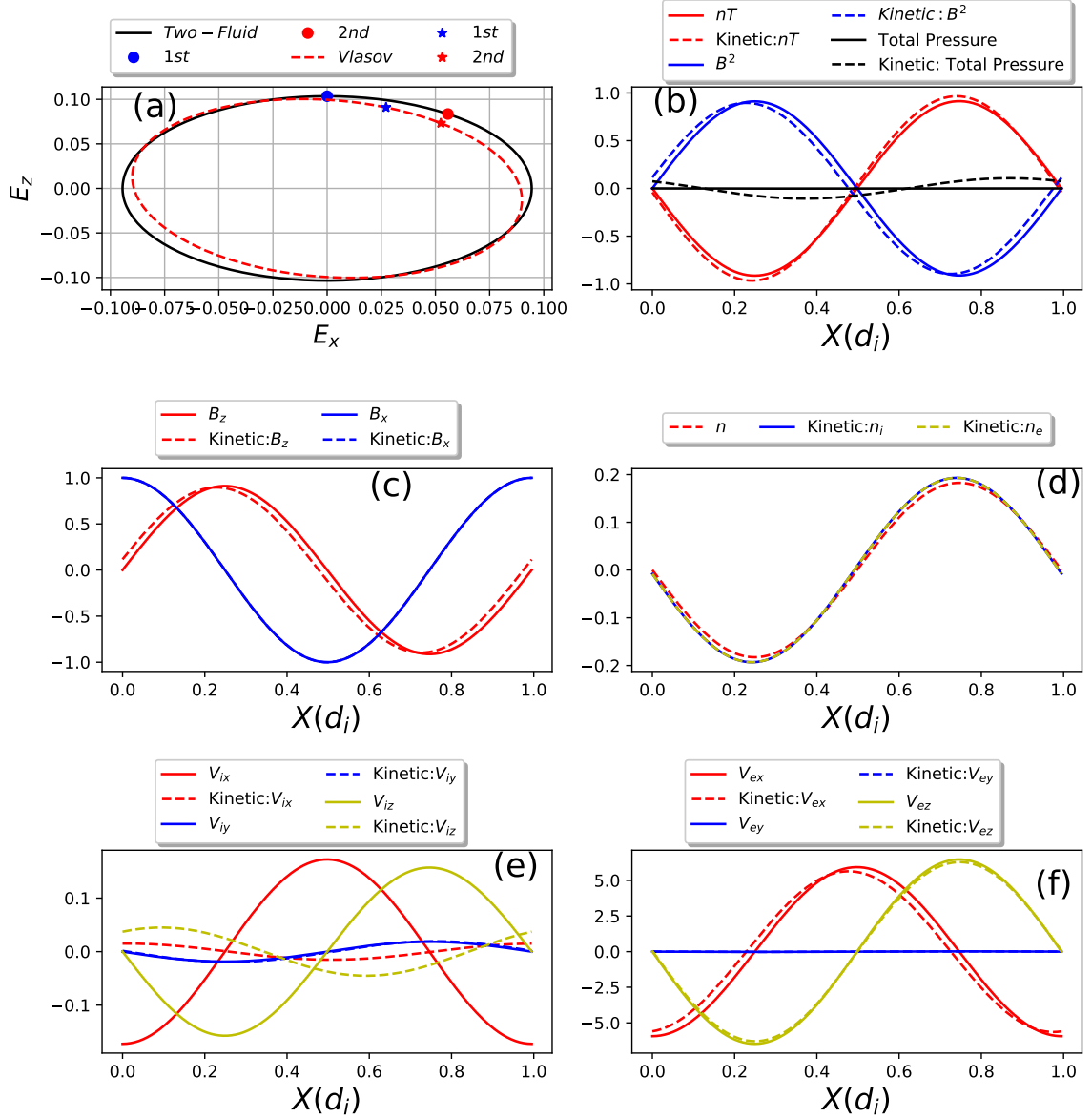
**Figure 2.10:** Case IV: Wave number $kd_i = 6.31$ is chosen such that Equation 2.19 matches with the dashed blue curve in Figure 2.3(b) within the KAW regime . (a) $x$ and $y$ components of electric field are plotted along horizontal and vertical axis. The range of $x/d_i$ is defined by $2\pi/kd_i$. The electric field rotating in the $xz$-plane is approximately circular in this parameter regime. Right handed if one were to look at $\vec{k}$ direction. (b) The pressure balance holds more-or-less in both models (c) The perturbation of magnetic field in the $z$-direction is about the same as x-direction. (d) Density perturbation is small for this parameter regime. (e) Ion velocities of each component. Except for y and z components, the fluid model and the kinetic model differ significantly, however, they have the same order of magnitude. (f) Electron velocities for both the models are similar.
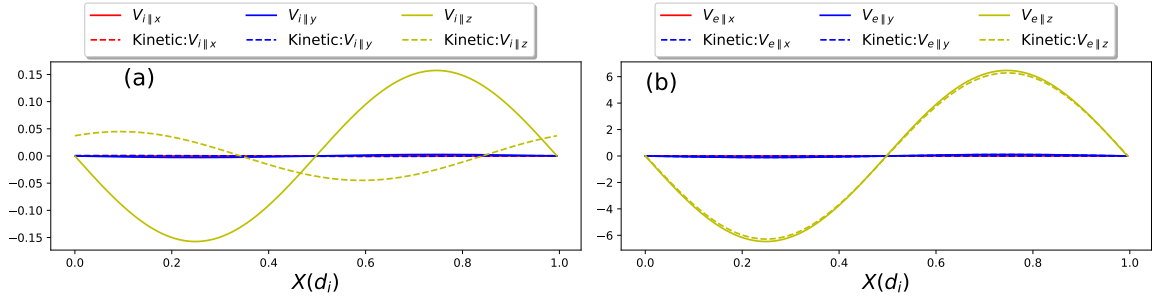
**Figure 2.11:** Case IV: Components of parallel flows are shown. (a) Largest parallel ion flows are in the $z$-direction. (b) Electron flows are primarily in the $z$-direction.
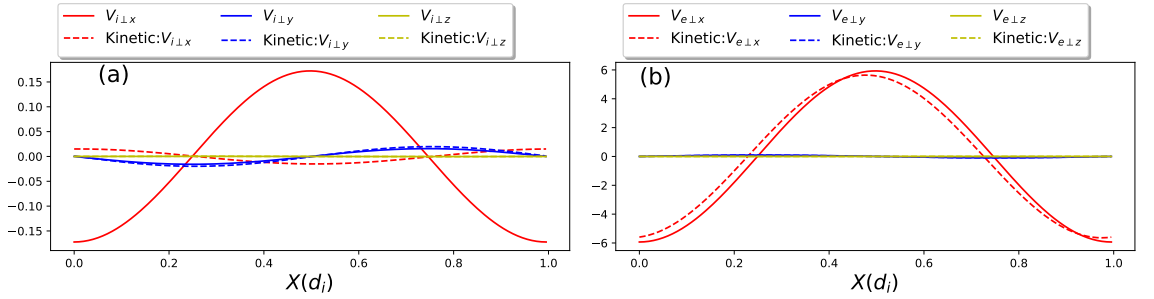


**Figure 2.12:** Case IV: Components of perpendicular flows are shown. (a) Kinetic calculation shows that perpendicular ion flows are in the $x$ and $y$ direction whereas the two-fluid analysis shows they are mostly in the $x$-direction. (b) Perpendicular electron flows are primarily in the $x$-direction.
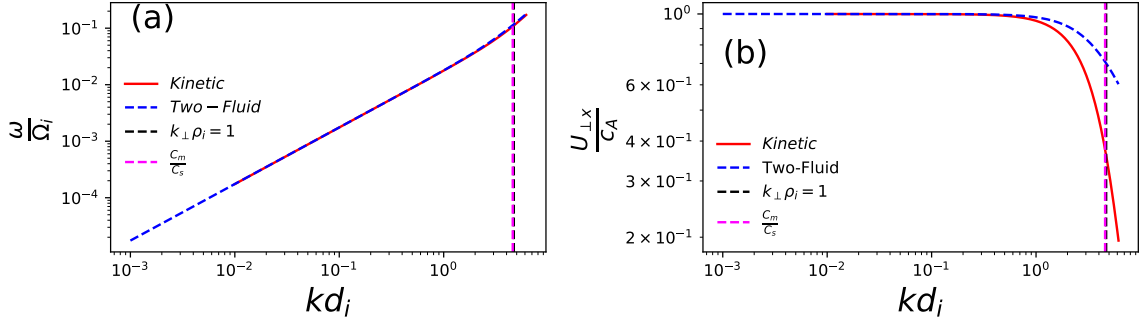
**Figure 2.13:** Case II: (a) Frequency $\frac{\omega}{\Omega_i}$ vs wavenumber $kd_i$ of the kinetic Alfvén wave branch is shown for two-fluid and kinetic dispersion solver. They don't have significant differences when $k_\perp \rho_i = 1$. (b) The response of ions in KAWs are somewhat similar in two-fluid and full kinetic description.
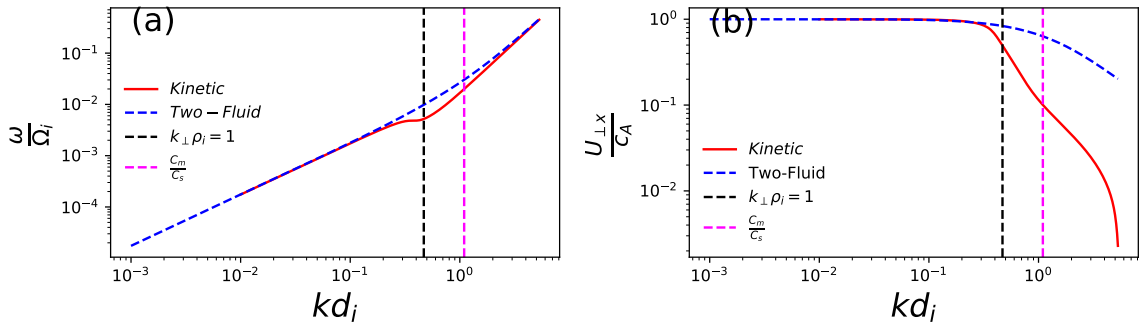


**Figure 2.14:** Case IV: (a) Frequency $\frac{\omega}{\Omega_i}$ vs wavenumber $kd_i$ of the kinetic Alfvén wave branch is shown for two-fluid and kinetic dispersion solver. They start to differ when $k_\perp \rho_i = 1$. (b) The respose of ions in KAWs are very different in two-fluid and full kinetic description. Ion flows in the perpendicular direction decreases rapidly after $k_\perp \rho_i = 1$ in contrast to Case II.

A brief analogy of Landau damping in plasma can be found from an example shown in Figure 2.15. This is similar to surf-boarder riding a wave example usually shown in textbooks e.g. [Chen, 1974]. Skiing provides a natural analogy for Landau damping of fields when particles gain energy. The group of bears in the back can be considered as a plasma wave riding a potential surface while the front bear A is the individual particle that gains energy. The hill in the picture can be regarded as the electric potential that governs the trajectory of particles. There are multiple bears downhill skiing. Three bears at the back are moving together with constant velocity $v_c$ and Bear A in Figure 2.15 is moving with velocity $v$. Bear A is attached to a rope that is tied to the group in the back. If $v_c < v$ then this would slow down Bear A because the rope acts as a tension force. In doing so, Bear A slows down compensating this via energy transfer. Similarly, when the positions of the group and Bear A are reversed, Bear A gains speed if $v_c > v$. The force due to an electric field acts similar to the tension force in the rope.

To illustrate this concept in terms of distribution of particles, in Figure 2.16 is shown a one dimensional distribution function $f(v)$. If the distribution function $f$ has a negative slope close to the resonant particles then on average, energy from the wave is transferred to resonant particles as there are more particles to the left of the distribution $f$. This is seen when the Vlasov equation is linearized, and the dispersion relation in the electrostatic approximation takes the form

$$\frac{\omega_p^2}{k^2} \int_{-\infty}^{\infty} \frac{\frac{\partial f_0}{\partial v}}{v - \frac{\omega}{k}} dv = 1 \tag{2.32}$$

where $f_0$ is the unperturbed part of the distribution function $f$. The simplest choice for $f_0$ is Maxwell-Boltzmann distribution. The solution to this Equation 2.32 depends on where $\omega$ lies in the complex plane of $v$. The concept of analytical continuation comes in useful as the integral in Equation 2.32 is ill-posed at $v = \frac{\omega}{k}$. Using this concept, Landau proposed integral contours eliminating this difficulty. Thus, we may further
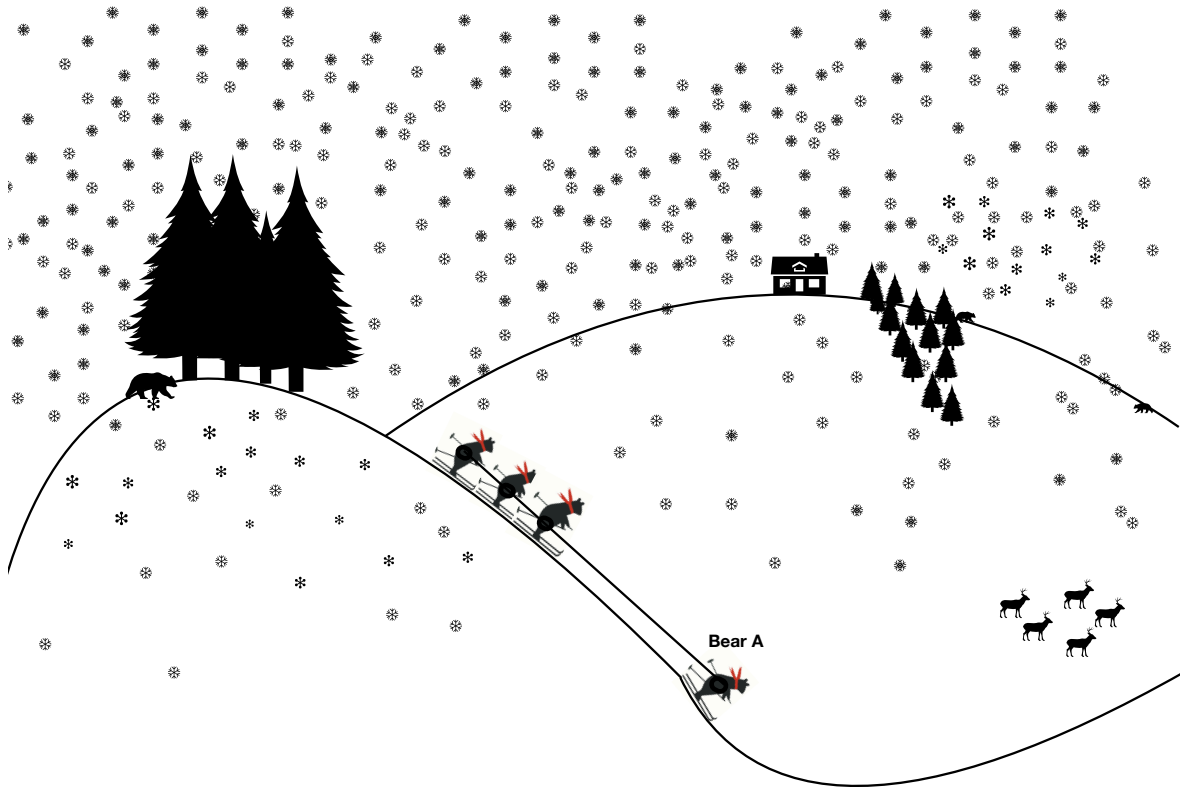
**Figure 2.15:** Skiing provides a natural analogy for Landau damping of fields when particles gain energy. The group of bears in the back can be considered as a plasma wave while the front bear A is the individual particle that gains energy.
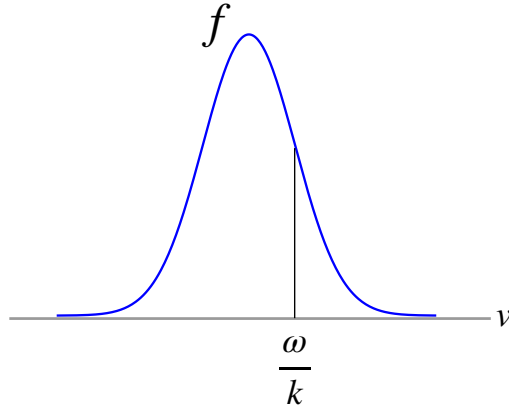
**Figure 2.16:** A one dimensional distribution function $f$ of particles: Particles with velocity close to the wave phase speed $\frac{\omega}{k}$ are in resonance.

write Equation 2.32 conditionally as

$$\frac{\omega_p^2}{k^2} \int_{-\infty}^{\infty} \frac{\frac{\partial f_0}{\partial v}}{v - \frac{\omega}{k}} dv = 1, \ \text{Im}(\omega) > 0, \tag{2.33}$$

$$\frac{\omega_p^2}{k^2} \int_{-\infty}^{\infty} \frac{\frac{\partial f_0}{\partial v}}{v - \frac{\omega}{k}} dv - \frac{2\pi i \omega_p^2}{k^2} \frac{\partial f_0(\omega/k)}{\partial v} = 1, \ \text{Im}(\omega) < 0 \tag{2.34}$$

where integrals are taken along the real $v$ axis. Also note that the plasma dispersion function $Z(\xi)$ has a similar form like the integral in Equation 2.32. As we will see in subsequent discussion of Landau damping of kinetic Alfvén wave, the dispersion tensor contains plasma dispersion function $Z$ in all of its elements. In other words, Landau damping terms are traced to this plasma dispersion function $Z$. More illuminating discussion on physical mechanism of Landau damping is shown in Dawson [1961].

Now that we have some level of intuitive understanding of Landau damping, we will explore a bit more on the mathematical formalism of how linear Landau damping works. In order to get quantitative measure of collisionless damping rate, we have to treat plasma as a kinetic system. In other words, we invoke the Vlasov equation. The fluid formulation of plasma can give other kinds of dissipation e.g. viscous dissipation, but the collisionless damping can only be explored using kinetic formulation of plasma.

Much of the kinetic formulation of plasmas can be found in standard textbooks [Chen, 1974, Krall and Trivelpiece, 1986, Stix, 1992], so we won't go through the details of rederiving the linear dispersion tensor. We use general dispersion tensors provided in standard textbooks and appropriate approximations are discussed to derive kinetic Alfvén wave damping rate.

## 2.6   Derivation of Landau Damping of Kinetic Alfvén Wave

In order to derive Landau damping of kinetic Alfvén wave, we have to inspect the full linear dispersion tensor of a hot magnetized uniform plasma. We follow a similar method presented in Lysak and Lotko [1996], however, we further extend this formalism to analytically calculate kinetic Alfvén wave damping rate. The following steps are taken to get the dispersion relation. For simplicity, we only take two species, namely ions and electrons. The perturbed current density is

$$\vec{J_1} = n_0 e \int (f_{1i} - f_{1e})\vec{v}d\vec{v}, \tag{2.35}$$

where $f_1$ is the perturbed distribution governed by the Vlasov equation. The Ohm's law is

$$\vec{J} = \overleftrightarrow{\sigma} \cdot \vec{E} \tag{2.36}$$

where $\overleftrightarrow{\sigma}$ is the conductivity tensor. Substituting Equation 2.36 into Maxwell's equations we get

$$\vec{\nabla} \times \vec{E} = -\frac{1}{c}\frac{\partial \vec{B}}{\partial t} \tag{2.37}$$

$$\vec{\nabla} \times \vec{B} = \frac{1}{c}\left(\frac{\partial \vec{E}}{\partial t} + 4\pi\overleftrightarrow{\sigma} \cdot \vec{E}\right). \tag{2.38}$$

Assuming all perturbed quantities are proportional to $\exp[i(\vec{k} \cdot \vec{x} - \omega t)]$ and linearizing Equations 2.37 and 2.38, we define the dielectric tensor as

$$\overleftrightarrow{\epsilon} = \mathbf{1} + i\frac{4\pi}{\omega}\overleftrightarrow{\sigma}. \tag{2.39}$$

Solving for $\vec{E}$ and $\overleftrightarrow{\epsilon}$ from Equations 2.37 and 2.38, we get

$$k^2\vec{E} - (\vec{k} \cdot \vec{E})\vec{k} - \frac{\omega^2}{c^2}\overleftrightarrow{\epsilon} \cdot \vec{E} = 0, \tag{2.40}$$

46

which in the tensorial form is

$$(k^2\delta_{ij} - k_i k_j - \frac{\omega^2}{c^2}\epsilon_{ij})E_j = 0, \tag{2.41}$$

where $\delta_{ij}$ is Kronecker's delta. The dispersion relation is given by

$$\det(k^2\delta_{ij} - k_i k_j - \frac{\omega^2}{c^2}\epsilon_{ij}) = 0 \tag{2.42}$$

If the wavevector $\vec{k}$ lies in the $xz$-plane and the unperturbed $\vec{B_0}$ points in the $\hat{z}$-direction, this relation can be written as

$$\det \begin{pmatrix} \epsilon_{xx} - n_\parallel^2 & \epsilon_{xy} & \epsilon_{xz} + n_\parallel n_\perp \\ -\epsilon_{xy} & \epsilon_{yy} - n^2 & \epsilon_{yz} \\ \epsilon_{xz} + n_\parallel n_\perp & -\epsilon_{yz} & \epsilon_{zz} - n_\perp^2 \end{pmatrix} = 0, \tag{2.43}$$

where $n_\parallel^2 = k_\parallel^2 c^2/\omega^2$, $n_\perp^2 = k_\perp^2 c^2/\omega^2$ and $n^2 = k^2 c^2/\omega^2$ are the parallel, perpendicular and total index of refraction. The $\epsilon_{ij}$'s are the elements of the dielectric tensor defined below. The convention used is taken from a textbook [Chen, 1974].

$$\epsilon_{xx} = 1 + \sum_s \frac{\omega_{ps}^2}{\omega^2}\xi_{0s} \sum_{n=-\infty}^{\infty} \frac{n^2\Gamma_n(\mu_s)}{\mu_s} Z(\xi_{ns}) \tag{2.44}$$

$$\epsilon_{yy} = 1 + \sum_s \frac{\omega_{ps}^2}{\omega^2}\xi_{0s} \sum_{n=-\infty}^{\infty} \left( \frac{n^2\Gamma_n(\mu_s)}{\mu_s} - 2\mu_s\Gamma_n'(\mu_s) \right) Z(\xi_{ns}) \tag{2.45}$$

$$\epsilon_{zz} = 1 - \sum_s \frac{\omega_{ps}^2}{\omega^2}\xi_{0s} \sum_{n=-\infty}^{\infty} \xi_{ns}\Gamma_n(\mu_s)Z'(\xi_{ns}) \tag{2.46}$$

$$\epsilon_{xy} = -i \sum_s \frac{\omega_{ps}^2}{\omega^2}\xi_{0s} \sum_{n=-\infty}^{\infty} n\Gamma_n'(\mu_s)Z(\xi_{ns}) \tag{2.47}$$

$$\epsilon_{xz} = \sum_s \frac{\omega_{ps}^2}{\omega^2}\xi_{0s} \sum_{n=-\infty}^{\infty} \frac{n\Gamma_n(\mu_s)}{\sqrt{2\mu_s}}\xi_{ns}Z(\xi_{ns}) \tag{2.48}$$

$$\epsilon_{yz} = i \sum_s \frac{\omega_{ps}^2}{\omega^2}\xi_{0s} \sum_{n=-\infty}^{\infty} \sqrt{\frac{\mu_s}{2}}\Gamma_n'(\mu_s)\xi_{ns}Z(\xi_{ns}), \tag{2.49}$$

where s is the species, $\omega_{ps} = \sqrt{\frac{4\pi n_s q_s^2}{m_s}}$ is the plasma frequency of species s, $\xi_{ns} = \frac{\omega - n\Omega_s}{k_\parallel a_s}$, $\Omega_s = \frac{q_s B}{m_s c}$ is the cyclotron frequency of species s (negative for electrons), $a_s = \sqrt{\frac{2T_s}{m_s}}$ is the modified thermal velocity, and $\mu_s = \frac{k_\perp^2 T_s}{m_s \Omega_s^2}$. The function $\Gamma_n(\mu_s) = e^{-\mu_s} I_n(\mu_s)$

where $I_n(\mu_s)$ is the modified Bessel function. The derivative of this function is $\Gamma'_n(\mu_s) = (I'_n(\mu_s) - I_n(\mu_s))e^{-\mu_s}$. The function $\Gamma_n(\mu_s) = e^{-\mu_s} I_n(\mu_s)$ is symmetric about its order i.e, $\Gamma_n(\mu_s) = \Gamma_{-n}(\mu_s)$. A sum rule of this function is given by $\sum_{n=-\infty}^{\infty} \Gamma_n(\mu_s) = 1$. Due to its symmetric property, it is easy to show $\sum_{n=1}^{\infty} \Gamma_n(\mu_s) = \frac{1 - \Gamma_0(\mu_s)}{2}$. Lastly, the plasma dispersion function $Z(\xi)$ is described in textbooks [Chen, 1974, Krall and Trivelpiece, 1986, Stix, 1992] and its derivative is given by $Z'(\xi) = -2(1 + \xi Z(\xi))$. This plasma dispersion function is

$$Z(\xi) = \frac{1}{\sqrt{\pi}} \int_{-\infty}^{\infty} \frac{e^{-t^2}}{t - \xi} dt. \tag{2.50}$$

The elements of the dielectric tensor $\epsilon_{ij}$ are calculated from Equation 2.35. The $x$-component of current density from Equation 2.36 is $J_{x1} = \sigma_{xx} E_{x1} + \sigma_{xy} E_{y1} + \sigma_{xz} E_{z1}$. $f_1$ is substituted from the linearized Vlasov equation[2] and $\sigma_{xx}$ is read off as a coefficient of $E_{x1}$. And finally, $\epsilon_{xx} = 1 + i\frac{4\pi}{\omega} \sigma_{xx}$ is calculated from Equation 2.39. Similarly, all the elements of the dielectric tensor are calculated. The general solutions to Equation 2.43 are calculated numerically, but, in the limit of low frequency $\omega \ll \Omega_s$ and long parallel wavelength $k_\parallel a_s \ll \Omega_s$, solutions are somewhat tractable. Here we consider only the regime $\beta \ll 1$. For $n \neq 0$, using these approximation gives $|\xi_{ns}| \gg 1$. Ignoring higher order terms, $Z(\xi_{ns}) \sim -\frac{1}{\xi_{ns}} = -\frac{k_\parallel}{\omega - n\Omega_s}$. If $n = 0$, it has no contribution to Equation 2.44 and expanding, we get

$$\epsilon_{xx} = 1 - \sum_s \frac{\omega_{ps}^2}{\omega^2} \xi_{0s} \left[ \sum_{n=1}^{\infty} \frac{n^2 \Gamma_n(\mu_s)}{\mu_s} \frac{k_\parallel a_s}{\omega - n\Omega_s} + \sum_{n=-1}^{-\infty} \frac{n^2 \Gamma_n(\mu_s)}{\mu_s} \frac{k_\parallel a_s}{\omega - n\Omega_s} \right]. \tag{2.51}$$

Substituting $n = -m$ is the third term of Equation 2.51 and noting that $\Gamma_m(\mu_s) = \Gamma_{-m}(\mu_s)$ and since $n$ is a dummy variable, we have

$$\epsilon_{xx} = 1 - \sum_s \frac{2\omega_{ps}^2}{\mu_s} \sum_{n=1}^{\infty} \frac{n^2 \Gamma_n(\mu_s)}{\omega^2 - n^2 \Omega_s^2} \tag{2.52}$$

---

[2] The method of characteristics is generally used in textbooks to solve for the perturbed distribution $f_1$. In this method, the integration is carried out along the particle's unperturbed trajectory. However, $f_1$ used in ref. [Chen, 1974] is obtained by direct integration over a gyro angle $\alpha$ in the plane perpendicular to $\hat{z}$ in guiding-center phase space. In this case, $f_1$ has to be periodic function of $\alpha$, therefore restricting solutions of the linearized Vlasov equation.

In the denominator, $\omega^2$ is dropped in the low frequency approximation. Using the property of $\Gamma_n(\mu_s)$ we have

$$\epsilon_{xx} = 1 + \sum_s \frac{2\omega_{ps}^2}{\mu_s \Omega_s^2} \sum_{n=1}^{\infty} \Gamma_n(\mu_s) \tag{2.53}$$

$$= 1 + \sum_s \frac{\omega_{ps}^2}{\Omega_s^2} \frac{1 - \Gamma_0(\mu_s)}{\mu_s} \tag{2.54}$$

The electron contribution is neglected because $\frac{\omega_{pe}^2}{\Omega_e^2} \ll \frac{\omega_{pi}^2}{\Omega_i^2} = \frac{c^2}{c_A^2}$. Thus, we have

$$= 1 + \sum_s \frac{c^2}{c_A^2} \frac{1 - \Gamma_0(\mu_i)}{\mu_i} \tag{2.55}$$

For $\mu_i \ll 1$, $\Gamma_0(\mu_i) \approx 1 - \mu_i + \frac{3}{4}\mu_i^2$. Therefore, $\frac{1 - \Gamma_0(\mu_i)}{\mu_i} \approx 1$ in this limit. MHD is valid in the small ion gyroradius limit. So, taking the dispersion relation $\epsilon_{xx} - n_\parallel^2 = 0$, we get $\omega^2 = k_\parallel^2 c_A^2$ which is the shear Alfvén wave dispersion relation. Note that $\frac{c^2}{c_A^2} \gg 1$ is assumed in Equation 2.55. We expand Equation 2.45 and note that the first term is $\epsilon_{xx}$, we have

$$\epsilon_{yy} = \epsilon_{xx} - \sum_s \frac{2\omega_{ps}^2}{\omega^2} \xi_{0s} \mu_s \Gamma_0'(\mu_s) Z(\xi_{0s})$$
$$- \sum_s \frac{2\omega_{ps}^2}{\omega^2} \xi_{0s} \mu_s \sum_{n=1}^{\infty} \left[ \Gamma_n'(\mu_s) Z(\xi_{ns}) + \Gamma_{-n}'(\mu_s) Z(\xi_{-ns}) \right]. \tag{2.56}$$

Here we use Bessel function properties to get $\Gamma_n'(\mu_s) = \Gamma_{n+1}(\mu_s) - \Gamma_n(\mu_s) + \frac{n}{\mu_s}\Gamma_n(\mu_s)$. Using this relation and a bit of algebra, it can be shown that $\frac{n}{\mu_s}\Gamma_n(\mu_s)$ is small and what is left is

$$\epsilon_{yy} = \epsilon_{xx} - \sum_s \frac{2\omega_{ps}^2}{\omega^2} \xi_{0s} \mu_s \Gamma_0'(\mu_s) Z(\xi_{0s})$$
$$- \sum_s \frac{\omega_{ps}^2}{\omega^2} \frac{2\omega}{k_\parallel a_s} \mu_s \left[ -\sum_{n=1}^{\infty} \Gamma_n(Z_+ + Z_-) + \sum_{n=1}^{\infty} (\Gamma_{n+1} Z_+ + \Gamma_{-n+1} Z_-) \right], \tag{2.57}$$

where the argument of $\Gamma$ is dropped and $\xi_+ = \xi_{ns}$, $\xi_- = \xi_{-ns}$, $Z_+ = Z(\xi_{ns})$, $Z_- = Z(\xi_{-ns})$, $\Gamma_n(\mu_s) = \Gamma_+$ and $\Gamma_{-n}(\mu_s) = \Gamma_-$ are often used for convenience. Also, $(Z_+ + Z_-) \approx \frac{2k_\parallel a_s}{n^2} \frac{\omega}{\Omega^2}$ in this limit, so

$$
\begin{aligned}
\epsilon_{yy} = \epsilon_{xx} &- \sum_s \frac{2\omega_{ps}^2}{\omega^2} \xi_{0s} \mu_s \Gamma_0'(\mu_s) Z(\xi_{0s}) \\
&+ \sum_s 4\mu_s \frac{\omega_{ps}^2}{\omega^2} \sum_{n=1}^{\infty} \frac{\Gamma_n}{n^2} \\
&- \sum_s \frac{\omega_{ps}^2}{\omega^2} \frac{2\omega}{k_\parallel a_s} \mu_s \left[ \sum_{n=1}^{\infty} (\Gamma_{n+1} Z_+ + \Gamma_{-n+1} Z_-) \right].
\end{aligned}
\tag{2.58}
$$

Using Bessel function properties[3] and $\Gamma_{-n+1} = \Gamma_{n-1}$, the last term inside the brackets of the right hand side of Equation 2.58 is

$$
\begin{aligned}
\sum_{n=1}^{\infty} \Gamma_{n+1}(Z_+ + Z_-) &+ \sum_{n=1}^{\infty} \frac{2n\Gamma_n(\mu_s)}{\mu_s} Z_- \\
&\approx \sum_{n=1}^{\infty} \Gamma_{n+1}(\mu_s) \frac{2}{n^2} \frac{\omega}{\Omega_s} \frac{k_\parallel a_s}{\Omega_s} - \frac{k_\parallel a_s}{\Omega_s} \frac{2}{\mu_s}
\end{aligned}
$$

Using this relation, the last term of Equation 2.58 is

$$
\sum_s \frac{4\omega_{ps}}{\Omega_s} \frac{\omega_{ps}}{\omega} - \sum_s 4\mu_s \frac{\omega_{ps}^2}{\omega^2} \sum_{n=1}^{\infty} \frac{\Gamma_{n+1}}{n^2}.
$$

The first expression is dropped considering a low frequency approximation and the second expression above scales like the third term in Equation 2.58 which we drop in the cold plasma approximation and small gyroradius limit. The second term in Equation 2.58 is calculated by noting that $\Gamma_0'(\mu_s) = \Gamma_1(\mu_s) - \Gamma_0(\mu_s)$, which is

$$
\begin{aligned}
\sum_s \frac{2\omega_{ps}^2 \mu_s}{\omega_s^2} &\left[ \Gamma_1(\mu_s) - \Gamma_0(\mu_s) \right] \\
&\approx -\frac{2k_\perp^2}{\omega^2} \left( \omega_{pe}^2 \frac{T_e}{m_e \Omega_e^2} + \omega_{pi}^2 \frac{T_i}{m_i \Omega_i^2} \right) \\
&= -\frac{k_\perp^2 c^2}{\omega^2} \frac{8\pi n(T_i + T_e)}{B^2}.
\end{aligned}
$$

---

[3] $\Gamma_{n-1}(x) = i^{-(n-1)} J_{n-1}(ix) e^{-x} = ii^{-n} J_{n-1}(ix) e^{-x} = i\{\frac{2n}{ix} i^{-n} J_n(ix) e^{-x} - i^1 i^{-(n+1)} J_{n+1}(ix) e^{-x}\} = \frac{2n}{x} \Gamma_n(x) + \Gamma_{n+1}(x)$. Note we have used the Bessel function property $J_{n-1}(x) = \frac{2n}{x} J_n(x) - J_{n+1}(x)$.

We cast Equation 2.58 as

$$\epsilon_{yy} = 1 + \frac{c^2}{c_A^2} - \frac{8\pi n(T_i + T_e)}{B^2}\frac{k_\perp^2 c^2}{\omega^2}. \tag{2.59}$$

Now, it is clear that the highest order of $\epsilon_{yy}$ is $\sim \frac{c^2}{c_A^2}$. Setting $\epsilon_{yy} - n^2 = 0$ gives the fast mode frequency[4] $\omega^2 = k^2 c_A^2 + k_\perp^2 c_s^2$. This will come in handy later. The last diagonal term can be simplified using similar technique.

$$\epsilon_{zz} = 1 - \sum_s \frac{\omega_{ps}^2}{\omega^2}\frac{\omega}{k_\parallel a_s}\Big[\xi_{0s}\Gamma_0(\mu_s)Z'(\xi_{0s})$$
$$+ \sum_{n=1}^{\infty}\Gamma_n(\mu_s)\{\xi_{ns}Z'(\xi_{ns}) + \xi_{-ns}Z'(\xi_{-ns})\}\Big] \tag{2.60}$$

Expanding $Z'$ in the limit $|\xi| \gg 1$, the last term in Equation 2.60 within $\sum_{n=1}^{\infty}$ becomes

$$\sum_{n=1}^{\infty}\Gamma_n(\mu_s)\Big[ - 2\xi_{ns}(1 + \xi_{ns}Z(\xi_{ns})) - 2\xi_{-ns}(1 + \xi_{-ns}Z(\xi_{-ns}))\Big]$$
$$\approx \sum_{n=1}^{\infty}\Gamma_n(\mu_s)\Big[\frac{1}{\xi_{ns}} + \frac{1}{\xi_{-ns}}\Big] = \sum_{n=1}^{\infty}\Gamma_n(\mu_s)\frac{2\omega k_\parallel a_s}{\omega^2 - n^2\Omega_s^2}.$$

Equation 2.60 takes the following form in the low frequency approximation ($\omega^2 \ll \Omega_s^2$):

$$\epsilon_{zz} = 1 + \sum_s \frac{2\omega_{ps}^2}{k_\parallel^2 a_s^2}\Gamma_0(\mu_s)\Big[1 + \xi_{0s}Z(\xi_{0s})\Big] + \sum_s \frac{\omega_{ps}^2}{\Omega_s^2}\sum_{n=1}^{\infty}\frac{2\Gamma_n(\mu_s)}{n^2} \tag{2.61}$$

Here we neglect the last term because $\frac{k_\parallel^2 a_s^2}{2\Omega_s^2} \ll 1$ by the long parallel wavelength approximation. Expanding the second term we get

$$\epsilon_{zz} = 1 + \frac{\Gamma_0(\mu_e)}{k_\parallel^2 \lambda_{De}^2}\Big[1 + \xi_{0e}Z(\xi_{0e})\Big] - \frac{\omega_{pi}^2}{\omega^2}\Gamma_0(\mu_i), \tag{2.62}$$

where we have used $\frac{\lambda_{Ds}^2}{a_s^2} = \frac{1}{2\omega_{ps}^2}$. The ion term is neglected again for the low $\beta \ll 1$ case[5]. Equation 2.62 is simply given by

$$\epsilon_{zz} = 1 + \frac{\Gamma_0(\mu_e)}{k_\parallel^2 \lambda_{De}^2}\Big[1 + \xi_{0e}Z(\xi_{0e})\Big]. \tag{2.63}$$

---

[4] $\epsilon_{yy} - n^2 = 0 \Rightarrow 1 + \frac{c^2}{c_A^2} - \beta\frac{k_\perp^2 c^2}{\omega^2} - \frac{k^2 c^2}{\omega^2} = 0 \Rightarrow \omega^2 = (k^2 + \beta k_\perp^2)c_A^2 = k^2 c_A^2 + c_s^2 k_\perp^2$

[5] The ratio of ion term to electron term is given by $\frac{\omega_{pi}^2}{\omega^2}k_\parallel^2\lambda_{De}^2 = k_\parallel^2\frac{c_s^2}{\omega^2}$. For shear Alfvén waves $\omega^2 \approx k_\parallel^2 c_A^2$ and the ratio becomes $\beta$. $\beta \ll 1$ in our approximation. Hence, ion term can be neglected.

Setting $\epsilon_{zz} - n_\perp = 0$ gives the ion acoustic frequency[6]. Moving on to the off-diagonal terms, they become small for low-$\beta$ limit and vanish for a cold plasma limit. First,

$$
\begin{aligned}
\epsilon_{xz} &= \sum_s \frac{\omega_{ps}^2}{\omega^2} \xi_{0s} \frac{1}{\sqrt{2\mu_s}} \sum_{n=1}^\infty \{ n\Gamma_n (\xi_+ Z_+ - \xi_- Z_-) \} \\
&= \sum_s \frac{\omega_{ps}^2}{\omega^2} \xi_{0s} \frac{1}{\sqrt{2\mu_s}} \sum_{n=1}^\infty \{ n\Gamma_n (1/\xi_-^2 - 1/\xi_+^2) \} \\
&= \sum_s \frac{\omega_{ps}^2}{\omega^2} \xi_{0s} \frac{1}{\sqrt{2\mu_s}} \sum_{n=1}^\infty \left[ n\Gamma_n \left( \frac{-4}{n^3} \frac{k_\parallel^2 a_s^2}{\Omega_s^2} \frac{\omega}{\Omega_s} \right) \right] \\
&= -\sum_s \frac{2\omega_{ps}^2}{\omega^2} \frac{k_\parallel}{k_\perp} \sum_{n=1} \frac{\Gamma_n}{n^2}
\end{aligned}
\tag{2.64}
$$

Under the assumption that $\frac{k_\parallel}{k_\perp} \ll 1$, Equation 2.64 is dropped. In general, the remaining two off-diagonal terms cannot be neglected. We expand Equation 2.49

$$
\begin{aligned}
\epsilon_{yz} &= i \sum_s \frac{\omega_{ps}^2}{\omega^2} \xi_{0s} \sqrt{\frac{\mu_s}{2}} \left[ \Gamma_0'(\mu_s) \xi_{0s} Z(\xi_{0s}) + \sum_{n\neq0} \Gamma_n'(\mu_s) \xi_{ns} Z(\xi_{ns}) \right] \\
&= i \sum_s \frac{\omega_{ps}^2}{2\omega^2} \frac{k_\perp}{k_\parallel} \frac{\omega}{\Omega_s} \left[ \Gamma_0'(\mu_s) \xi_{0s} Z(\xi_{0s}) + \sum_{n=1}^\infty \{ \Gamma_+' \xi_+ Z_+ + \Gamma_-' \xi_- Z_- \} \right] \\
&\approx i \sum_s \frac{\omega_{ps}^2}{2\omega^2} \frac{k_\perp}{k_\parallel} \frac{\omega}{\Omega_s} \left[ \Gamma_0'(\mu_s) \xi_{0s} Z(\xi_{0s}) - \sum_{n=1}^\infty \{ \Gamma_+' + \Gamma_-' \} \right] \\
&= i \sum_s \frac{\omega_{ps}^2}{2\omega^2} \frac{k_\perp}{k_\parallel} \frac{\omega}{\Omega_s} \left[ \Gamma_0'(\mu_s) \xi_{0s} Z(\xi_{0s}) - \sum_{n=1}^\infty \left\{ \Gamma_{n+1} - \Gamma_n + \frac{n}{\mu_s}\Gamma_n + \Gamma_{-n+1} - \Gamma_{-n} - \frac{n}{\mu_s}\Gamma_{-n} \right\} \right] \\
&= i \sum_s \frac{\omega_{ps}^2}{2\omega^2} \frac{k_\perp}{k_\parallel} \frac{\omega}{\Omega_s} \left[ \Gamma_0'(\mu_s) \xi_{0s} Z(\xi_{0s}) - \sum_{n=1}^\infty \{ \Gamma_{n+1} + \Gamma_{n-1} - 2\Gamma_n \} \right] \\
&= i \sum_s \frac{\omega_{ps}^2}{2\omega^2} \frac{k_\perp}{k_\parallel} \frac{\omega}{\Omega_s} \left[ \Gamma_0'(\mu_s) \xi_{0s} Z(\xi_{0s}) + \Gamma_0' \right].
\end{aligned}
\tag{2.65}
$$

---

[6] We assume that $\omega_{pi} \gg k_\perp c$ which is a statement that the perpendicular wavelength is larger than ion inertial length $d_i = \frac{c}{\omega_{pi}}$. Thus, we have $1 + \frac{1}{k_\parallel^2 \lambda_{De}^2} - \frac{\omega_{pi}^2}{\omega^2} \approx 0 \Rightarrow \omega^2 = \omega_{pi}^2 \frac{k_\parallel^2 \lambda_{De}^2}{1+k_\parallel^2 \lambda_{De}^2} \Rightarrow \frac{\omega^2}{k_\parallel^2} = \frac{T_e}{m_i}$

Finally, the last element $\epsilon_{xy}$ from Equation 2.47 is worked out below[7]:

$$\epsilon_{xy} = -i \sum_s \frac{\omega_{ps}^2}{\omega^2} \xi_{0s} \left[ \sum_{n=1}^\infty n\{\Gamma_+' Z_+ - \Gamma_-' Z_-\} \right]$$

$$= -i \sum_s \frac{\omega_{ps}^2}{\omega^2} \xi_{0s} \left[ \sum_{n=1}^\infty n\{\Gamma_{n+1} - \Gamma_n + \frac{n\Gamma_n}{\mu_s}\}(Z_+ - Z_-) \right]$$

$$= -i \sum_s \frac{2\omega_{ps}^2}{\omega^2} \xi_{0s} \frac{k_\parallel a_s}{\Omega_s} \sum_n \Gamma_n' \tag{2.66}$$

$$= i \sum_s \frac{\omega_{ps}^2}{\omega\Omega_s} \Gamma_0'(\mu_s). \tag{2.67}$$

Now that we are done working with each tensor component, we expand Equation 2.43 about the middle row. We neglect $\epsilon_{xz}$ and get the following expression

$$(\epsilon_{xx} - n_\parallel^2)(\epsilon_{zz} - n_\perp^2) - n_\perp^2 n_\parallel^2 = -\frac{\epsilon_{xy}^2(\epsilon_{zz} - n_\perp^2) + \epsilon_{yz}^2(\epsilon_{xx} - n_\parallel^2) + 2\epsilon_{xy}\epsilon_{yz}n_\parallel n_\perp}{(\epsilon_{yy} - n^2)}, \tag{2.68}$$

where we have assumed $\epsilon_{yy} - n^2 \neq 0$. This is to ensure that the frequency we consider is much less than the fast mode frequency[8]. The index of refraction $n = \frac{kc}{\omega} > \frac{k_\perp c}{\omega} = \frac{k_\perp c_A}{\Omega_i} \frac{c}{c_A} \frac{\Omega_i}{\omega}$. All three factors are $\gg 1$, therefore, $n^2 \gg \epsilon_{yy} \approx \mathcal{O}(\frac{c^2}{c_A^2})$. Therefore, we set the right hand side of Equation 2.68 to zero and get the dispersion relation of kinetic Alfvén wave. It was pointed out earlier that $\epsilon_{xx}$ component gives shear Alfvén wave dispersion relation and $\epsilon_{zz}$ component gives ion acoustic wave dispersion relation. Hence, kinetic Alfvén wave is a mixture of shear Alfvén and ion acoustic mode [Hasegawa and Chen, 1975]. The dispersion relation takes a simple form of

$$\left(\frac{\omega}{k_\parallel c_A}\right)^2 = \frac{\mu_i}{1 - \Gamma_0(\mu_i)} + \frac{k_\perp^2 \rho_s^2}{\Gamma_0(\mu_e)[1 + \xi_{0e} Z(\xi_{0e})]}. \tag{2.69}$$

So far we have approximated $|\xi_{ns} \gg 1|$ for $n \neq 0$ but have not made any assumption about $\xi_{0s}$. The cold electron approximation is given by $\xi_{0s} \gg 1$, whereas the hot

---

[7] Here we have used $\sum_{n=1} \Gamma_n = (1 - \Gamma_0)/2 \Rightarrow \sum_{n=1} \Gamma_n' = -\Gamma_0'/2$.

[8] For low beta ($\beta \ll 1$), fast mode frequency $\omega \sim kc_A$ for highly oblique propagation ($k_\perp \sim k$). This condition is satisfied if $\frac{k_\perp c_A}{\Omega_i} \gg 1$.

electron approximation is $\xi_{0s} \ll 1$. Using the hot electron approximation, the plasma dispersion function is

$$Z(\xi_{0e}) = i\sqrt{\pi}e^{-\xi_{0e}^2} - 2\xi_{0e} + \frac{4}{3}\xi_{0e}^3 - \text{.......} \tag{2.70}$$

$$\xi_{0e}Z(\xi_{0e}) = i\sqrt{\pi}\xi_{0e}e^{-\xi_{0e}^2} - 2\xi_{0e}^2 + \frac{4}{3}\xi_{0e}^4 - \text{.......}/. \tag{2.71}$$

The highest order term of Equation 2.71 is $i\sqrt{\pi}\xi_{0e}$ when the maximum value of $e^{-\xi_{0e}^2}$ is one. For small ion gyroradius, $\Gamma_0(\mu_i) \approx 1 - \mu_i + \frac{3}{4}\mu_i^2$ and similarly for the electrons[9], $\Gamma_0(\mu_e) \approx 1$. And we have

$$\frac{\mu_i}{1 - \Gamma_0(\mu_i)} \approx 1 + \frac{3}{4}\mu_i. \tag{2.72}$$

Letting $\mathscr{A} = 1 + \frac{3}{4}\mu_i$, Equation 2.69 is written as

$$\xi_{0e}^2 \frac{a_e^2}{c_A^2} = \mathscr{A} + k_\perp^2\rho_s^2[1 + i\sqrt{\pi}\xi_{0e} - 2\xi_{0e}^2]^{-1}. \tag{2.73}$$

Using Taylor expansion and rearranging, Equation 2.73 becomes

$$\left(\frac{a_e^2}{c_A^2} - 2k_\perp^2\rho_s^2\right)\xi_{0e}^2 + i\sqrt{\pi}k_\perp^2\rho_s^2\xi_{0e} - \left(\mathscr{A} + k_\perp^2\rho_s^2\right) = 0, \tag{2.74}$$

which is a simple quadratic Equation with the solutions

$$\xi_{0e} = \frac{-i\sqrt{\pi}k_\perp^2\rho_s^2 \pm \sqrt{-\pi k_\perp^4\rho_s^4 + 4\left(\frac{a_e^2}{c_A^2} - 2k_\perp^2\rho_s^2\right)\left(\mathscr{A} + k_\perp^2\rho_s^2\right)}}{2\left(\frac{a_e^2}{c_A^2} - 2k_\perp^2\rho_s^2\right)}. \tag{2.75}$$

If $\omega$ is decomposed as $\omega = \omega_r + i\gamma$ then $\xi_{0e} = \frac{\omega_r}{k_\parallel a_e} + i\frac{\gamma}{k_\parallel a_e}$, where $|\gamma| < \omega_r$ is assumed. Separating the real and imaginary parts of Equation 2.75, we have

$$\omega_r = \frac{k_\parallel a_e\sqrt{-\pi k_\perp^4\rho_s^4 + 4\left(\frac{a_e^2}{c_A^2} - 2k_\perp^2\rho_s^2\right)\left(\mathscr{A} + k_\perp^2\rho_s^2\right)}}{2\left(\frac{a_e^2}{c_A^2} - 2k_\perp^2\rho_s^2\right)} \tag{2.76}$$

---

[9] We assume $\rho_e < \rho_i$, which is not very restrictive at all. For real mass ratio of electron and proton, $\rho_i \sim 40\sqrt{\frac{T_i}{T_e}}\rho_e$. Therefore, $\mu_e < \mu_i$.

and

$$\gamma = \frac{-\sqrt{\pi} k_\perp^2 \rho_s^2 k_\parallel a_e}{2\left(\frac{a_e^2}{c_A^2} - 2k_\perp^2 \rho_s^2\right)}. \tag{2.77}$$

We assume, $\frac{a_e^2}{c_A^2} \gg 2k_\perp^2 \rho_s^2$ that implies $k_\perp^2 d_i^2 \frac{m_e}{m_i} \ll 1$, which is not very restrictive again. Picking out the highest ordered terms in Equations 2.76 and 2.77, we get

$$\begin{aligned}
\omega_r &= \frac{\sqrt{4\frac{a_e^2}{c_A^2} k_\perp^2 \rho_s^2 + 3\mu_i \frac{a_e^2}{c_A^2}}}{2\frac{a_e^2}{c_A^2}} \\
&= \frac{k_\parallel c_A}{2}\sqrt{4k_\perp^2 \rho_s^2(1 + \frac{3}{4}\frac{\rho_i^2}{\rho_s^2})} \\
&= k_\parallel k_\perp c_A \rho_s \sqrt{1 + \frac{3}{4}\frac{T_i}{T_e}} \tag{2.78}
\end{aligned}$$

and

$$\gamma = -\frac{\sqrt{\pi} k_\parallel a_e}{2} k_\perp^2 \rho_s^2 \frac{c_A^2}{a_e^2}. \tag{2.79}$$

When $\frac{T_i}{T_e} < 1$, from Equation 2.78 and Equation 2.79 we have

$$\frac{\gamma}{\omega_r} = -\frac{1}{2}\sqrt{\frac{\pi}{2}} k_\perp d_e, \tag{2.80}$$

where $d_e = \frac{c}{\omega_{pe}}$ is the electron inertial length. Typically, $k_\perp d_e < 1$ and the damping factor is small in that case. But, we have considered highly oblique propagation. For hot electrons, the kinetic Alfvén wave damping rate increases with higher propagation angle. The damping rate derived here cannot be applied to the large $\beta$ regime. Even for a low $\beta$ plasma with high frequencies and different ion to electron temperature ratio, the damping rate derived here breaks down. To explore other parameter regimes, numerical linear Vlasov dispersion solvers are used in general.

## 2.7 Outline for the Remaining Chapters

This concludes the introductory background materials that are useful for the rest of the Chapters. In Chapter 3, concepts introduced in Chapter 2 are used and concepts from both Chapter 1 and 2 are heavily used in Chapter 4 and 5. Brief synopses of Chapter 3, Chapter 4 and Chapter 5 are given below.

- In Chapter 3, the super-Alfvénic propagation of energy away from an x-line is examined using kinetic particle-in-cell simulations of antiparallel symmetric magnetic reconnection. In the reconnection simulations, the KAW wave vector has a typical magnitude of and a direction of 85 - 89 degrees relative to the local magnetic field. We find that the damping of the reconnection KAW is consistent with linear Landau damping results from a numerical Vlasov dispersion solver, which allows us to generalize our damping predictions to the magnetotail and solar corona. For the magnetotail, the KAW from reconnection will not damp away before propagating the 20 - 30 Earth radii to the inner magnetosphere and may produce white light aurora. For the solar corona, on the other hand, these KAWs will completely damp before reaching the photosphere.

- In Chapter 4, we simulate reconnection conditions appropriate for the magnetosheath and solar wind, i.e., plasma beta (ratio of gas pressure to magnetic pressure) greater than 1 and low magnetic shear (strong guide field). Changing the simulation domain size, we find that the ion response varies greatly. For reconnecting regions with scales comparable to the ion inertial length, the ions do not respond to the reconnection dynamics leading to "electron-only" reconnection with very large quasi-steady reconnection rates. Note that in these simulations the ion Larmor radius is comparable to the ion inertial length. The transition to more traditional "ion-coupled" reconnection is gradual as the reconnection domain size increases, with the ions becoming frozen-in in the exhaust when the magnetic island width in the normal direction reaches many ion inertial lengths. During this transition, the quasi-steady reconnection rate decreases until the ions are fully coupled, ultimately reaching an asymptotic value. The scaling of the ion outflow velocity with exhaust width during this electron-only to ion-coupled transition is found to be consistent with a theoretical model of a newly reconnected field line. In order to have a fully frozen-in ion exhaust with ion flows comparable to the reconnection Alfvén speed, an exhaust width of at least several ion inertial lengths is needed. In turbulent systems with reconnection occurring between magnetic bubbles associated with fluctuations, using geometric arguments we estimate that fully ion-coupled reconnection requires magnetic bubble length scales of at least several tens of ion inertial lengths.

- In Chapter 5, we explore "electron-only" magnetic reconnection embedded inside turbulence in three dimensional configuration. In 2.5D simulations, it has been shown that the reconnection rate for fully ion-coupled magnetic reconnection is of the order $0.1c_A$, far below recent spacecraft observations of the electron-only reconnection. We perform force-free three dimensional particle-in-cell simulation of high beta plasma to find that magnetic reconnection in 3D is inherently faster than in traditional 2.5D PIC simulation with enhanced parallel electric field, thereby giving us some context and understanding of magnetic reconnection found in the turbulent magnetosheath.

## Chapter 3

## SUPER-ALFVÉNIC PROPAGATION AND DAMPING OF RECONNECTION ONSET SIGNATURES

Propagation and damping of the standing kinetic Alfvén wave (KAW) structure generated from magnetic reconnection are explored. The damping of the quadrupolar out-of-plane (Hall) magnetic field is consistent with the numerical damping rate computed from the full linear Vlasov dispersion solver. KAWs with $kd_s \sim 0.25$ can travel global magnetotail distances and have sufficient Poynting flux to create white light aurora.

## 3.1 Introduction

Magnetic reconnection plays an important role in plasmas by converting magnetic energy into plasma flows, plasma heating and energetic particles. The energy converted by magnetic reconnection propagates away from the x-line, which is the site where magnetic field lines break and reform. While much of the energy propagates away at MHD speeds, i.e., the magnetosonic or Alfvén speed, a significant amount of Poynting flux $\vec{S} = \frac{c}{4\pi}\vec{E} \times \vec{B}$ has been shown to propagate super-Alfvénically in the form of Kinetic Alfvén Waves (KAWs) associated with the quadrupolar out-of-plane (Hall) magnetic field generated during kinetic reconnection [Shay et al., 2011, Lapenta et al., 2013], where $\vec{E}$ is the electric field and $\vec{B}$ is the magnetic field.

These KAWs are one of the fastest propagating signals generated at the onset of reconnection. Understanding their properties may allow a much more accurate determination of the timing of reconnection onset in observations. As an example, the sudden onset of magnetospheric substorms may be caused by reconnection onset about $20 - 30$ Earth radii ($R_e$) downtail [Baker et al., 1996] or a near Earth instability

around $10\,\mathrm{R}_e$ [Lui, 1996]. Determining whether reconnection and/or another instability is initiating substorms requires a careful timing analysis and has been the subject of much scrutiny [Angelopoulos et al., 2008, Lui, 2009, Angelopoulos et al., 2009, Kepko et al., 2009, Nishimura et al., 2010]. KAWs have been postulated as an energy source for aurora [Lysak and Song, 2004], and have been observed near reconnection sites in the magnetotail [Dai, 2009, Keiling et al., 2003] and during dayside reconnection [Chaston et al., 2005, 2009, Gershman et al., 2017].

An important unresolved question is how far these KAWs can propagate before they damp, disperse, or transform into some other wave mode; it is an open question whether these waves generated in the magnetotail make it $20 - 30\,\mathrm{R}_e$ to Earth and generate aurora. A linear analysis of the damping of KAWs in the inner magnetosphere found that most KAWs would be expected to propagate with little damping from $10\,\mathrm{R}_e$ to the ionosphere [Lysak and Lotko, 1996]. Mode conversion of compressional waves to KAWs in the strong density gradients of this region can create large parallel electric fields [Lysak and Song, 2011]. The morphology of these waves in the inner magnetosphere and auroral zone has been examined with kinetic models, finding both ion (e.g., [Chaston et al., 2004]) and electron (e.g., [Watt and Rankin, 2009, 2010, Damiano et al., 2015, 2016]) energization, either of which may cause aurora. However, the question remains if reconnection generated KAWs in the more distant magnetotail can successfully transmit significant Poynting flux from a magnetotail x-line to the inner magnetosphere.

KAWs in the more distant magnetotail plasma sheet have been modeled using MHD simulations and linear theory (e.g., [Lysak and Song, 2004, Lysak et al., 2009]). To date, however, a direct fully kinetic study examining both the generation and attenuation of these reconnection generated KAW has not yet been performed. A first step in this direction is to examine the KAW morphology in the region where the equilibrium geometry can be approximated as a quasi-1D current sheet; this examination is the focus of the current Chapter. The answer to this question can determine if significant reconnection-generated KAW energy can propagate large distances to regions

such as the inner magnetosphere, where more complicated global geometry effects due to the Earth's dipole field become important.

To directly examine the damping of KAWs during reconnection, we perform kinetic particle-in-cell (PIC) simulations of antiparallel symmetric reconnection in a 1D current sheet equilibrium and examine how the structure and amplitude of the Hall field changes as it propagates away from the x-line. After being generated, the peak amplitude of the standing KAW structure in the out-of-plane field decreases as it propagates away from the x-line. In order to compare with linear Landau damping theory, we estimate the average $k$ for the structure and determine the angle $\theta$ between $\mathbf{k}$ and the magnetic field. The reconnection simulations typically have a wavevector $k\,d_s \sim 1$, where $d_s \equiv d_i\,c_s/c_M$ (e.g., [Rogers et al., 2001]) is the effective fluid Larmor radius, $d_i$ is the ion inertial length, $c_s$ is the sound speed, and $c_M$ is the magnetosonic speed. The angle $\theta$ varies between $85°$ and $89°$. We find that the damping of the reconnection KAW is consistent with linear Landau damping predictions from a numerical Vlasov dispersion solver [Gary, 1993].

We emphasize that the findings in this Chapter do not include more complicated geometry effects such as the increase in the magnetic field in the Earth's dipole geometry and at lower altitudes in the solar corona. Modifications to the reconnection generated KAWs due to these effects will be the focus of future studies. With those caveats in mind, we extrapolate the findings to the magnetotail and the solar corona.

Poynting flux from reconnection in the solar corona during solar flares has also been postulated as a mechanism to accelerate electrons and create hard x-rays [Fletcher and Hudson, 2008]. Although this previous work has shown that long wavelength Alfvén waves associated with reconnection can drive flows into the solar corona to produce hard x-rays, in our analysis we find that shorter wavelength KAWs associated with reconnection will damp long before they can reach distances comparable to the length of a flare loop; hence, significant energy reaching the photosphere is unlikely.

For the magnetotail, reconnection KAWs with $k\,d_s \sim 1$ ($d_s \approx 0.25d_i$) can propagate $20\,R_e$ while retaining at least 10% of their initial amplitude. On the other hand,

waves with $k\,d_s \gg 1$ are expected to damp completely. Hence it seems likely that a significant amount of Poynting flux from reconnection generated KAWs at a near-Earth neutral line may propagate to the inner magnetosphere. Using a simplistic order of magnitude estimate for the amplification of Poynting flux in converging magnetic fields, the predicted Poynting flux magnitude is sufficient to have the potential for generation of aurora.

## 3.2   Validation of Particle-In-Cell (PIC) Simulations

### Particle In Cell (PIC) Method

**(a)**

**(b)**
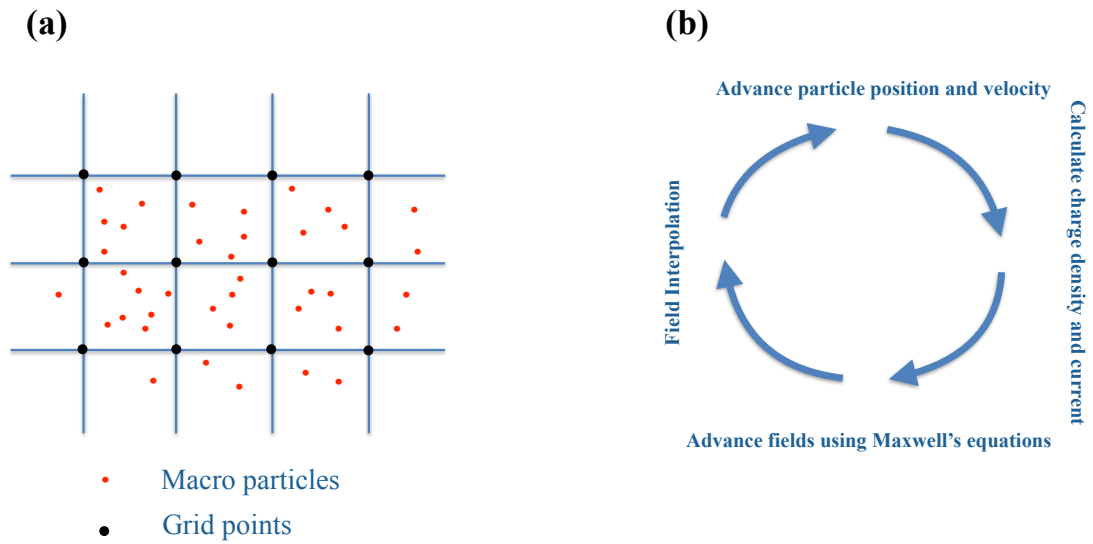


**Figure 3.1:** (a) Macro particles loaded within each grid cell are shown in red dots. (b) Evolution of fields and particles for a single time step $\Delta t$.

A very efficient way to solve the Vlasov equation is by using the particle in cell (PIC) method. A large number of "macro-particles" are populated with each grid

cell (hence the name Particle In Cell - PIC) as shown in Figure 3.1(a). The macro-particles satisfy the properties of plasma particles and are assigned with a specific distribution function. Individual macro-particle's trajectory is evolved using equations of motion. In essence, a randomly discretized distribution function (Monte Carlo method) is evolved in time. The moments of the distribution function like effective density, velocity, etc. at the grid points are calculated from the macro-particles. These moments are used to update the Maxwell's equations as shown in Figure 3.1(b). A complete description of PIC method is given in the book by Birdsall and Langdon [1985]. The numerical techniques for the PIC simulation (P3D) used in this thesis are documented in Zeiler et al. [2002].

We have also simulated a one dimensional single mode Alfvén wave to validate the PIC code used in this thesis. In this simulation, the mass ratio is $\frac{m_e}{m_i} = 0.01$, $\beta = 0.25$, $\frac{T_e}{T_i} = 1$ and the angle of propagation of the wave is 86º. The damping rate for this particular mode is $\frac{\gamma}{\Omega_i} = -0.015$. Unlike our prior coordinate system, the background magnetic field $\vec{B}_0$ lies in the $xz$-plane with wave vector $\vec{k}d_i$ pointing in the $x$-direction. The perturbations are initiated in the $y$ and $z$-directions. The eigenvectors from the two-fluid model is used for this validation. The frequency of the wave is $\omega/\Omega_i = 0.169$ with corresponding wave number $kd_i \sim 0.9234$. The time period of the wave is $\tau \sim 39\Omega_i^{-1}$. As is expected, the wave travels one complete cycle in this time period seen in Figure 3.2. We also plot the damped $B_y$ versus time shown in Figure 3.3. The rapid oscillations shown by the blue curve of $B_y$ are plasma wave oscillations. The overall damping of the wave is consistent with linear theory till $t = 10\Omega_i^{-1}$. However, for later times, significant deviation between the simulation and the linear theory is seen.

## 3.3 Simulation Parameters

In this Chapter, we also perform simulations of collisionless antiparallel reconnection in 2.5 dimensions using the parallel particle-in-cell code P3D [Zeiler et al.,
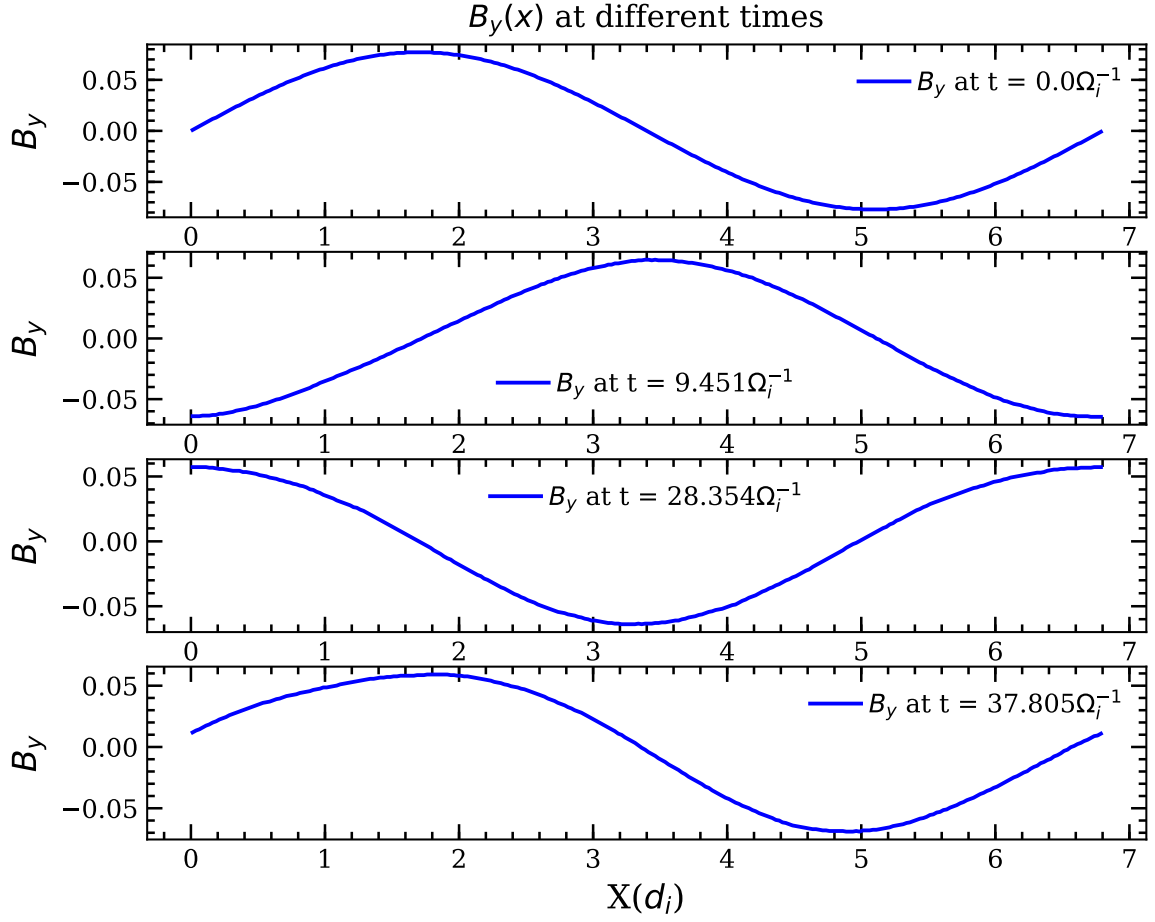
**Figure 3.2:** Evolution of $B_y$ as it propagates to the right in the $x$-direction.

| | Simulation parameters | | | | | | | | | | KAW scaling | | |
|---|---|---|---|---|---|---|---|---|---|---|---|---|---|
| Runs | $\frac{m_e}{m_i}$ | $B_{\text{up}}$ | $n_{\text{up}}$ | $T_{\text{e}}$ | $T_{\text{i}}$ | $\beta$ | $c/c_{\text{A}}$ | $\frac{L_{\text{x}}}{d_i}$ | $\frac{L_{\text{y}}}{d_i}$ | $\frac{\Delta}{d_i}$ | $\theta$ | $kd_{i\ell}$ | $kd_{s\ell}$ |
| A | 0.01 | 0.3 | 0.18 | 0.35 | 1.2 | 6.23 | 30 | 204.8 | 102.4 | 0.025 | 89 | 3.88 | 3.38 |
| B | 0.04 | 1 | 0.04 | 9 | 9 | 1.44 | 40 | 409.6 | 204.8 | 0.4 | 85 | 1.97 | 1.27 |
| C | 0.04 | 1 | 0.04 | 9 | 9 | 1.44 | 40 | 1638.4 | 204.8 | 0.4 | 85 | 1.5 | 1.0 |
| D | 0.04 | 1 | 0.2 | 0.083 | 0.25 | 0.13 | 15 | 204.8 | 102.4 | 0.05 | 85 | 3.83 | 1.0 |

**Table 3.1:** Plasma parameters of four simulations : $\Delta$ is grid scale, $c/c_A$ is light speed, and $(L_{\text{x}}, L_{\text{y}})$ are simulation domain sizes. $d_s = d_i c_s / c_M$ is the effective fluid Larmor radius as described in the text. The subscript "$\ell$" denotes the lobe (local) values of parameters used where the KAWs are identified.
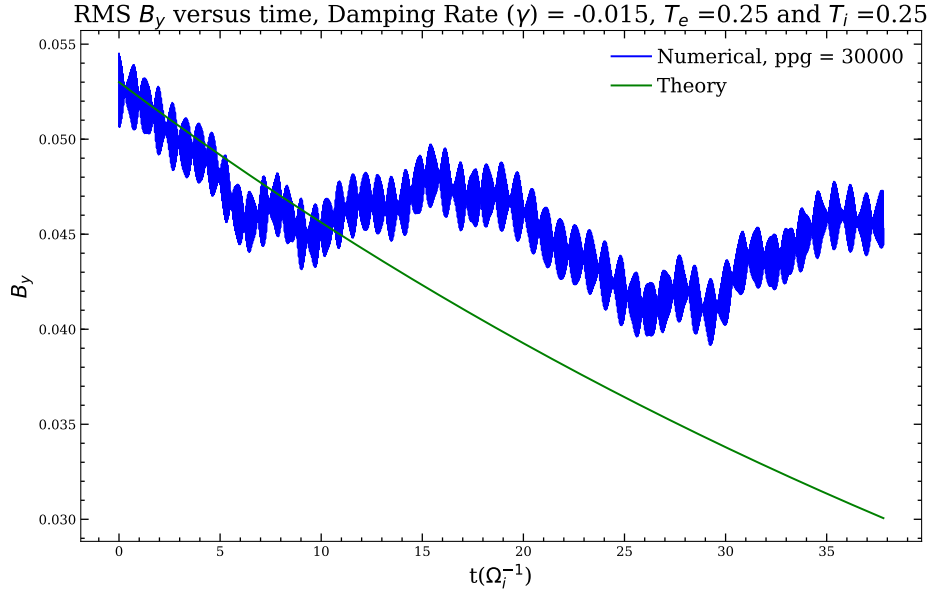
**Figure 3.3:** Root mean square (RMS) of $B_y$ is plotted in time. The blue curve is measured from the simulation and the green line is the damping rate calculated from the Vlasov dispersion solver. 30000 particles per cell is used in this simulation.
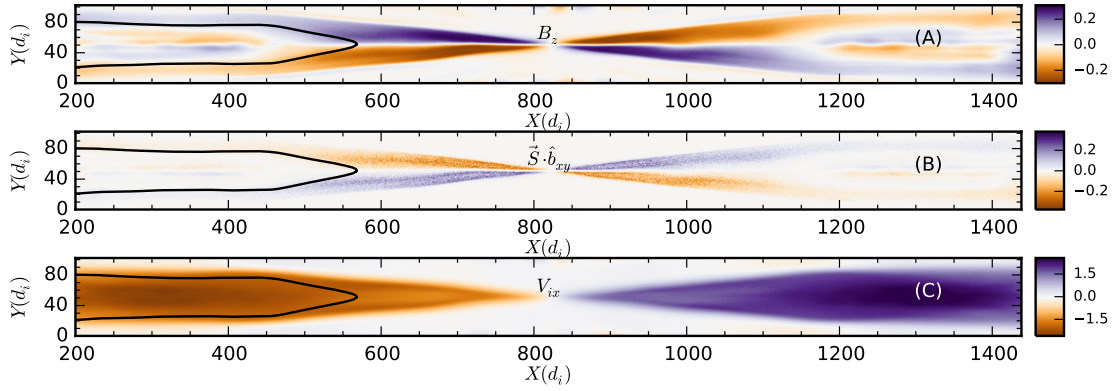


**Figure 3.4:** Sim C: At time $t = 175\Omega_i^{-1}$: (A) Out of plane magnetic field $B_z$, (B) parallel Poynting flux projection onto the $x-y$ plane, and (C) ion outflow velocity $V_{ix}$. The black contour in all three plots is the magnetic field line tracked to study the KAW propagation. The KAW structure in (A) and (B) broadens significantly and damps as it propagates downstream.

2002]. Calculations are presented in normalized units: the magnetic field to $B_0$, density to $n_0$, lengths to ion inertial length $d_i \equiv c/\omega_{pi}$, times to inverse ion cyclotron

63
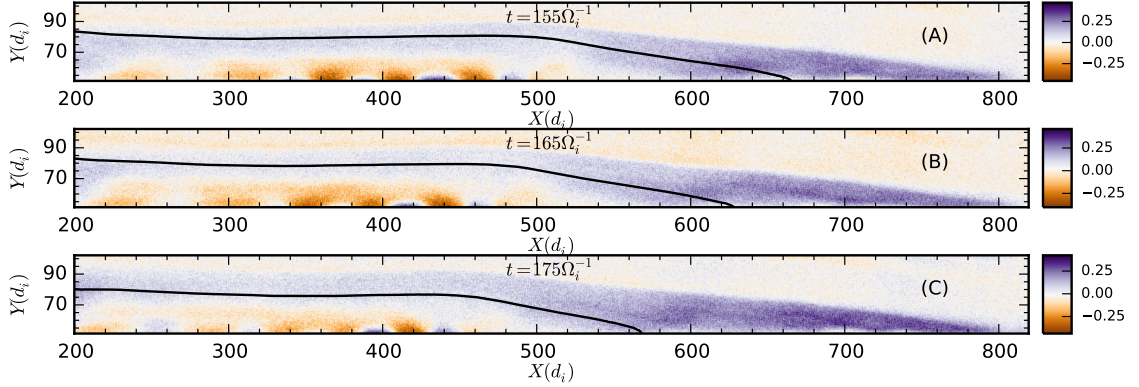
**Figure 3.5:** Sim C: Evolution in time of $B_z$ and a single magnetic field line (constant magnetic vector potential $\psi$).

frequency $\Omega_i^{-1}$ defined in terms of $\frac{m_i c}{e B_0}$, velocities to the Alfvén speed $c_{A0}$, temperature to $m_i c_{A0}^2$, and electric fields to $E_0 = B_0 c_{A0}/c$ and Poynting flux to $S_0 = \frac{c_A B_0^2}{4\pi}$. Using the simulation normalized units, various key physical length scales can be calculated from code values as: ion inertial length $d_i = \sqrt{1/n}$; electron inertial length $d_e = \sqrt{(m_e/m_i)\, n}$; ion Larmor radius $\rho_i = \sqrt{T_i}/B$; and electron Larmor radius $\rho_e = \sqrt{T_e\,(m_e/m_i)}/B$. The simulations have a periodic domain with size $L_x \times L_y$ and grid scale $\Delta$. The simulations are initialized with two Harris sheet currents[1]: $B_x = B_{up}\big(\tanh\left[(y - 0.25 L_y)/w_0\right] - \tanh\left[(y - 0.75 L_y)/w_0\right] + 1\big)$ is the equilibrium magnetic field, where $w_0$ is the half-width of the initial current sheets. The inflowing plasma has magnetic field $B_{up}$ and density $n_{up}$. A small local magnetic perturbation is added to start the reconnection.

We examine four different simulations, the parameters of which are given in Table 3.1. Note that the simulations use artificially large $m_e/m_i$, which is necessary because all electron length and time scales must be resolved in the simulations. The first simulation (sim A) is a high-$\beta$ simulation. The second (sim B) and third (sim C) have $\beta \sim 1$. Sim C is longer in the $x$-coordinate than the other simulations and allows a direct measurement versus time of the attenuation of the KAW. In the other,

---

[1] Harris sheet current is an exact one-dimensional solution to the kinetic Vlasov-Maxwell equilibrium equation. The magnetic field is a hyperbolic tangent function.
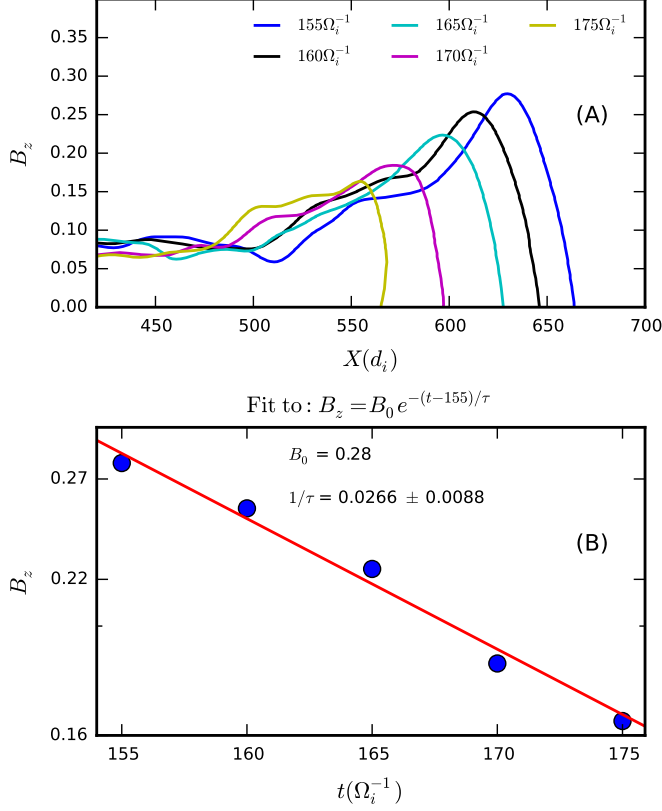
**Figure 3.6:** Sim C: (A) $B_z$ along the contours of constant $\psi$ in Figure 3.5 are plotted at $155\Omega_i^{-1}$, $160\Omega_i^{-1}$, $165\Omega_i^{-1}$, $170\Omega_i^{-1}$, and $175\Omega_i^{-1}$. (B) Peak value of $B_z$ from (A) with respect to time on a semilog scale. The dotted points are simulation data. The red line is the best fit line.

shorter simulations, an effective time based on the quasi-steady reconnection rate will be utilized. Lastly, the fourth (sim D) is a low-$\beta$ simulation.

KAWs in our simulations are identified from the analysis shown in Rogers et. al. [Rogers et al., 2001], where the key controlling length is $d_s \equiv d_i\, c_s/c_M$, and $d_s^2 \gg d_e^2$ is the necessary condition to have KAWs; $c_s$ is the sound speed and $c_M$ is the magnetosonic speed. Note that for $\beta \ll 1$ this length reduces to $d_s \approx \rho_s = c_s/\Omega_i$, where $\Omega_i$ is the ion cyclotron frequency. The angle of propagation and the values of $k$ for each simulation are given in Table 3.1

## 3.4 Propagation and Damping of KAW

We start by examining the propagation of the magnetic field line after it reconnects and travels downstream. As the magnetic field line reconnects and propagates away from the x-line, the magnitude of $B_z$ on the field line grows in time, reaches a peak value, and then begins to decrease in amplitude. For simplicity, we examine times after $B_z$ has reached its peak value.

First, we examine a very long simulation in which the propagation and damping of the KAW can be observed to occur in time, namely sim C. A snapshot of the simulation is shown in Figure 3.4 at $t = 175 \, \Omega_i^{-1}$. $B_z$ and the Poynting flux are enhanced in the exhaust, especially at the outer edges near the separatrices (Figure 3.4A and B). Examining $V_{ix}$ (Figure 3.4C) reveals significant ion flow that spans the entire domain of the simulation box. The enhanced Poynting flux and quadrupolar structure is due to the parallel electron flows near the separatrices that are super-Alfvénic [Shay et al., 2011]. The black contour line at the left side of the panels is the field line used to study the morphology of $B_z$. The evolution of this field line as it propagates away from the x-line is shown in Figure 3.5 on top of the value of $B_z$ in one quadrant of the reconnection region.

To examine the propagation and decay of the KAW along this magnetic field, we plot $B_z$ on the field line at different times in Figure 3.6A. The peak magnitude of $B_z$ steadily decreases in time, and this peak value is plotted versus time in a semilog plot in Figure 3.6B. The best fit line for an exponential decay is shown, with an exponential decay rate of $1/\tau = 0.0266 \pm 0.0088$.

We have also performed more modest sized simulations. In these simulations, the reconnection does not proceed long enough to follow a magnetic field as it propagates downstream in the manner of Figure 3.5. Therefore, for simulations A, B, and D, we use the same analysis methods used in Shay et al., 2011 [Shay et al., 2011]. During the quasi-steady phase of the reconnection simulation, the structure of the KAW in the vicinity of the x-line does not change significantly. The motion of the magnetic field lines in this quasi-steady region can be directly linked to the change in magnetic
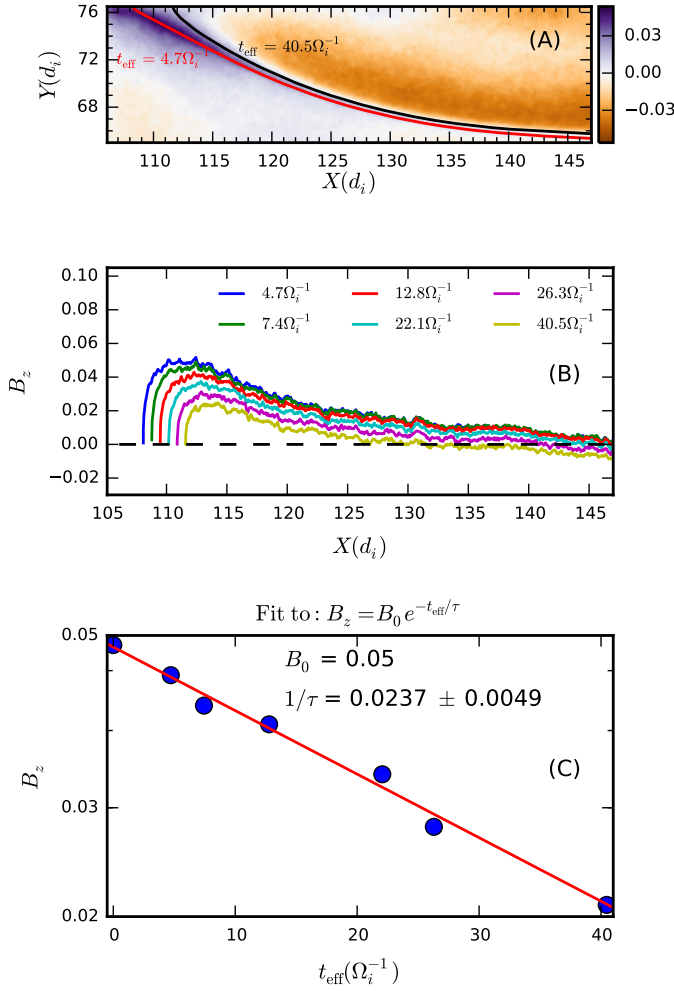
**Figure 3.7:** Sim A: (A) lower right quadrant of $B_z$ structure with two magnetic field lines shown as red and black lines with corresponding effective time. (B) $B_z$ along field lines shown in (A). (C) Peak value of $B_z$ for each field line in (B) with respect to effective time $t_{\mathrm{eff}}$ in semilog scale. The quasi-steady reconnection is used to determine $t_{\mathrm{eff}}$, as described in the main body. Best fit line shown in red.

vector potential: $\Delta t = \Delta \psi / E$, where $E$ is the spatially uniform reconnection electric field along the $z$ direction. The effective time difference between magnetic field lines in the exhaust is determined by setting $t = 0$ at the x-line, giving $t_{\mathrm{eff}} = (\psi - \psi_{\mathrm{xline}})/E$. In this way, the motion of the magnetic field and the damping of the KAW wave can be studied by examining how $B_z$ changes with changing $\psi$. An example of this method is
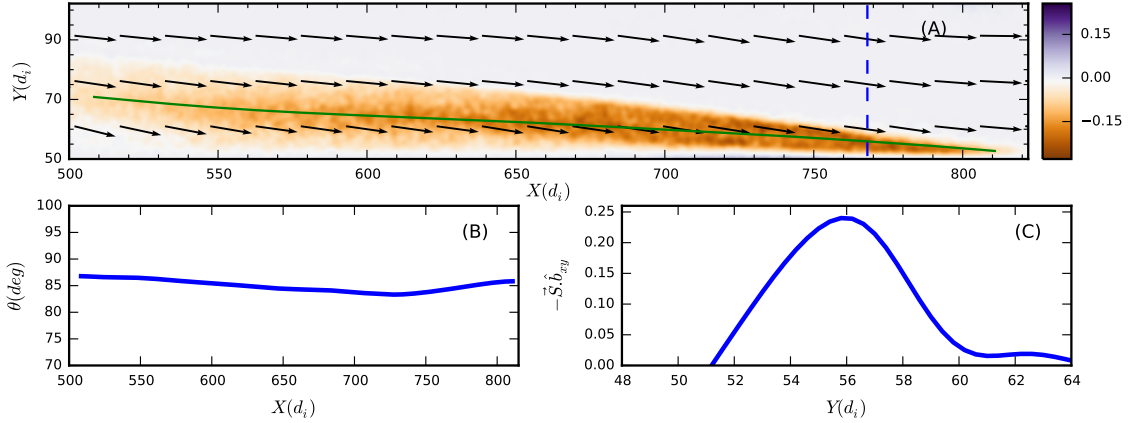
**Figure 3.8:** Sim C: Determination of KAW angle of propagation at $t = 175\,\Omega_i^{-1}$. **(A)** $\vec{S} \cdot \hat{b}_{\mathrm{xy}}$ in top left reconnection quadrant with vectors giving the magnetic field direction. The green line shows the location of the peak value of the $\vec{S} \cdot \hat{b}_{\mathrm{xy}}$ at each $x$ value. The wave vector $(\vec{k})$ is perpendicular to this line. The magnetic field is nearly parallel to the green line, giving a wave vector $\vec{k}$ that is oblique to the magnetic field. This gives the angle of propagation $\theta$ of the KAW that is shown in panel B. **(B)** $\theta$ variation with $x$ along the green line in (A). **(C)** $-\vec{S} \cdot \hat{b}_{\mathrm{xy}}$ is plotted along the dashed blue line shown in panel (A) at $x = 768$. The half max width is $5.2\,d_{\mathrm{i}}$ giving $k\,d_{s\ell} \approx 1.0$ where $d_{s\ell}$ is based on the local density.

shown in Figure 3.7 for Simulation A. The two red and black lines in (A) plotted over the color plot of $B_{\mathrm{z}}$ show the field lines used in this analysis. Note that we only show the first and the last field line and field lines in between are not shown in (A). The peak value of $B_{\mathrm{z}}$ on these field lines gradually decreases as the field line propagates away from the x-line, as shown in Figure 3.7B. The change in this peak value with $t_{\mathrm{eff}}$ is shown in (C) with a best fit line on a semilog plot. The best fit exponential decay rate is $1/\tau = 0.0237 \pm 0.0049$. Similar analyses were performed for Simulations B and D, yielding $1/\tau = 0.0520 \pm 0.018$ and $1/\tau = 0.0421 \pm 0.0121$ respectively.

An important question is whether the empirically measured damping rates are consistent with theoretical prediction based on linear Landau resonance. To examine this question, we compared the measured rates to theoretical predictions based on the
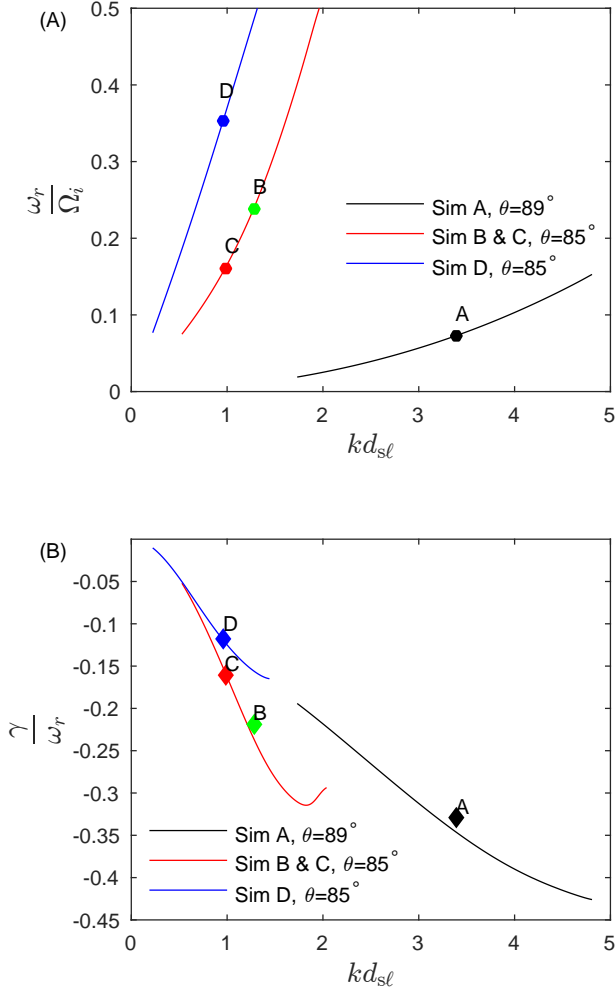
**Figure 3.9:** Comparison between Vlasov dispersion predictions and reconnection simulation measurements. The lines show frequencies versus $k\,d_{s\ell}$ from the Vlasov solver. (A) Real frequencies $\omega_{\rm r}/\Omega_{\rm i}$. The colored circles show the Vlasov solver real frequency at the appropriate $k\,d_{s\ell}$ for each simulation. (B) Damping rates $\gamma/\omega_{\rm r}$. The diamonds are measured damping rates for the reconnection simulations at the measured $k\,d_{s\ell}$ value.

well-known linear Vlasov dispersion solver [Gary, 1993] which solves the fully electromagnetic plasma dispersion relation using Newton's method. We have compared results of this linear Vlasov solver to the Lysak and Lotko dispersion relation [Lysak and Lotko, 1996]; the two show agreement in regimes where the Lysak and Lotko relation is valid (particularly $\beta \ll 1$). The angle of propagation $\theta$ relative to the magnetic
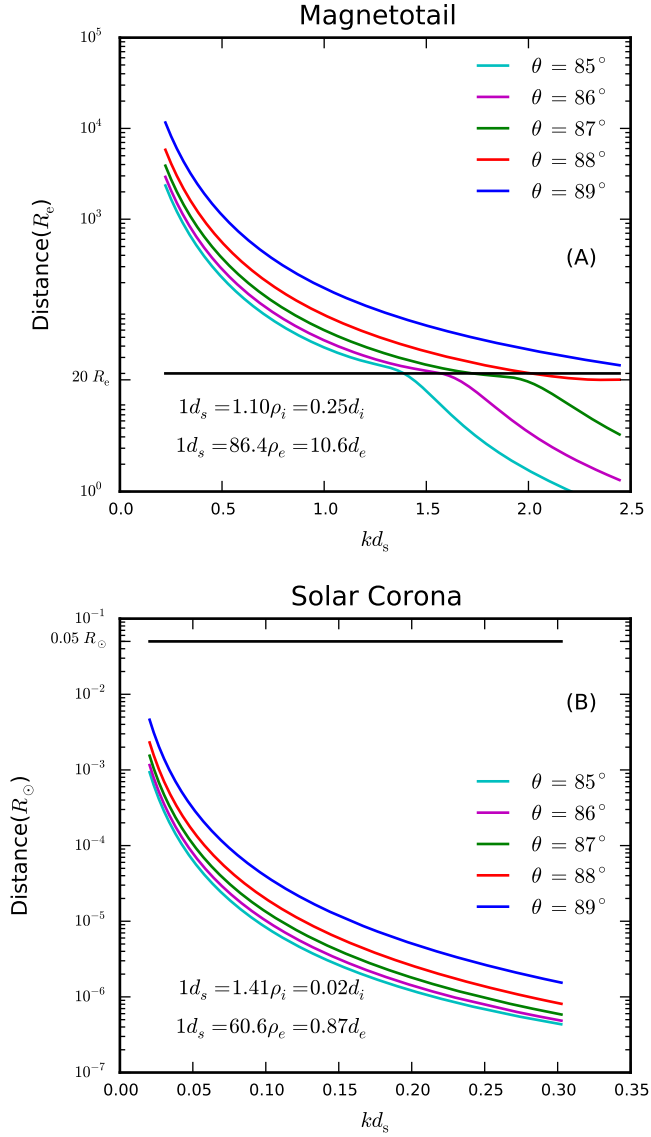
**Figure 3.10:** Distance traveled by reconnection KAW before it attenuates to 10% of its initial $B_z$ amplitude for several oblique propagation angles $\theta$. The conversion between the fluid Larmor radius $d_s$, ion Larmor radius $\rho_i$, and ion inertial length $d_i$ is given in each panel. Note that this extrapolation assumes constant background plasma and field conditions. (A) Magnetotail parameters: KAWs with $k\,d_s \lesssim 1$ can propagate global magnetotail distances of $20\,R_e$ (shown by black line). (B) Solar corona parameters: All KAWs damp before reaching about $10^{-3} R_\odot$, which is about one order of magnitude smaller than a typical flare loop length.

field is needed to determine the theoretical damping rate. To measure $\theta$ we examined the quasi-1D spatial structure of $\vec{S} \cdot \hat{b}_{xy}$ shown at $t = 175\,\Omega_i^{-1}$ in Figure 3.8A, where $\vec{S} = \frac{c}{4\pi}\vec{E} \times \vec{B}$ and $\hat{b}_{xy} = (\vec{B}_x + \vec{B}_y)/\sqrt{B_x^2 + B_y^2}$. The green line represents a line of peak value of $\vec{S} \cdot \hat{b}_{xy}$ for the KAW with $\vec{k}$ perpendicular to this line. Clearly the wave propagation is oblique with $\vec{k}$ nearly perpendicular to the magnetic field. $\theta$ is relatively constant for the KAW as shown in Figure 3.8B, where $\theta$ is given versus $x$ along the green line in (A). We used the average value in (B) of $\theta \approx 85°$ for the linear dispersion solver. In Figure 3.8C, we determined the magnitude of $\vec{k}$ by examining $-\vec{S} \cdot \hat{b}_{xy}$ as a function of distance along the dashed blue line shown in Figure 3.8A. The half max width is 5.2 giving an approximate wavelength of $\lambda \approx 20.8$ and $k\,d_{s\ell} \approx 1.0$ where $d_{s\ell} = d_{i\ell}c_s/c_m$ is the effective fluid Larmor radius using local values. Note that the local value of the parameters in the vicinity of the KAW that are used for the linear dispersion solver are denoted by the suffix $\ell$. These local values are approximately equal to the inflowing plasma conditions. For each simulation, $\theta$, $k\,d_{s\ell}$ and $k\,d_{i\ell}$ are given in Table 3.1.

The estimates of $\theta$ and $k$ above completes all the parameters required to get the wave frequency and the damping rate, which are $B$, $\theta$, $k$, $T_e$, $T_i$, and $n$. We use the Vlasov dispersion solver by Gary [1993] to calculate the frequencies and the damping rates of the KAWs generated in our simulation; note that for each comparison the Vlasov solver uses the same artificial mass ratio as was used in the kinetic PIC simulation.

The comparison between the reconnection findings and Vlasov predictions are shown in Figure 3.9. The solid lines in the two panels are the linear frequencies from the Vlasov solver using the simulation parameters as inputs. In Figure 3.9A, the colored circles give the Vlasov real frequencies for the $kd_{i\ell}$ measured in the reconnection simulations. In Figure 3.9B, the diamonds denote the damping rates measured directly from the reconnection simulations. Highlighting simulation C, the point $(kd_{s\ell}, \frac{\omega_r}{\Omega_i}) = (1.0, 0.1604)$ is the red circle in Figure 3.9A and the red diamond in Figure 3.9B is $\frac{\gamma}{\Omega_i} = -0.0266$. The linear Vlasov damping calculations in Figure 3.9B

match the reconnection simulations quite well, even though the simulations do not have a homogeneous background and isotropic temperatures as is assumed in the linear Vlasov dispersion solver. The good agreement between the PIC simulations and linear theory allows us to extrapolate the simulation output to realistic parameters in the magnetotail and solar corona in the next section.

One question is whether this damping is due to electron or ion resonance. For simulation D, the parallel KAW speed is a factor of two larger than the electron thermal velocity and more than a factor of four larger than the ion thermal velocity. In simulations A, B, and C, the parallel KAW phase speed lies between the electron and ion thermal velocities and within around a factor of two of both of them. However, in this case a parameter sweep using the linear Vlasov solver shows that changing $T_e$ modifies the damping rate substantially. For these reasons, it seems plausible that the damping is due to the electrons.

## 3.5   Extrapolation to Magnetotail and Solar Corona Parameters

Ultimately, we wish to determine the fate of the Poynting flux associated with the reconnection KAWs. In the magnetotail, can these KAWs propagate $20 - 30\,\mathrm{R}_e$ from the reconnection site to the ionosphere to drive the aurora? Similarly, in the solar corona, could KAWs propagate along a flare loop to the photosphere and create hard x-rays? Using plasma parameters in these two systems, we extrapolate the Landau damping findings to determine the distance traveled before the wave is reduced to 10% of its initial amplitude. Note, however, that the direct applicability of these extrapolations is limited to regions where the equilibrium current structure generating reconnection can be approximated as a quasi-1D current sheet. Effects such as changing magnetic field strength and plasma parameters due to the Earth's dipole field are not included. However, even with these limitations, the predictions give KAW amplitudes and Poynting flux that are testable by in-situ satellite observations.

Magnetotail parameters used are: $B = 20\,\mathrm{nT}$, $n = 0.1\,\mathrm{cm}^{-3}$, $T_i = 1\,\mathrm{keV}$, $T_e = 300\,\mathrm{eV}$, which are typical conditions found in this region. The ion inertial length $d_i$

and KAW wavelength using these parameters are $721\,\text{km}$ and $1180\,\text{km}$ respectively, which are much smaller compared to the magnetotail scale lengths $20 - 30\,R_{\text{e}}$. Using the parallel wave speed and the damping frequency from the linear Vlasov calculation, we calculated how far a KAW will travel before attenuating to 10% of its initial amplitude. For different oblique propagation angles, we plot this distance versus $k\,d_s$ in Figure 3.10A. Reference lines are drawn for parallel propagation distances of $20R_{\text{e}}$, which would be sufficient for the KAW to propagate global magnetotail distances. While KAW with $k\,d_s \sim 0.25 \rightarrow k\,d_i \sim 1$ will easily propagate these global distances, KAW with $k\,d_s \gg 0.25$ would be expected to damp away well before that point.

We also estimate the change in Poynting flux strength as the KAWs propagate away from the X-line using $S \approx S_x \approx B_z B_z' C_{Az} d_i / 4\pi$ from Shay et al. [2011], where $B_z' = \partial B_z / \partial y \approx k\,B_z$. Using $B_z / B_{\text{up}} \approx 0.3$ and the parallel wave speed, Figure 3.11 shows the Poynting flux versus distance from the x-line for selected wave numbers and propagation angles. Higher $k$ values as expected begin with higher Poynting flux, but show increased damping with distance. On the other hand, $k\,d_s \sim 0.25$ shows almost no damping. The angle of propagation has a large effect for higher wave numbers.

Using the rough approximation by Shay et al. [2011] that the Poynting flux stays on the same magnetic flux tube and ignoring mode conversion and reflection, we estimate the Poynting flux in the ionosphere as $S_{\text{ion}} \sim (B_{\text{ion}}/B_{\text{lobe}})S_{\text{lobe}} \sim 10^3 S_{\text{lobe}}$. The minimum Poynting flux capable of creating white light aurora is estimated as $10^{-3}\,\text{W/m}^2$, giving a white-light threshold of $10^{-6}\,\text{W/m}^2$ for Figure 3.11, which is drawn as a horizontal dotted line. We emphasize that this threshold is uncertain and should be viewed only as an order of magnitude estimate, as it does not include wave conversion and other effects associated with changing plasma conditions. Thus, for the angles presented, $k\,d_s \sim 0.25$ equivalent to $k\,d_i \sim 1$ have the potential to create white light aurora, but $k\,d_s \gg 0.25$ are not expected to.

For the solar corona, we also estimate the distance a reconnection KAW could travel before $B_z$ damps to 10% its original amplitude. Parameters used are: $B = 0.05\,\text{T}$, $T_{\text{i}} = 10^7\,\text{K}$, $T_{\text{e}} = 10^7\,\text{K}$, $n = 3.0 \times 10^9\,\text{cm}^{-3}$. Propagation distances are shown
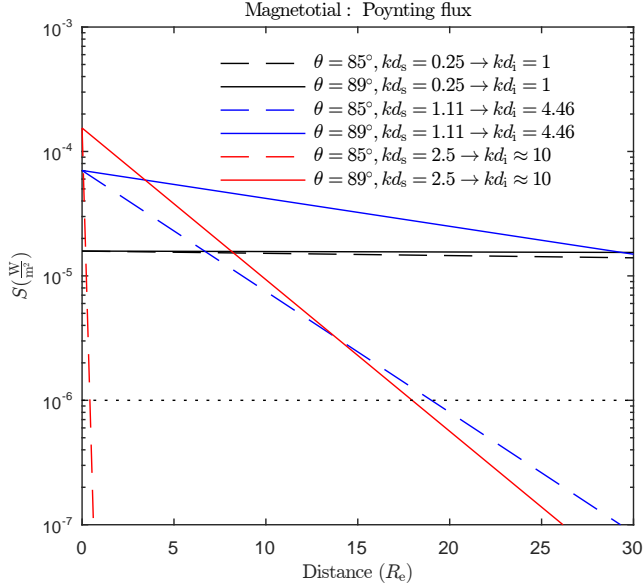
**Figure 3.11:** Strength of KAW Poynting flux $S_x$ at different $R_e$ distances from the reconnection x-line. Angles of propagation of 85° and 89° are chosen for three distinct $kd_s$. Note that this extrapolation assumes constant background plasma and field conditions. The dotted line at $10^{-6}$ W/m² is a simplistic order of magnitude estimate of the threshold $S$ which has the potential to create white light aurora, as described in the body of the text.

in Figure 3.10B. A typical flare loop has length $30 - 100\,\mathrm{M}m$ which is $0.05 - 0.15\,R_\odot$. All KAW with $k\,d_s \sim 0.02 \to k\,d_i \sim 1$ damp to 10% after propagating at most one order of magnitude less than a flare loop length. The reconnection KAW would not be expected to reach the photosphere and generate hard x-rays. Once again, we reiterate that these approximate should be viewed as an upper bound.

## 3.6  Conclusions

Using kinetic PIC simulations, we examine the attenuation of the Hall quadrupolar magnetic field structure during symmetric reconnection, which propagates as a kinetic Alfvén wave. This attenuation is consistent with predictions from linear Landau damping theory. Extrapolating to magnetotail parameters and using a realistic mass ratio, KAWs with $k\,d_s \sim 0.25$ can propagate the global magnetotail distances (on the

order of 20 $R_e$) without complete attenuation; therefore, these KAWs have the potential to create white light aurora.

There is a question of the validity of applying a simplistic 1D wave analysis to the standing KAW structure associated with magnetic reconnection. Effects such as perpendicular wave propagation and/or wave dispersion could lead to an inaccurate estimation of the damping of the wave. Regarding perpendicular propagation, the inflow edge of the KAW boundary near the separatrices in Figure 3.4 remains quite sharp for large distances downstream of the x-line; perpendicular spreading of the wave would be expected to blur this boundary. This lack of spreading is likely associated with the plasma inflowing velocity, which roughly balances the perpendicular propagation of the wave. Regarding wave dispersion, if dispersion were broadening the KAW, a traveling wave train associated [Coroniti, 1971] with dispersion would exist upstream of the separatrices. The key point, however, is that the linear Landau damping predictions match quite well with the 2D nonlinear reconnection simulations. The applicability of linear damping to this systems appears quite robust, considering that this study uses both quasi-steady and time varying analysis of the magnetic field lines, and also spans a range of plasma parameters and ion to electron mass ratios.

There are significant complications, however, which must be addressed in future studies before explicit predictions can be made about the role of these KAW in generating aurora and hard x-rays. As the waves approach the inner magnetosphere, the increasing magnetic strength is expected to enhance $k_\perp$, which likely would increase the damping. On the other hand, the amplitude of the wave can change due to mode conversion and reflection. This could, in fact, dominate over the effects of linear decay of the wave and thus may limit the scope of our predictions to a smaller tail region where most of the plasma background is uniform. Hence, the KAW propagation in the inner magnetosphere and auroral region will be the topic of future study. It is clear, however, that electron scale KAWs with $k\,d_s \gg 0.25$ will attenuate completely before reaching the inner magnetosphere. For the solar corona, on the other hand, all KAWs with $k\,d_s \gtrsim 0.02$ will damp long before reaching the photosphere.

## Chapter 4

## TRANSITION FROM ION-COUPLED TO ELECTRON-ONLY RECONNECTION: BASIC PHYSICS AND IMPLICATIONS FOR PLASMA TURBULENCE

This Chapter studies magnetic reconnection in the magnetosheath unlike the magnetotail in Chapter 3. Multiple PIC simulations were performed and the coupling of ions to magnetic reconnection were studied systematically. The scaling of reconnection ion exhaust velocity is consistent with standing kinetic Alfvén wave dynamics calculated from the linear Vlasov dispersion solver. The smallest discernible ion flows require reconnection exhaust width of at least 5 $c/\omega_{pi}$, while fully ion coupled reconnection are several 10's of $d_i$.

### 4.1  Introduction

Magnetic reconnection is a magnetic energy release process that plays a fundamentally important role in laboratory, space, and astrophysical plasmas [Yamada et al., 2010]. The role that magnetic reconnection plays in damping turbulent fluctuations in plasma has significant implications for our understanding of diverse systems such as the solar corona, the solar wind, the Earth's magnetosheath, and astrophysical accretion disks. While magnetic reconnection has been observed in the Earth's turbulent magnetosheath [Retinò et al., 2007, Yordanova et al., 2016, Eriksson et al., 2016, Vörös et al., 2017, Phan et al., 2018], our understanding of its role in damping turbulent magnetic energy and heating the plasma is incomplete. Two-dimensional magnetohydrodynamics (MHD) simulations and Hall MHD simulations of turbulence have been used to study the statistics of reconnection, finding a wide range of reconnection rates at x-lines occurring as part of the turbulence [Servidio et al., 2010,

76

Donato et al., 2012]. The x-lines showing robust reconnection had reconnection rates consistent with quasi-steady theories of reconnection [Cassak and Shay, 2007]. Recently, these x-line identification techniques were applied to fully kinetic simulations of turbulence [Haggerty et al., 2017], where a similar spread of reconnection rates was found. The effect of reconnection on the cascade of energy and even as a driver of the cascade has recently been the focus of significant study [Cerri and Califano, 2017, Dong et al., 2018, Mallet et al., 2017, Boldyrev and Loureiro, 2017, Franci et al., 2017, Papini et al., 2018]. A framework for estimating the heating due to reconnection in turbulence has been established [Shay et al., 2018], which draws on recent studies of heating during isolated laminar reconnection [Phan et al., 2013, 2014, Shay et al., 2014, Haggerty et al., 2015].

In a low collisionality plasma, the cascade of turbulent energy from large energy containing scales to small scales raises the question as to the existence and properties of the magnetic reconnection at the smallest scales where turbulent energy is damped. At such small scales, it seems likely that reconnection may occur in regions so small where the ions do not respond: i.e., "electron-only reconnection" occurs. In fact, recent observations of magnetic reconnection in the turbulent magnetosheath have observed magnetic reconnection occurring with no ion response [Phan et al., 2018].

Various aspects of electron-only reconnection have been studied previously with both fluid and kinetic particle-in-cell (PIC) simulations (e.g., Shay et al. [1998], Chacón et al. [2007], Jain et al. [2012], and references therein). Simulation scaling studies [Biskamp et al., 1995, Shay et al., 1998] found that the rate of quasi-steady reconnection is independent of the electron mass. The decoupling of electron and ion velocities, e.g., Hall physics [Sonnerup, 1979, Terasawa, 1983], was found to be a key factor in this independence. Studies of the transition from this Hall reconnection to more typical "ion-coupled reconnection" have also been performed and show that the timescale to reconnect flux transitions from a Hall timescale to one mediated by the MHD Alfvén time [Mandt et al., 1994, Biskamp et al., 1995]; note that we use the term "ion-coupled" to describe reconnection in which the ion outflow exhausts become
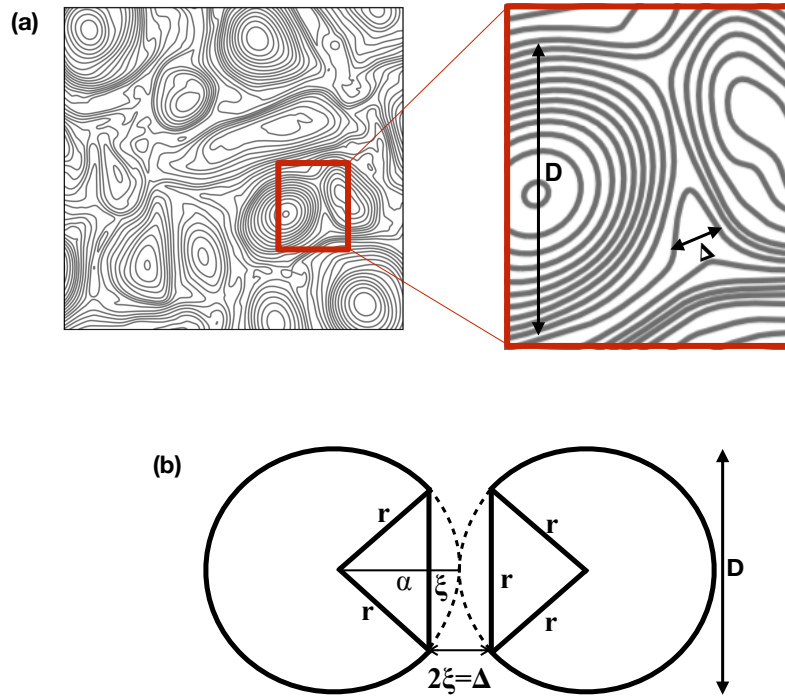
**Figure 4.1:** (a) Schematic of magnetic field lines adapted from Phan et al. [2018] showing an enlargement in the vicinity of a magnetic reconnection region. Shown are the approximate exhaust width $\Delta$ from the reconnection of a magnetic bubble roughly of size D. (b) Geometrical interpretation: two flux bubbles with radius r with a separation distance $\Delta$ interact. The figure is an illustration of bubble size threshold for the ions to respond to the reconnected field lines in magnetic reconnection.

frozen-in to the magnetic field. The deviation from MHD behavior began for system sizes smaller than about 10 ion inertial lengths. Turbulence simulations driven at scales small enough that the ions are not coupled at the energy containing scale have found that in the vicinity of reconnection sites, electrons are preferentially heated in the direction parallel to the magnetic field [Haynes et al., 2014].

An important question concerning electron-only reconnection regards the limiting length scales and timescales for its existence. Magnetic reconnection in a turbulent system occurs between magnetic "bubbles" associated with the fluctuations in the magnetic field. A schematic of magnetic field lines in turbulence generated from a 2D turbulence simulation [Phan et al., 2018] is shown in Figure 4.1a. Two reconnecting magnetic bubbles (flux tubes in a 2D geometry) in a turbulent system are highlighted, and the approximate scale size D of a bubble is shown. The scale D is approximately the largest length scale associated with the reconnection and plays an important role in determining the degree of ion-coupling to the reconnection. This length scale is roughly equivalent to the simulation domain size of conventional simulations of laminar reconnection. Hence, simulating different domain sizes in laminar reconnection simulations can help shed light on the degree of ion coupling to reconnection in turbulence.

Ultimately, at MHD lengths or timescales, the reconnection must eventually couple to the ions. However, previous simulations of this transition between ion-coupled and electron-only reconnection focused exclusively on the reconnection rate [Mandt et al., 1994]. In addition, this study focused on low ion plasma $\beta$ and anti-parallel reconnection, whereas reconnection in the solar wind or Earth's magnetosheath is often characterized by strong guide fields and plasma $\beta \sim 1$, a regime that has received very little attention. The variations of important observational properties in this regime during this transition remain unknown, i.e., the existence of frozen-in ion outflows, the ion outflow speed, and the width along the normal direction of the ion exhaust.

In this Chapter, we study the transition from ion-coupled to electron-only reconnection using kinetic particle-in-cell (PIC) simulations of magnetic reconnection. The initial inflow conditions for the simulation are relevant for turbulent reconnection

in the magnetosheath, i.e., relatively large plasma $\beta$ and weak magnetic shear. We simulate varying simulation domain sizes and examine the effect on the ion response to the reconnection. We find that the transition between fully ion-coupled and electron-only reconnection is gradual, spanning nearly a factor of ten in domain size. This transition is characterized by a gradual increase in the ion outflow velocity, the ion out-of-plane current, and the degree to which the ions are frozen-in to the magnetic field. Electron-only reconnection exhibits much faster reconnection rates because the magnetic field motion is not limited by the Alfvén speed. We develop a simplistic model for a newly reconnected field line which accurately predicts the scaling of peak ion outflows with domain size. A key finding is that the ion outflow velocity is largely controlled by the exhaust width along the current sheet normal direction.

We then explore the implications of our findings. First, the relationship between exhaust width and ion response gives specific predictions for both ion outflow speeds and ion out-of-plane current that can be compared with observations. Second, we examine how the properties of turbulence impact the degree of ion coupling in the resultant reconnection.

A terminology issue arises in the simultaneous analysis of laminar reconnection simulations and reconnection as an element of turbulence. The magnetic flux structures currently undergoing reconnection have been variously called "magnetic flux bundles" [Shay et al., 1998], "unreconnected magnetic islands" [Matthaeus and Lamkin, 1986], and possibly other names. The flux structures consisting of already reconnected magnetic field lines have been called "magnetic islands", "reconnected magnetic islands", "magnetic bubbles", and "plasmoids". To avoid confusion here, we will use the term "magnetic bubbles" to describe magnetic flux structures currently undergoing reconnection and "magnetic islands" for flux structures composed of already reconnected magnetic field. We emphasize that the use of the term "bubble" does not imply that the reconnection structures are small. In our usage a "bubble" could have a diameter of thousands of ion inertial lengths.

Section 4.2 describes the simulations performed in this study. In Section 4.3,

the simulation results and analyses are presented and the model for ion outflows is described. Section 4.4 discusses the implications for observational signatures of reconnection. Section 4.5 discusses how our findings impact our understanding of ion coupling to reconnection in turbulence. Finally, in Section 4.6 we review and discuss our scientific results.

## 4.2 Simulations

To study the physics of small-scale magnetic reconnection relevant to the turbulent magnetosheath (plasma $\beta \gtrsim 1$ and large guide field), we have performed 6 different simulations described in Table 4.1 using the parallel particle-in-cell (PIC) code P3D [Zeiler et al., 2002]. The simulations are 2.5 dimensional with periodic boundary conditions. Systems with the same aspect ratio but various sizes are used to examine the transition from ion-coupled to electron-only reconnection. Calculations are presented in the same normalized units as shown in Section 3.3.

The simulations are initialized with two current sheets, with the magnetic field along $x$ given by $B_x = B_{up} \{ \tanh[(y - 0.25\, L_y)/w_0] - \tanh[(y - 0.75 L_y)/w_0] - 1\}$, where $w_0$ is the half-width of the initial current sheets and $B_{up}$ is the inflowing reconnecting magnetic field. $n_{up}$ is the density outside the current sheets and the density is varied to maintain total pressure balance. A small local magnetic perturbation is added to start the reconnection, and the initial currents are due solely to electron flows. Run A, B, C, C2, D, and E have 6000 particles per grid (ppg) in the regions outside the current sheets, while run F has 1500 ppg. The lower ppg for run F was necessary to prevent the simulations from being too computationally expensive. Temperatures are initially uniform and there is also an initial uniform large guide field $B_z = B_g$. Parameters for the simulations are shown in Table 4.1. The inflow conditions are similar to Phan et al. [2018]. Note that because $B_{up} = 1$ and $n_{up} = 1$, velocities and reconnection rates are normalized to the inflowing Alfvén speed $c_{Aup}$. Lastly, the simulation sizes of run A through F are notated interchangeably by their domain sizes: $2.5d_i$, $5d_i$, $10d_i$, $20d_i$,

| Run | $\frac{m_i}{m_e}$ | $B_{\mathrm{up}}$ | $n_{\mathrm{up}}$ | $T_{\mathrm{e}}$ | $T_{\mathrm{i}}$ | $B_g$ | $c$ | $L_{\mathrm{x}}$ | $L_{\mathrm{y}}$ | $\Delta$ | $\beta$ | $w_0$ |
|---|---|---|---|---|---|---|---|---|---|---|---|---|
| A | 1836 | 1 | 1 | 11.51 | 115.16 | 8 | 300 | 2.56 | 2.56 | 0.005 | 3.89 | 0.06 |
| B | 1836 | 1 | 1 | 11.51 | 115.16 | 8 | 300 | 5.12 | 5.12 | 0.005 | 3.89 | 0.04 |
| C | 1836/16 | 1 | 1 | 11.51 | 115.16 | 8 | 100 | 10.24 | 10.24 | 0.02 | 3.89 | 0.065 |
| C2 | 1836/64 | 1 | 1 | 11.51 | 115.16 | 8 | 100 | 10.24 | 10.24 | 0.02 | 3.89 | 0.065 |
| D | 1836/16 | 1 | 1 | 11.51 | 115.16 | 8 | 100 | 20.48 | 20.48 | 0.02 | 3.89 | 0.22 |
| E | 1836/64 | 1 | 1 | 11.51 | 115.16 | 8 | 50 | 40.96 | 40.96 | 0.035 | 3.89 | 0.4 |
| F | 1836/64 | 1 | 1 | 11.51 | 115.16 | 8 | 50 | 81.92 | 81.92 | 0.04 | 3.89 | 0.6 |

**Table 4.1:** Plasma parameters of six simulations (Runs) : $m_i/m_e$ is the mass ratio of ion to electron and $B_{\mathrm{up}}$ and $n_{\mathrm{up}}$ are the inflowing reconnecting field and density outside the current sheet, respectively. $B_g$ is the uniform guide field, $\Delta$ is grid scale, $c$ is light speed, and ($L_{\mathrm{x}}$, $L_{\mathrm{y}}$) are simulation domain sizes. $\beta$ is the total beta including the guide field. $T_e$ and $T_i$ are the uniform electron and ion temperatures. $w_0$ is the initial current sheet thickness.

$40\mathrm{d_i}$, and $80\mathrm{d_i}$. The domain sizes are used where the use of length scales are deemed instructive.

## 4.3   Simulation Results and Discussion

An overview of the reconnection simulations are shown in Figure 4.2; the left column is the smallest simulation domain (run A) and the right column is run E.

The larger simulation exhibits standard ion-coupled reconnection (Figure 4.2b,d,f), with a quadrupolar $B_z$ perturbation, an ion outflow exhaust, and an electron flow characterized by super-Alfvénic flow close to the x-line, and then exhaust flows similar to the ions farther downstream. In contrast, the smallest simulation (Figure 4.2a,c,e) exhibits a quadrupolar $B_z$ perturbation that extends beyond the current sheet, negligible ion outflow, and electron outflows peaked near the separatrices. Due to the lack of ion response, we follow Phan et al. [2018] and call this "electron-only" reconnection. The $B_z$ perturbation which fills the inflowing region in this reconnection is generated in part by the electron inflow which by necessity is a current.

Shown in Figure 4.2g,h are cuts of the outflow velocities along the midplane ($y = 0$) compared to the $(\mathbf{E} \times \mathbf{B})_x/B^2$ (E × B) drift, which reveal the electron and ion coupling explicitly. In the electron-only case there are no ion flows and the electron
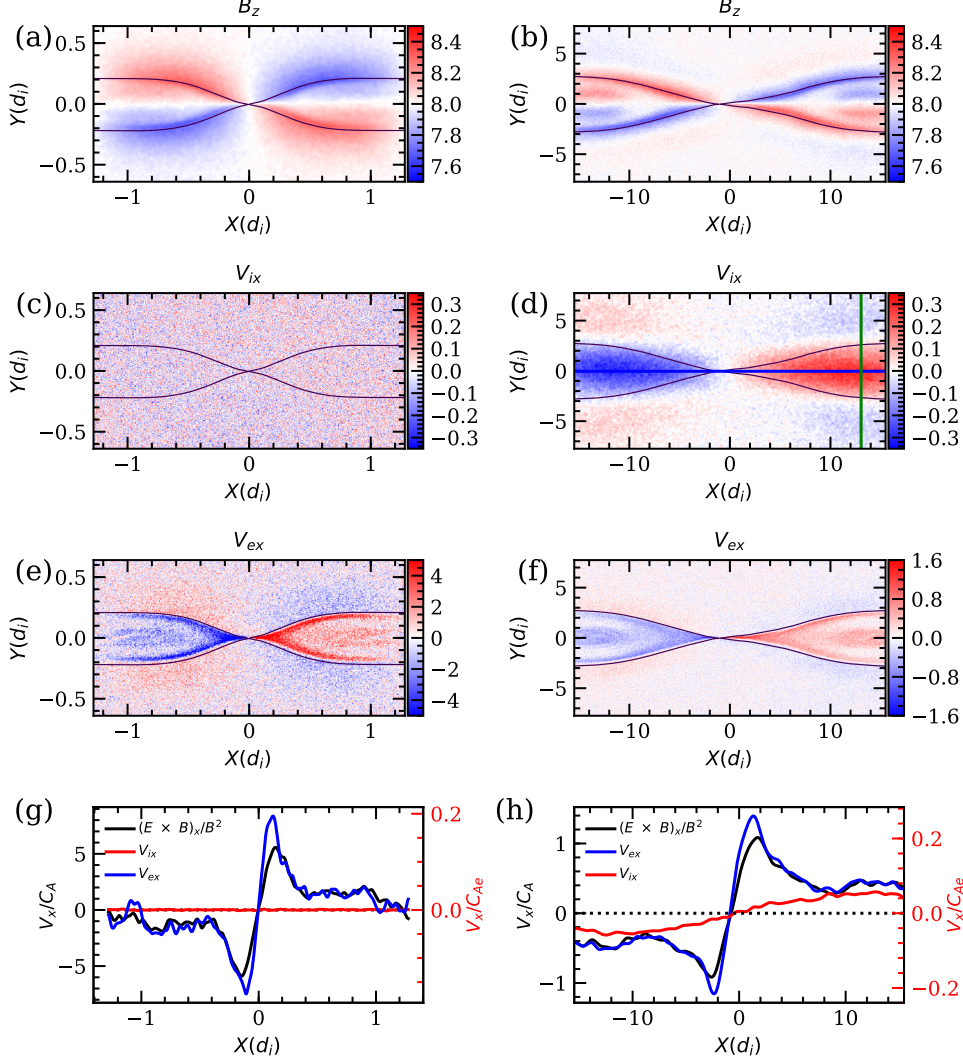
**Figure 4.2:** Overview of the reconnection simulations: time slice taken at $t = 0.265\Omega_i^{-1}$ for $2.5d_i$ (left column) and at $t = 27\Omega_i^{-1}$ for $40d_i$ (right column). (a) The quadrupolar structure of the out of plane magnetic field. (b) The out of plane magnetic field resembles that of a typical magnetic reconnection. (c) No ion exhaust velocity $V_{ix}$ is observed. (d) Significant ion outflows $V_{ix}$ are present. The intersection between the blue horizontal line and the green vertical line is the location of the maximum value of $V_{ix}$. (e) Electron outflow $V_{ex}$. The electron diffusion region is characterized by very fast collimated electron outflows near the x-line. (f) Peak electron jet close to the electron diffusion region is faster than the ion jets in (d). (g) A cut along $x$ at $y = 0$ is taken along the reconnection mid-plane. The electron outflow and $E \times B$ drift are very similar and $V_{ix}$ shows no ion response. (h) A cut along $x$ at $y = 0$ is taken along the reconnection mid-plane. Outside the diffusion region, $V_{ex}$ and $E \times B$ drift decrease slowly to match $V_{ix}$ at $\approx 10d_i$. The ions have fully coupled in this simulation.

outflow follows the E × B drift velocity closely. Note that for both simulations, this strong guide field reconnection has a significant $E_\parallel$ close to the x-line, so the electrons are not frozen-in there even though $V_{ex} \approx (\mathbf{E} \times \mathbf{B})_x / B^2$. For the ion-coupled reconnection in Figure 4.2h, the electron flows reach velocities much greater than the ions close to the x-line, and then slow down to roughly match the ion flows approximately 10 $d_i$ downstream of the x-line. The ions become frozen-in at this location with $V_{ix} \approx (\mathbf{E} \times \mathbf{B})_x / B^2$.

The electron response in the limit of a strong guide field but $\beta \gtrsim 1$ limit is somewhat surprising. Previous simulations with a strong guide field but much lower $\beta$ found a twisting of the electron current sheet (e.g., Swisdak et al. [2005]), a deflection of the electron outflow jet so that it was nearly at the separatrices (e.g., Pritchett [2001], Goldman et al. [2011]), a quadrupolar density perturbation [Kleva et al., 1995], and a warping of the quadrupolar structure of the Hall magnetic fields [Karimabadi et al., 1999]. However, in the present simulations, none of these features are present and the electron current layers and the Hall magnetic field resemble the antiparallel case. In other words, a quadrupole $B_z$, and electron $V_{ex}$ and $V_{ez}$ (not shown) are symmetric along the normal ($y$) direction. Kinetic PIC simulations with $\beta = 2$ but $T_i = T_e$ have found similar symmetry in the electron response [TenBarge et al., 2014, Muñoz et al., 2015].

Another important question raised by the strong guide field $\beta \gtrsim 1$ limit is the relative importance of the ion inertial length versus the ion Larmor radius in the transition from ion-coupled to electron-only reconnection. In reconnection simulations with $\beta \ll 1$ and strong guide fields, it has been found that the ion fluid Larmor radius $C_s / \Omega_{ci}$ determines the width of the ion diffusion region and thus the scale when the ions begin to decouple from reconnection (e.g., Kleva et al. [1995], Rogers et al. [2001], Stanier et al. [2015] and references therein), where $C_s$ is the sound speed. Determining the relative importance of the ion Larmor radius and the ion inertial length in this study is not possible because with $\beta \sim 1$ and $T_i / T_e \gg 1$, the two length scales are quite similar. Because of this ambiguity, we primarily discuss ion length

scales in terms of the ion inertial length for simplicity.

Due to the computational cost of larger simulations, smaller $m_i/m_e$ are used. Note that we have simulated two different mass ratios for the system size $10\,d_i$ i.e., runs C and C2. Both C and C2 show nearly identical results: the electron flows for electron-only reconnection are much greater than those for ion-coupled when normalized to the ion Alfvén speed (Figure 4.2g,h). However, when the electron flows are normalized to the electron Alfvén speed $c_{Ae}$, the peak electron flows are nearly identical; to highlight this fact, the right axes show values for $V_x/c_{Ae}$. At electron scales, both the very large and smallest simulations show quite similar behavior, as shown in Figure 4.3 that shows the electron scale behavior for the two simulations in Figure 4.2. When normalized to $c_{Ae}$, the ion $V_{ix}$ have different magnitudes because of their different electron masses. Also, note that in run E the X-line is moving, indicating that the X-line is not exactly the stagnation point for the ions and electrons.

As the ions couple more fully to the reconnection with increasing system size, the reconnection rate is lower because magnetic flux cannot flow away from the x-line as quickly as in the electron-only case. The reconnection rate $E_z$ is calculated by taking the time derivative of the magnetic flux between the x-point and the o-point. The reconnection rate $E_z$ versus time for the $40d_i$ simulation (Run E) is shown in Figure 4.4a. The reconnection rate rises and asymptotes to a value indicated by the horizontal black line in Figure 4.4a. The effect of system size on the quasi-steady value is shown in Figure 4.4b. As the simulation domain is increased the quasi-steady reconnection rate initially decreases, an effect which has been found in previous hybrid [Mandt et al., 1994] and kinetic PIC simulation studies [Shay and Drake, 1998]. Both of those studies determined that for smaller system sizes, whistler physics, as opposed to MHD, was controlling the reconnection rate. For larger systems, the reconnection rate stabilizes to a value consistent with previous reconnection scaling studies [Shay et al., 1999, Birn et al., 2001].

An important aspect of the transition between ion-coupled and electron-only reconnection that has not been previously addressed is the onset of ion flows. Clearly,
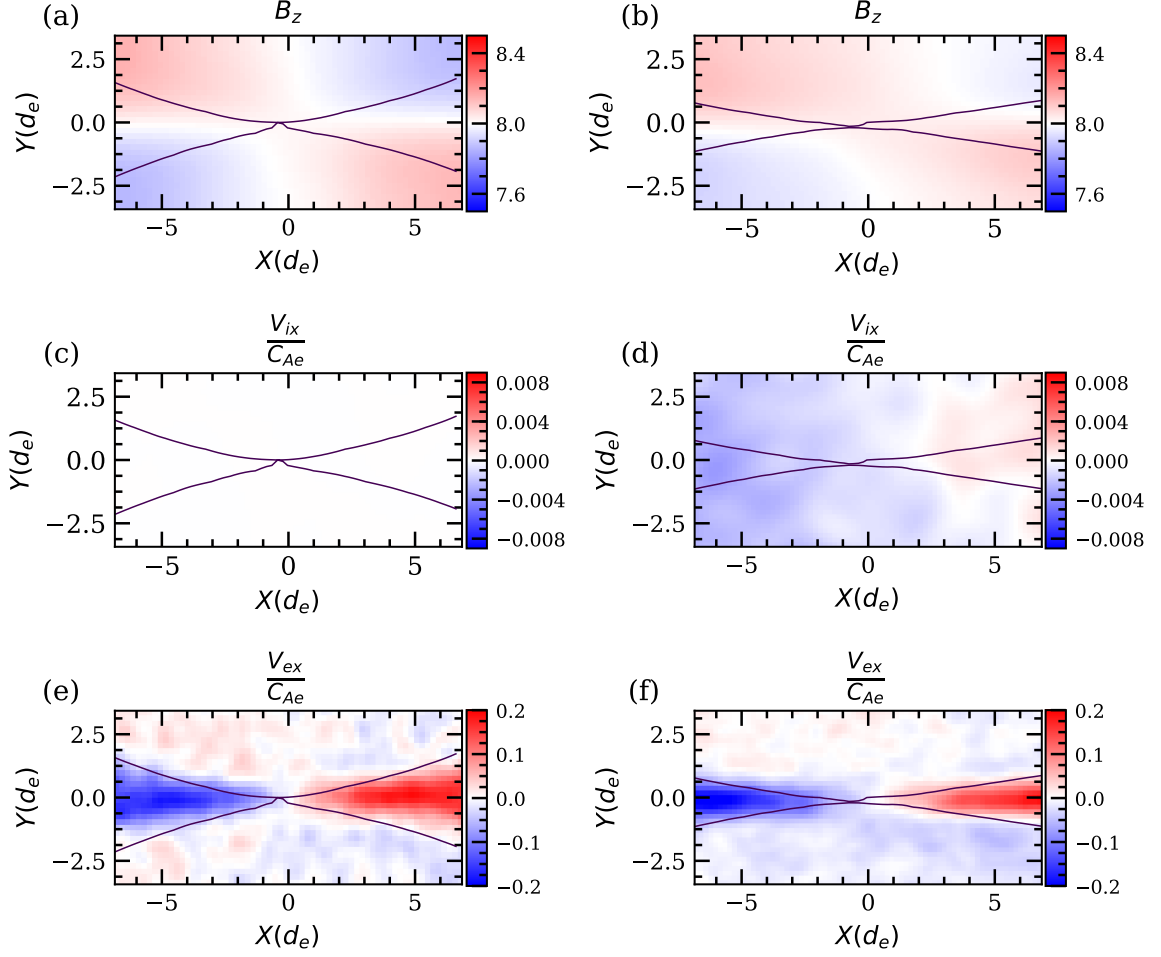
**Figure 4.3:** Zoomed-in panels of Figure 4.2 plotted near the X-line for a similar size when normalized to electron scales. The left column is run A and the right column is run E. The scale of each panel are shown in $d_e = c/\omega_{pe}$. Quadrupolar structure of the out of plane magnetic field $B_z$ is still present in (a) and (b). (c) and (d) show negligible ion exhaust velocities $V_{ix}/c_{Ae}$. The electron diffusion regions for panel (e) and (f) have very similar electron exhaust velocities $V_{ex}/c_{Ae}$.
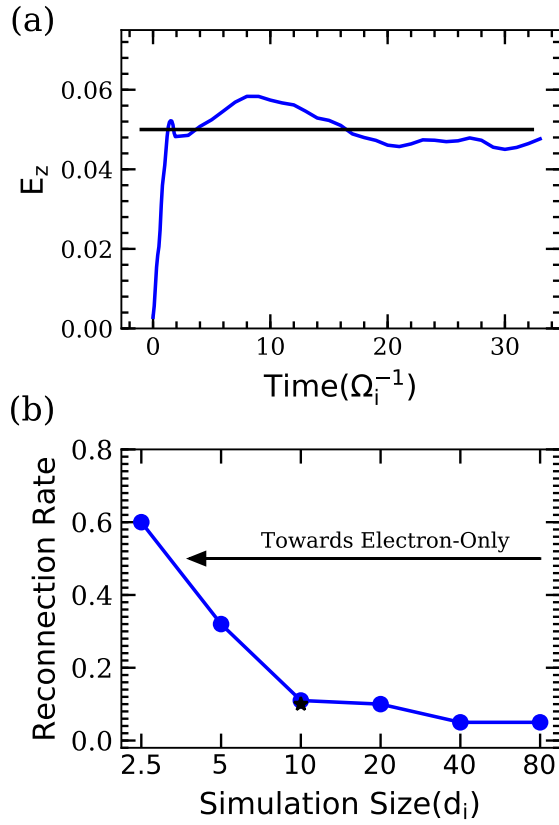
**Figure 4.4:** (a) Run E: Reconnection rate vs. time. The straight black line is the steady-state reconnection rate of 0.05 and the peak value is 0.06. (b) Reconnection rate vs. system size for all the simulations((*) denotes C2): Electron-only reconnection has a reconnection rate significantly larger than the ion coupled reconnection rates. Notably, the reconnection rate converges to 0.05 as MHD scales are realized.

as reconnection proceeds, and if the reconnection geometry extends to scales much greater than the ion inertial length, the ions will fully couple as in run E and F. However, is this transition sudden or does it gradually occur and what controls its onset? To address these questions, we study the ion flow properties as the system size is increased.

To characterize these ion flows, we begin with a cut along $x$ of $V_{ix}$ at the midplane of the exhaust in run E, an example of which is shown in Figure 4.2h. We average $0.1(c/\omega_{pi})$ above and below the midplane and a 1D-Gaussian filter is applied with a width corresponding to $0.07(c/\omega_{pi})$. Gaussian filtering proves to be an effective tool to reduce noise [Haggerty et al., 2017]. The peak outflow speed along this cut at $t \approx 27\Omega_i^{-1}$ is $|V_{ix}| \approx 0.32$ to the right of the x-point. The location of this peak outflow speed is also shown by the intersection of red vertical and blue horizontal line in Figure 4.2d. The peak outflow speed at each time is determined similarly, and the time evolution of this peak outflow speed is shown in Figure 4.5a. The outflow speed rises in time and reaches a peak of 0.32 before falling. We choose this peak value as the characteristic outflow speed for a given system size (simulation) and plot the results for each simulation in Figure 4.5d. It is clear from this figure that the characteristic ion outflow speed smoothly increases with system size.

The ion outflow velocity grows with system size because the ions can only fully couple to the reconnection process when the exhaust region is significantly larger than the ion inertial length (the ion Larmor radius is 1.34 $d_i$). The maximum width of the exhaust along the normal direction can be estimated as the total magnetic island width, which is shown for run E in Figure 4.5b; this width grows steadily in time as the reconnection proceeds. The ion outflow does not reach its characteristic speed until the total island width is a few ion inertial lengths wide ($t \approx 27$), as shown in Figure 4.5c. Intuitively then, the smaller simulation domains simply do not allow the magnetic island to become large enough to allow the ions to fully couple to the magnetic fields in reconnection, resulting in lower ion outflow velocities. This fact is highlighted in Figure 4.5e, which shows the characteristic ion outflow velocity versus the total island
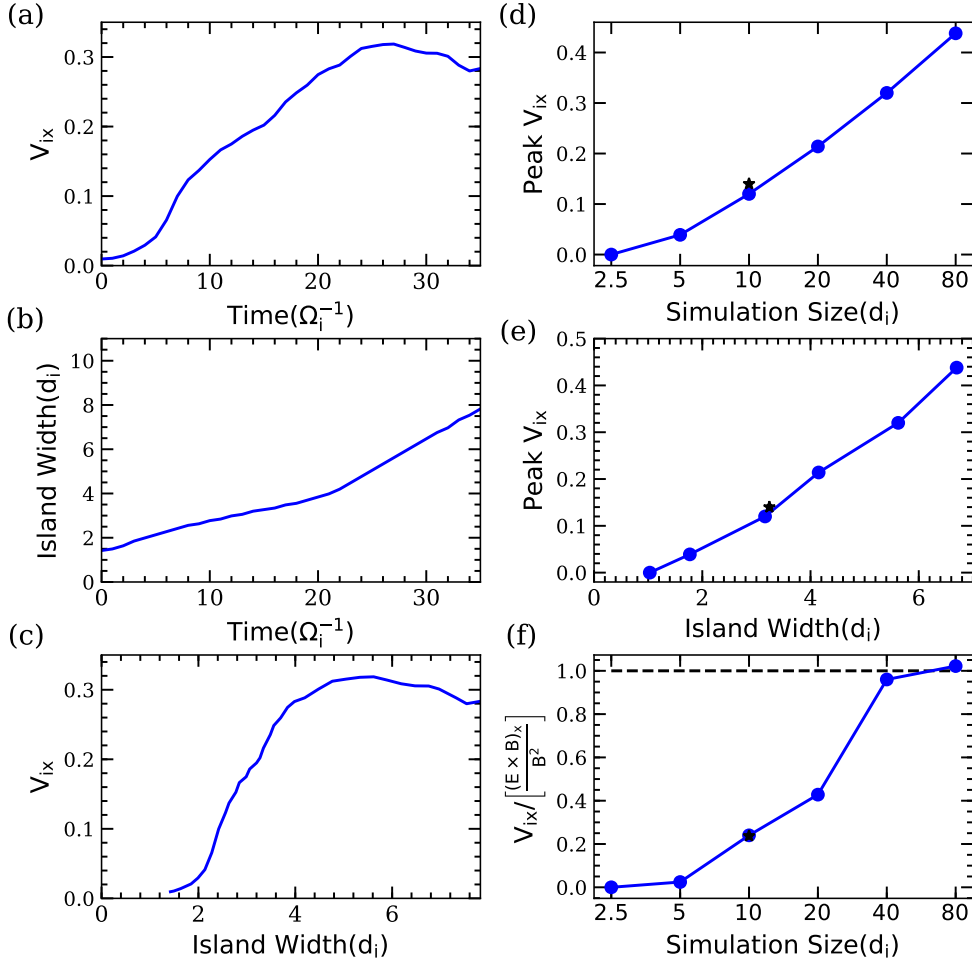
**Figure 4.5:** (a) Run E: Outflow speed vs. time. The outflow velocity is measured at the intersection of the horizontal blue and the vertical green line shown in Figure 4.2d for each time slice. The peak outflow velocity of about $\sim 0.32$ occurs at $t = 27$. (b) Run E: Total island width vs. time. The separatrices associated with the primary x-line form the boundary of the magnetic island. The total island width is the normal distance between the separatrices at the O-line. (c) Run E: Outflow velocity $V_{ix}$ versus island width. The peak value 0.32 is attained when the size of the island width is about $\sim 5.6d_i$. (d) All runs ((*) denotes C2): Peak $V_{ix}$ vs. system size of simulations. (e) All runs: Peak $V_{ix}$ vs. island width of simulations. The island width is measured at the time when the outflowing velocity $V_{ix}$ has peaked. (f) All runs: Ratio of the peak ion outflow $V_{ix}$ and $E \times B$ drift at the midplane. As the simulation size gets bigger, the ion outflow gradually reaches the $E \times B$ drift speed, indicating full ion coupling.

width for each simulation once this characteristic ion outflow speed is reached. It is clear from this figure that the transition to ion-coupled reconnection is gradual and not sudden, with the characteristic ion outflow speed smoothly increasing with system size. Further, in Figure 4.5f, we show the ratio of $V_{ix}$ and E × B drift for each simulation at its peak. As the system size increases, the characteristic ion outflow velocity catches up to the E × B drift velocity: another clear indication that the ions have fully coupled in the larger-size systems. We note that for the parameter regime simulated here, the ions are fully coupled for a system size of about $40\,d_i$ and larger. In contrast, the Mandt et al. [1994] study found that for system sizes of $10\,d_i$ or larger, the reconnection was fully in the MHD regime.

To understand more quantitatively the physics behind this transition from ion-coupled to electron-only reconnection, we study the physics controlling the contraction of a strongly-curved newly-reconnected field line by approximating this field line as a linear wave. For full ion-coupling, the wave is an Alfvén wave as expected. For decoupled ions, the wave is a kinetic Alfvén wave. Using linear Vlasov theory for the $T_i \gg T_e$ case, the transition between the two regimes occurs at $k\,\rho_i = 1$ [Howes et al., 2006, Schekochihin et al., 2009]. Although reconnection is a nonlinear phenomenon, this type of analysis has previously been used successfully to predict the electron outflow speed at sub-MHD length scales [Shay and Drake, 1998, Shay et al., 2001a, Cassak et al., 2010] and to study the propagation and damping of the Hall magnetic fields generated during reconnection [Shay et al., 2011, Pyakurel et al., 2018]. It has also been used to motivate why the global reconnection rate is "fast" i.e., independent of the dissipation mechanism and system size [Shay et al., 1999, Rogers et al., 2001], but this conclusion has been the source of significant and ongoing controversy (e.g., Bessho and Bhattacharjee [2005], Daughton and Karimabadi [2007], Chacón et al. [2008], TenBarge et al. [2014], Liu et al. [2014]). In this study we exclusively focus on using this type of model to give predictive insight into the ion reconnection exhaust velocity and we find that linear theory successfully predicts the scaling of this velocity.

The predicted ion outflow velocity is the bulk ion flow speed generated by

the wave, which in the MHD limit becomes the Alfvén speed based on the inflowing plasma conditions. The wavevector $\mathbf{k}$ is taken to be along $y$ with the background field $B_0 = \sqrt{B_y^2 + B_z^2}$, where $B_z$ is the guide field $B_g$ in Table 4.1; $B_y$ is chosen to be the value at the location of peak ion outflow, which is 0.18 for run E. The angle of propagation relative to the background field is $\theta = \tan^{-1}(B_z/B_y)$ and the wave propagates obliquely. The perturbation field is $B_x$, which is $B_{\mathrm{up}}$ in Table 4.1; $B_{\mathrm{up}} = 1$ for all of the simulations.

To determine the magnitude of $\mathbf{k}$, we examine the width $\delta$ of the ion $V_{ix}$ along $y$ as shown in Figure 4.6a. The cut is taken at the location where the ion $|V_{ix}|$ is peaked to the right of the x-line in Figure 4.2d, which is denoted by the vertical green line. The width $\delta \approx 3.3d_i$, which is the full width at half maximum, is converted to a wave number using $k \approx \frac{2\pi}{2\delta} \approx 0.94d_i^{-1}$.

Numerical solutions for the linear dispersion relation were calculated using the PLUME numerical solver [Klein and Howes, 2015]. For a set of equilibrium background parameters, in this work $\beta_i$, $T_i/T_e$, and $v_{th_i}/c$, PLUME determines the normal mode frequency $\frac{\omega}{\Omega_i}$ solutions of the hot plasma dispersion relation as a function of wavevector $\mathbf{k}d_i$, using a full Bessel Function representation of the ions and electrons as well as the associated eigenfunction fluctuations, e.g., the ion velocity flow shown in Figure 4.6b. As $k$ increases, the ion coupling to the wave decreases leading to a slower $V_{ix}$. The ion velocity has weak dependence on $\theta = \tan^{-1}(B_z/B_y)$ for these oblique angles. The two angles shown correspond to $B_y = 0.5$ and 0.1 but the two curves almost completely overlap. The dashed yellow vertical line denotes the value determined from Figure 4.6a, $k \approx 0.94d_i^{-1}$, giving the theoretical prediction for $V_{ix} \approx 0.43$ (dashed red line) shown in Figure 4.6b.

For all of the simulations in this study, a comparison of the measured versus theoretical predictions for the peak ion outflow are shown in Figure 4.7. The Vlasov prediction organizes the data in a straight line with a slope of approximately 0.75, shown as the dashed red line that is calculated using linear regression. For contrast, we also include a prediction from the isothermal two-fluid theory (see Formisano and

91
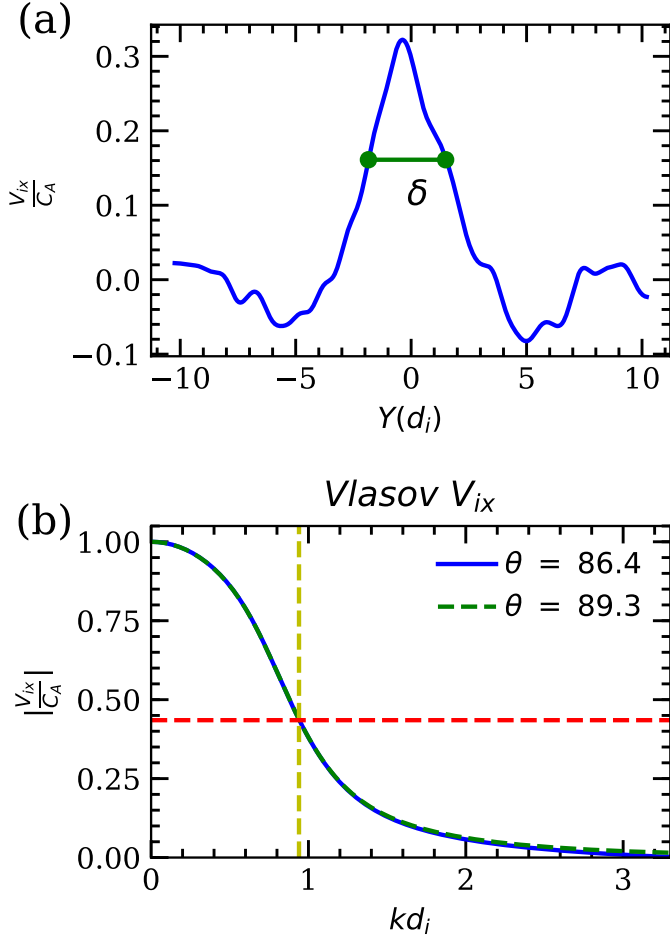
**Figure 4.6:** Run E: Determining the theoretical prediction of ion outflow velocity for run E at $t = 27\Omega_i^{-1}$ (a) Slice along $y$ of $V_{ix}$ at the location of peak $V_{ix}$ ($x = 13.04$ in Figure 4.2d and h). The width $\delta$ gives $k = (2\pi/2\delta)$. (b) $V_{ix}$ versus $kd_i$ from a numerical Vlasov dispersion solver [Klein and Howes, 2015]; two different angles of propagation $\theta = \tan^{-1}(B_z/B_y)$ are shown, corresponding to $B_y = 0.5$ and $0.1$. The dashed yellow vertical line shows the $kd_i$ value determined from (a), giving the theoretical prediction for $V_{ix}$ (dashed red line).
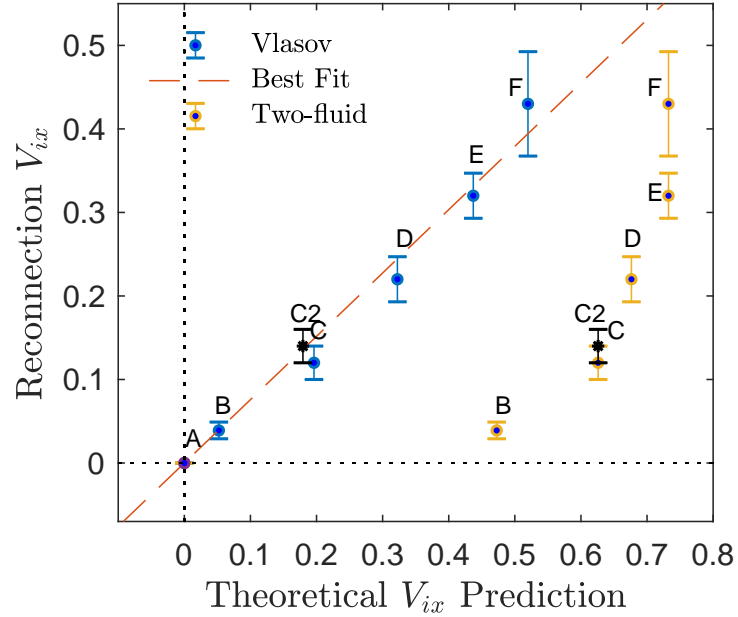
**Figure 4.7:** Comparison of the peak reconnection ion outflow velocity $V_{ix}$ with theoretical predictions. Theoretical predictions using both two-fluid and Vlasov dispersion relations are shown. The dashed red line with slope = 0.75 is the best fit line for the Vlasov prediction. The reconnection $V_{ix}$ are averaged values of $V_{ix}$ once they peak in each simulation. For example, run E is measured from Figure 4.5a when $t \approx 27\Omega_i^{-1}$. The uncertainty in $V_{ix}$ is estimated from the standard deviation of the fluctuations in time. Note that run C2 is not included in the fit for the best fit line.
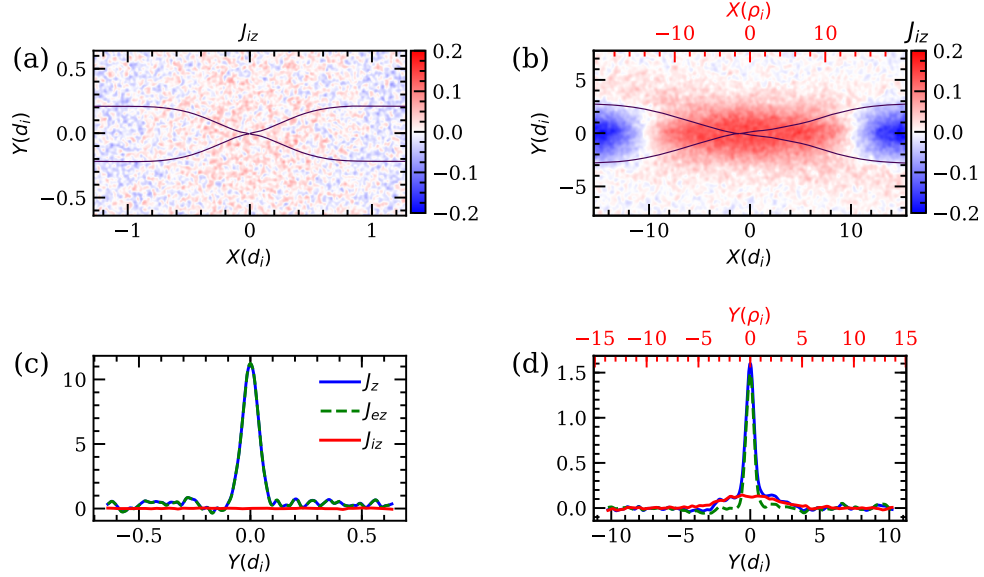
**Figure 4.8:** Time slice taken at $t = 0.265\Omega_i^{-1}$ for $2.5d_i$ (left column) and at $t = 27\Omega_i^{-1}$ for $40d_i$ (right column). (a) No out of plane ion current $J_{iz}$ is observed. (b) Significant out of plane ion currents $J_{iz}$ are present. (c) A cut along $y$ is taken at the location of peak $V_{ex}$ ($x = 0.11$ in Figure 4.2g). (d) A cut along $y$ is taken at the peak location of $V_{ex}$ ($x = 1.31$ in Figure 4.2h).

Kennel [1969] and Rogers et al. [2001]). Clearly due to the relatively high ion $\beta$, finite ion Larmor radius effects play an important role in the ion response to the reconnection. Note that the error bars for run F are significantly larger than the other simulations because of its lower particles-per-grid.

## 4.4 Implications for Reconnection Observations

Recent MMS observations of the turbulent magnetosheath [Phan et al., 2018] found smoking gun evidence for magnetic reconnection in the form of diverging super-Alfvénic electron plasma jets. The event was novel because it showed electron-only reconnection without ion coupling. First, the reconnection current sheet showed no evidence of the two-scale structure typical of ion-coupled reconnection ( Shay et al. [1998], Figure 3), i.e., a weaker ion-scale current sheet and an intense electron scale

current sheet. Previous observations of reconnection– both with ion reconnection outflows (e.g., Phan et al. [2007]) and without ion flows (e.g., Wilder et al. [2017]) –found that the reconnecting magnetic field exhibited two distinct ion scales consistent with ion and electron current sheets. Second, in the Phan et al. [2018] event the ions showed no change in their velocity due to the reconnected magnetic field lines. Additionally, no ion flows were measured in any of the current sheets that were observed. The simulations performed in this study have plasma inflow conditions often found in the downstream of a quasi-parallel bow shock in the magnetosheath (relatively high $\beta$, significant guide field), and can therefore provide some context for interpreting observations.

The transition from a two-scale ion-coupled sheet to an electron-only reconnection current sheet is evident in the simulations. Figure 4.8a and b show the Gaussian filtered ion out-of-plane current $J_{iz}$ for runs A and E, with both having the same color scale. Note that $|J_{iz}| \approx |V_{iz}|$ in this study because the density is nearly constant with a value of 1.0 because the flows are low Mach number. While run A shows no ion response, in run E the ions have a rectangular current sheet typically seen in ion-coupled reconnection [Shay et al., 1998]. This ion current sheet extends almost $10\,\mathrm{d_i}$ downstream from the x-line.

A spacecraft crossing the diffusion region in these two cases would see very different structures. In Figure 4.8c and d, we plot electron, ion, and total currents in a cut along $y$ through the location of peak electron outflow, i.e., near the outflow edge of the electron diffusion region. This smoothed cut is located at $x = 0.1$ and $x = 1.31$ for runs A and E, respectively. In the electron-only case, the only current comes from an electron current sheet with a total width of roughly $8\,\mathrm{d_e} \approx 0.2\,\mathrm{d_i}$. In contrast, the ion-coupled case (run E) exhibits a much wider ion current sheet: approximately $11\,d_i$. As with $V_{ex}$ in Figures 4.2g and h, the electron currents are smaller in run E because they roughly scale with $\sqrt{m_i/m_e}$.

Similar to $V_{ix}$, the transition between electron-only and ion coupled $J_{iz}$ signature is gradual as the system size increases. In Figure 4.9 is shown the peak value of $J_{iz}$ in each simulation plotted versus system size, showing a gradual increase in $J_{iz}$ with
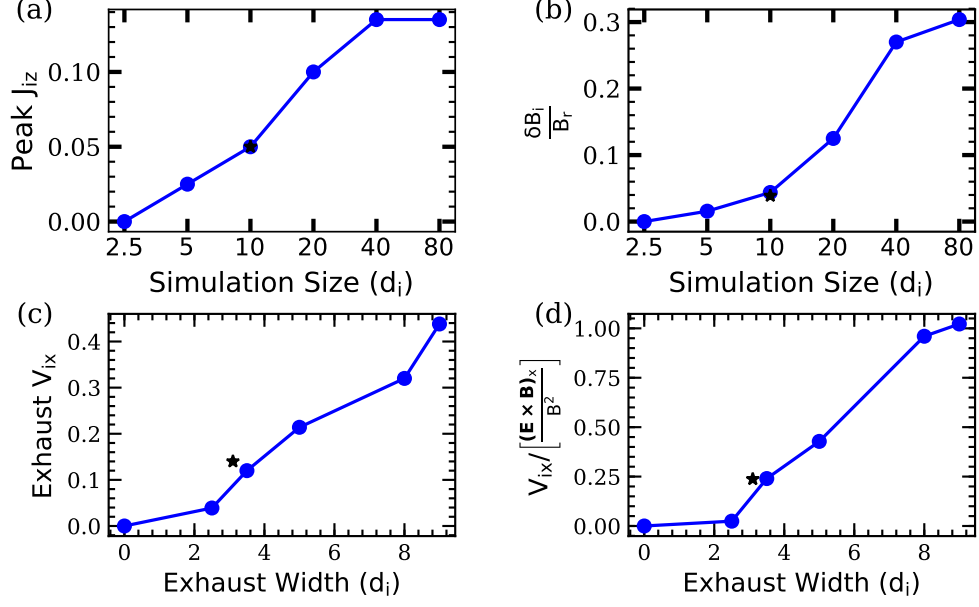
**Figure 4.9:** All runs: each point represents a simulation and (*) represents run C2. (a) Peak $J_{iz}$ gradually increases and plateaus at simulation size of $40d_i$. (b) Reduction in the inflowing reconnecting magnetic field for given simulations. (c) The peak ion exhaust velocities are plotted against the exhaust widths for given simulations. A gradual increase is seen. (d) The ion exhaust speeds normalized to $E \times B$ drift velocity for each simulation are plotted against the exhaust width.

system size until a plateau is reached for the largest two simulations. A cut along the mid-plane is taken and an average peak value is inferred from this cut to determine $J_{iz}$. Generally, the peak value of $J_{iz}/n_i$ in simulation normalized units is roughly half the peak value of $V_{ix}$ when compared with Figure 4.5d.

The larger scale ion current sheet causes a gradual reduction over ion scales of the reconnection magnetic field in the inflow region. The expected change in the magnetic field due to the ion current is calculated by integrating the ion current from deep in the inflow region to the center of the current sheet:

$$\delta B_i = \int_{-\text{inflow}}^{0} dy\, J_{iz} \approx \frac{1}{4}\, \Delta_i\, J_{iz\,\text{peak}}, \tag{4.1}$$

where $\Delta_i$ is the half width of the ion current sheet. For run E with $\Delta_i \approx 8\,\rho_i$, this approximation gives $\delta B_i/B_r \approx (1/4)\,(9.4)\,(0.13) \approx 0.3$. We calculate $\delta B_i/B_r$ for each

simulation by directly integrating $J_{iz}$ and the result is shown in Figure 4.9b. The magnetic perturbation gradually increases with system size but roughly asymptotes for the two largest systems at a value of around 0.3. The empirical findings for $\delta B_i/B_r$ may be testable with current satellite observations.

If fully developed reconnection is strongly coupled to the ions, a significant perturbation to the reconnection magnetic field would be expected at scales of several ion inertial lengths. These scales are of order 100 times larger than the thickness of the electron diffusion region for a realistic mass ratio, so a spacecraft such as MMS is very unlikely to see the deviation in the ion bulk flow if crossing through the electron diffusion region.

Another important insight from this study is that the width of the ion exhaust is linked to the peak outflow speed. The width of the ion exhaust is measured at the location of the peak ion velocity described in section 4.3. In Figure 4.9c we plot the peak outflow velocity for each simulation compared to the exhaust width. The peak velocity continues to increase up to exhaust widths of order $10\,d_i$. In Figure 4.9d, we plot the peak velocity normalized to the local $E \times B$ drift speed. This normalized velocity increases with exhaust width, ultimately plateauing when the ions become fully coupled for exhaust widths of around $8\,d_i$. If a satellite crossing the ion reconnection exhaust measured fully frozen-in ion outflow, it is expected that the exhaust width would be at least many ion inertial lengths.

## 4.5 Implications for Turbulence

Although the simulations and analyses thus far have focused on laminar reconnection geometries, the basic relationship between exhaust width and ion coupling can be applied to turbulent systems in which reconnection can occur between adjacent interacting magnetic bubbles (flux tubes) [Servidio et al., 2010]; we use the term "magnetic bubbles" to avoid confusion as discussed in the Introduction of this Chapter. Such an application can provide a causal linkage between turbulent length scales and the expected ion participation in subsequent reconnection. In Figure 4.1a, two

reconnecting magnetic bubbles (flux tubes in a 2D geometry) in a turbulent system are highlighted, where the approximate width of the exhaust $\Delta$ and diameter of the magnetic bubble D are shown. If the exhaust region is to have a width of at least several ion inertial lengths, it is necessary for the magnetic bubble size to be tens of ion inertial lengths.

The constraints on magnetic bubble size in order to allow ion involvement in reconnection can be estimated using geometric arguments. A diagram of the relevant configuration is shown in Figure 4.1b. Two magnetic bubbles, each of circular cross section and radius r interact, along the lines of what is seen in Figure 4.1a, but more simplified. Upon interaction, the boundary between the bubbles is flattened, each bubble distorted by a distance $\xi$, so that a region of width $\Delta = 2\xi$ emerges, in which the field strength drops to zero. The out-of-plane electric current density resides in this region. The flattened region defines the length $L$ of the associated reconnection zone. On geometrical grounds we argue that the region $L$ cannot reasonably be expected to be larger than r, as this would produce an extreme distortion and large stresses within the reconnecting flux tubes. Setting $L = r$, we find by construction that $(r - \xi)^2 + (r/2)^2 = r^2$. Throwing out a nonphysical solution with $\xi > r$, we find $\xi = (1 - \sqrt{3}/2)\, r$, giving a maximum value of $\Delta$ (or $\xi$) for a given bubble size r, namely $\xi = \Delta/2 = (1 - \sqrt{3}/2)r$. Consequently, to exceed a minimum specified $\xi$ requires that $r \gtrsim 8\xi$. For the minimum width $\xi$ needed for ion flows, we turn to the results of the previous sections, exemplified by the exhaust widths plotted in Figure 4.9c.

For the particular upstream (inflow) conditions used in this study, the smallest discernible ion flow in Figure 4.9c required an exhaust width of at least $\Delta \approx 2\, d_i$. For this minimal ion participation, the reasoning of the previous paragraph implies a reconnecting magnetic bubble radius of at least $r \approx 8\, d_i$. Similarly, for fully ion-coupled reconnection the requirement is an inter-bubble separation $\Delta \gtrsim 8\, d_i$, which corresponds to a minimum bubble size of $r \approx 30\, d_i$.

These estimates provide significant constraints on the properties of plasma turbulence if one anticipates that the reconnection in this turbulence is to have some

degree of ion response. For large turbulent systems spanning many $d_i$ in length scales, the smallest magnetic eddies produced in the cascade may be generated at sub-$d_i$ scales (see, e.g., Karimabadi et al. [2013]). The above considerations may limit ion participation in reconnection occurring between these very small bubbles (or magnetic eddies). At the other extreme, the largest magnetic bubbles in a system are expected to be roughly the size of the turbulence correlation length, and thus the largest scale reconnection events would also occur between bubbles of this size. Taking the threshold for minimal ion response to be $\Delta \approx d_i$ requires a magnetic bubble diameter or correlation length of at least ten ion inertial lengths. For fully coupled ions in reconnection occurring in the largest eddies, the correlation scale should be at least several 10s of ion inertial lengths. We purposely leave these constraints somewhat vague because the transition between ion-coupled and electron-only reconnection would be expected to have some dependence on inflow parameters. These estimates are consistent with recent studies of electron-only reconnection in turbulence [Califano et al., 2018], where the typical magnetic island size was less than $10\,d_i$. Such reconnection would be expected to have little coupling to the ions.

We note that in applying the geometrical arguments in this section we do not make assumptions regarding whether the bubbles reconnect completely nor whether magnetic flux is compressed upstream of the diffusion region (pileup reconnection). Turbulence simulations [Servidio et al., 2010] have found both pileup and non-pileup reconnection to exist, and kinetic simulations of pileup reconnection have noted that complete merging of bubbles may not occur [Karimabadi et al., 2011]. Pileup reconnection has been shown to occur at the interface of converging reconnection jets during magnetopause reconnection [Øieroset et al., 2019].

## 4.6 Conclusions

In order to study the physics controlling the transition from fully ion-coupled reconnection to electron-only, we have performed kinetic PIC simulations of magnetic reconnection with inflow conditions appropriate for the magnetosheath and the solar

wind: i.e., plasma $\beta$ greater than 1 and low magnetic shear. In our study, the ion inertial length is comparable to the ion Larmor radius. Simulations with varying domain sizes were performed to determine their effect on the reconnection rate and the ion response to reconnection: i.e., the peak ion outflow velocity, the frozen-in nature of the outflowing ions, and the generation of an ion current along the reconnection electric field (out-of-plane direction).

For small simulation domains up to about 5 ion inertial lengths, there is little or no ion response to magnetic reconnection. The magnetic field convection speed is not limited by the Alfvén speed which is consistent with previous studies (e.g., Mandt et al. [1994]) and the quasi-steady reconnection rate is much faster than typical MHD-scale magnetic reconnection. As the domain size is gradually increased, the coupling of the ion flows to the reconnected magnetic field gradually increases, becoming fully coupled for a domain size of around 40 ion inertial lengths. For this domain size and larger, the quasi-steady reconnection rate asymptotes to a rate comparable to previous MHD-scale studies (e.g., Shay et al. [1999]). The transition between electron-only and fully ion-coupled reconnection is smooth, with the ion outflows gradually becoming more frozen-in to the magnetic field as the domain size increases. The ion reconnection out-of-plane current (along the reconnection electric field) exhibits a similar gradual increase with domain size, reaching peak values of roughly one-half of the peak exhaust velocity.

As the domain size increases, the physics controlling the ion exhaust velocity changes from kinetic Alfvén physics to MHD physics. We study this physics by approximating a newly reconnected and contracting magnetic field line as a portion of a linear wave (e.g., Drake et al. [2008]; see Section 4.3 for a complete discussion). The wave number of the wave is roughly inversely proportional to the reconnection exhaust width. For smaller systems with higher wave numbers, the magnetic field line acts as a kinetic Alfvén wave as it contracts, with little or no ion response. With larger system sizes and smaller wave numbers, the wave acts as an MHD Alfvén wave with Alfvénic frozen-in ion outflows. Because of the simulation's large ion Larmor radius,

it is necessary to use a full Vlasov dispersion solver to determine the wave properties. We find good agreement between the ion outflow velocities predicted by the model and those observed in the reconnection simulations.

The limit of reconnection with strong guide field and $\beta \gtrsim 1$ has received little attention in the literature. Unlike previous guide field simulations with $\beta < 1$ ( Karimabadi et al. [1999], Swisdak et al. [2005]), there is no twisting of the electron current sheets or skewing of the Hall magnetic field. The electron currents and Hall magnetic fields have structure very similar to the antiparallel reconnection case for both $T_i \gg T_e$ in this study and $T_i = T_e$ [TenBarge et al., 2014, Muñoz et al., 2015].

We also examine how some observational signatures of reconnection vary with the degree of ion-coupling. First, an important observational clue to the degree of ion coupling has been the existence of an ion current along the out-of-plane direction surrounding the electron current sheet. As a spacecraft approaches the center of the reconnection current sheet, therefore, the reconnection magnetic field would reduce in magnitude over two different length scales. The lack of an ion scale reduction in the field (termed $\delta B_i$) provided important evidence that the Phan et al. [2018] event was electron-only reconnection. We find that the transition between electron-only and ion-coupled reconnection is characterized by a gradual increase in the ion out-of-plane current and thus $\delta B_i$, with $\delta B_i$ ultimately reaching values of about thirty percent of the asymptotic reconnection magnetic field.

Second, the width of the ion exhaust along the current sheet normal puts significant restrictions on both the ion flow speed and the coupling of the ions. In our simulations for a domain size of about 5 ion inertial lengths, a very small but discernible ion outflow exhaust occurred with a width of about 2 ion inertial lengths. On the other hand, to achieve frozen-in ion outflows required a minimum simulation domain of about 40 ion inertial lengths and a resultant exhaust width was about 8 ion inertial lengths.

Finally, the link between exhaust width and ion outflow velocity has implications for our understanding of turbulence, where turbulent fluctuations lead to reconnection

between magnetic bubbles. As mentioned in the introduction, to avoid confusion we call magnetic flux structures about to undergo reconnection as "magnetic bubbles," and already reconnected magnetic flux structures as "magnetic islands." Using geometric arguments for two reconnecting magnetic bubbles, we derive a relation between the bubble radius and the maximum reconnection exhaust width. Because the exhaust width ultimately determines the degree of ion-coupling to the reconnection, this degree can be linked to magnetic bubble size. In order to have any ion response to the reconnection, it is clear that the exhaust width must be greater than around one ion inertial length. Using our geometric relation then requires the magnetic bubble diameter to be greater than about 10 ion inertial lengths. For fully coupled ions an exhaust width $\gtrsim 5\, c/\omega_{pi}$ is required; thus, fully frozen-in ion exhausts would require a magnetic bubble size of at least several 10s of ion inertial lengths.

We note that there is some ambiguity associated with a threshold for "discernable" ion flows due to reconnection. To say the least, the ability to determine if a given ion flow is associated with reconnection will depend on the global conditions driving the reconnection. A strongly turbulent system would likely have ion shear flows surrounding the reconnection site as well as significant asymmetry in inflow conditions. In our simulations we were able to discern ion outflows of around five percent of the Alfvén speed in the inflow region.

Note also that the magnetic reconnection occurring in this study is well-developed reconnection, where the island width is at least $10 - 20$ electron inertial lengths. If the island width is much smaller, then the reconnection may be in a more transient onset phase. In that case the reconnection properties may be changing faster than the transit time of electrons through the diffusion region. If so, then time derivatives cannot be ignored and a Sweet Parker-like analysis of the diffusion region is not applicable. This will be a topic of future research.

An important extension of the current work will be to study three-dimensional effects on the physics controlling the ion coupling to reconnection. Three-dimensional effects can generate significant instabilities in the current sheets (e.g., Daughton et al.

[2011], Liu et al. [2013] and references therein). In addition, reconnection in finite length x-lines [Huba and Rudakov, 2002, Shay et al., 2003] may modify the conditions necessary for ion coupling. Finally, reconnection in fully 3D equilibrium geometries can have a significant impact on the process of reconnection (e.g., Priest et al. [2003], Dorelli et al. [2007], Sun et al. [2010] and references therein).

The three-dimensional nature of turbulence may also have an impact on the reconnection occurring as an element of turbulence. Quasi-two dimensionality is often used as a simplified model due to the propensity for turbulence to admit a dominance of gradients nearly perpendicular to the mean magnetic field, as evidenced by simulations [Oughton et al., 1994, TenBarge and Howes, 2012] and observations [Bieber et al., 1996, Sahraoui et al., 2010, Narita et al., 2011]. However, modeling studies Zhdankin et al. [2013], Wan et al. [2014] and observations [Matthaeus et al., 1990, Bieber et al., 1996] also point to the existence of an admixture of fluctuations that varies along the mean magnetic field. These fluctuations may impact the frequency and properties of reconnection. While studies of reconnection as an element of turbulence in two dimensions are numerous (e.g., Haggerty et al. [2017] and references therein), few studies have been performed in 3D. A few studies employing weakly three-dimensional reduced MHD simulations found distinctive effects, including that X-points were not always collocated with current sheets [Wan et al., 2014, Zhdankin et al., 2013]. The average reconnection rate was lower for X-points farther from current sheets. Future studies of reconnection in turbulence in 3D systems will help determine if these 3D effects fundamentally alter the transition from ion-coupled to electron-only reconnection.

# Chapter 5

# THREE DIMENSIONAL HIGH TEMPERATURE ELECTRON-ONLY RECONNECTION

This Chapter is a direct extension of Chapter 4. Three-dimensional "electron-only" reconnection is studied and a mechanism of faster reconnection in comparison to two-dimensional magnetic reconnection is proposed.

## 5.1  Introduction

Magnetic reconnection is an energy conversion process that converts magnetic energy rapidly into kinetic energy. Recently discovered electron-only reconnection found downstream of a quasi-parallel bow shock in the magnetosheath found no evidence of ion outflows due to the reconnected magnetic field lines [Phan et al., 2018]. This raises the question of the existence of the length and time scales of such tiny magnetic reconnection. The transition of such small scale "electron-only" reconnection to ion-coupled reconnection, in part, has been studied (e.g., Mandt et al. [1994], Sharma Pyakurel et al. [2019] and references therein). In the turbulent magnetosheath, magnetic reconnection– even with a clear ion exhaust detected exhibited much larger [Wilder et al., 2017, Eriksson et al., 2016] reconnection rates than previous observations [Genestreti et al., 2018, Nakamura et al., 2018]. The observed parallel electric field $E_\parallel$ close to the x-line in the Phan et al. [2018] event was $\sim 8$mV/m, but only $\sim 4$mV/m in the Wilder et al. [2017] event. These events when normalized to their upstream magnetic field and exhaust velocity are greater than 1 which is a clear evidence of faster reconnection than previous predictions [Shay and Drake, 1998, Shay et al., 1999, Hesse et al., 1999, Shay et al., 2007, Birn et al., 2001, Liu et al., 2017]. In this Chapter, we find that such fast reconnection could possibly be due to three dimensional effects.

104

**Table 5.1:** Simulation parameters: $\frac{m_i}{m_e}$ is ion to electron mass ratio, $B_g$ is the guide field and $L_x$, $L_y$ and $L_z$ are simulation lengths in $x$, $y$ and $z$. $\frac{c}{c_A}$ is the light speed. $\Delta$ and $dt$ are grid scale and time step, respectively. $w_0$ is the initial width of the current sheet. ppg is particles per grid.

| Simulations | $\frac{m_i}{m_e}$ | $B_g$ | $(L_x, L_y, L_z)$ | $\frac{c}{c_A}$ | $dt$ | $\Delta$ | $w_0$ | ppg |
|---|---|---|---|---|---|---|---|---|
| 2D | 1836 | 1 | (1,1,0) | 125 | 0.00002 | 0.0019 | 0.025 | 10000 |
| 3D | 1836 | 1 | (1,1,4.5) | 100 | 0.000036 | 0.0039 | 0.025 | 1000 |

We find that in a three-dimensional configuration, the plasma is released in the third dimension giving net mass flux loss which is not possible in a two-dimensional configuration. This ultimately provides an avenue for faster reconnection than the standard two-dimensional configuration.

## 5.2 Simulations

We perform two simulations using the massively parallel particle-in-cell (PIC) code P3D [Zeiler et al., 2002]. The simulations are initialized with two current sheets at $y = \frac{L_y}{4}$ and $y = \frac{3L_y}{4}$ with periodic boundary conditions. Each simulation contains a guide field $B_g$ of the same value as the reconnection magnetic field $B_x$. Calculations are presented in the same normalized units as shown in Chapter 3. We use force-free initial conditions in which the magnetic fields are given by $B_x = B_0 \{ \tanh[(y - 0.25\,L_y)/w_0] - \tanh[(y - 0.75L_y)/w_0] - 1\}$ and $B_z = \sqrt{B_0^2 + B_g^2 - B_x^2}$, where $w_0$ is the half-width of the initial current sheets. The out of plane magnetic field $B_z$ asymptotes to $B_g$ outside the current sheet. This configuration requires temperature anisotropy to be in kinetic equilibrium [Bobrova et al., 2001], however the pressure balance still holds so that the density is uniform initially. The initial current sheet solely consists of only electrons with ions as a neutralizing background. No initial perturbation is added to the simulations so that the reconnection is developed due to particle noise via current driven instability. Real mass ratio of $\frac{m_i}{m_e} = 1836$ is chosen for both the simulations. The parameters are summarized in Table 5.1.
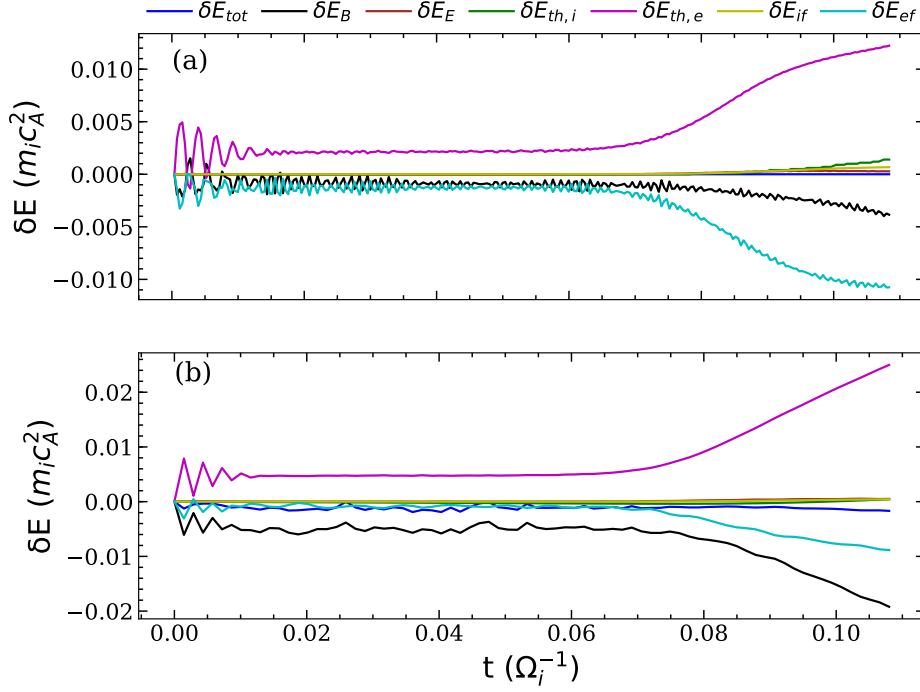
**Figure 5.1:** Evolution of energies versus time. (a) 2D simulation: Electron thermal energy increases rapidly while electron flow energy decreases starting around $0.06\Omega_i^{-1}$ indicating energy conversion due to electron scale magnetic reconnection. (b) 3D simulation: Electron thermal energy increase twice as much as 2D simulation with the magnetic energy is primarily converted.

## 5.3 Results

In Figure 5.1 are shown change of energies (e.g., $\delta E = E(t) - E(t = 0)$) calculated over the whole simulation domain in 3D and 2.5D simulations, where the electrical energy $\delta E_E$, magnetic energy $\delta E_B$, thermal energy of ions and electrons $\delta E_{th_{i,e}}$, flow energy of ions and electrons $\delta E_{f_{i,e}}$, and the total energy $\delta E_{tot}$ which is the sum of all the above mentioned energies are plotted against time $t(\Omega_i^{-1})$. It is seen in Figure 5.1(a) and Figure 5.1(b) that the gain in electron thermal energy in 3D simulation is approximately twice as large as 2.5D simulation shown by the magenta curves. This increase in electron thermal energy comes from the change in electron flow energy (pink curve) and magnetic field energy (black curve) for both the simulations. The
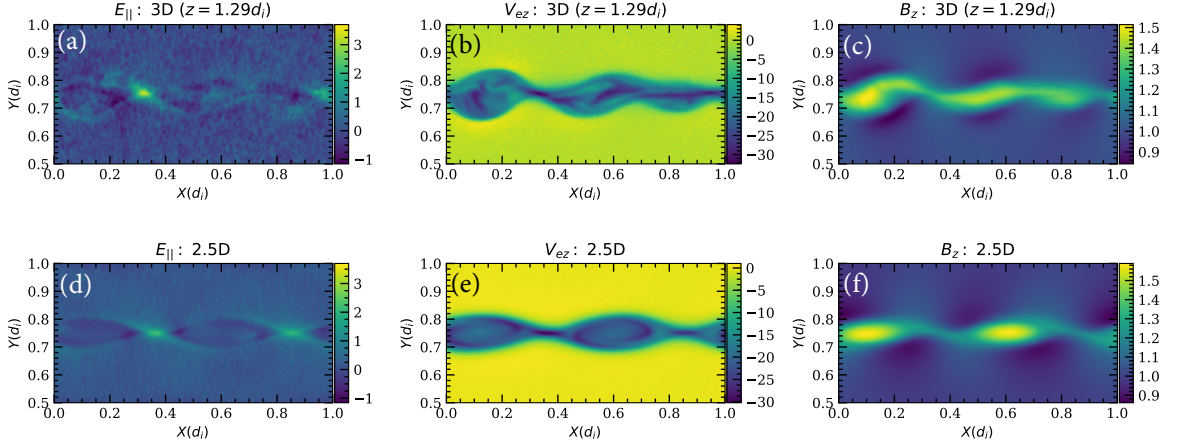
**Figure 5.2:** From left to right are parallel electric field $E_\parallel$, out-of-plane electron flows $V_{ez}$ and out-of-plane magnetic field $B_z$, respectively. The top panels are for the 3D simulation and the bottom are for the 2D simulation. The color scale are the same for both 3D and 2.5D simulations.

change in electron flow energy is of the same order for both simulations, however, it is seen that the conversion of magnetic field energy is the primary source of the increase in thermal energy of electrons in the 3D simulation which is not the case for 2.5D simulation. In both the simulations, we find that the onset of reconnection is close to $0.06\Omega_i^{-1}$ and the reconnection rate peaks at about $0.08\Omega_i^{-1}$. In 3D simulation, the onset of magnetic reconnection is accompanied by a bifurcation of the current sheet as in containing several peaks, observed in both in-plane and out of plane direction $\hat{z}$, somewhat similar to Dahlin et al. [2015]. Along the $z$-direction, this complex magnetic field and current sheet breaks up and gives very localized magnetic reconnection. In the top panels of Figure 5.2, a planar cut at $z = 1.29$ is shown for the 3D simulation and the bottom panels are for the 2.5D simulation. This location of $z = 1.29$ is chosen where the maximum value of $E_\parallel = 3.4$ is measured. Unlike the 3D simulation, the maximum value of $E_\parallel = 1.8$ is measured in 2.5D simulation. Clearly, $E_\parallel$ is about twice as large in the 3D simulation than measured in the 2.5D simulation. The middle and the right columns in Figure 5.2 are the out of plane electron flow velocities $V_{ez}$ pointing into the page and the out of plane magnetic field $B_z$ pointing out of the page.
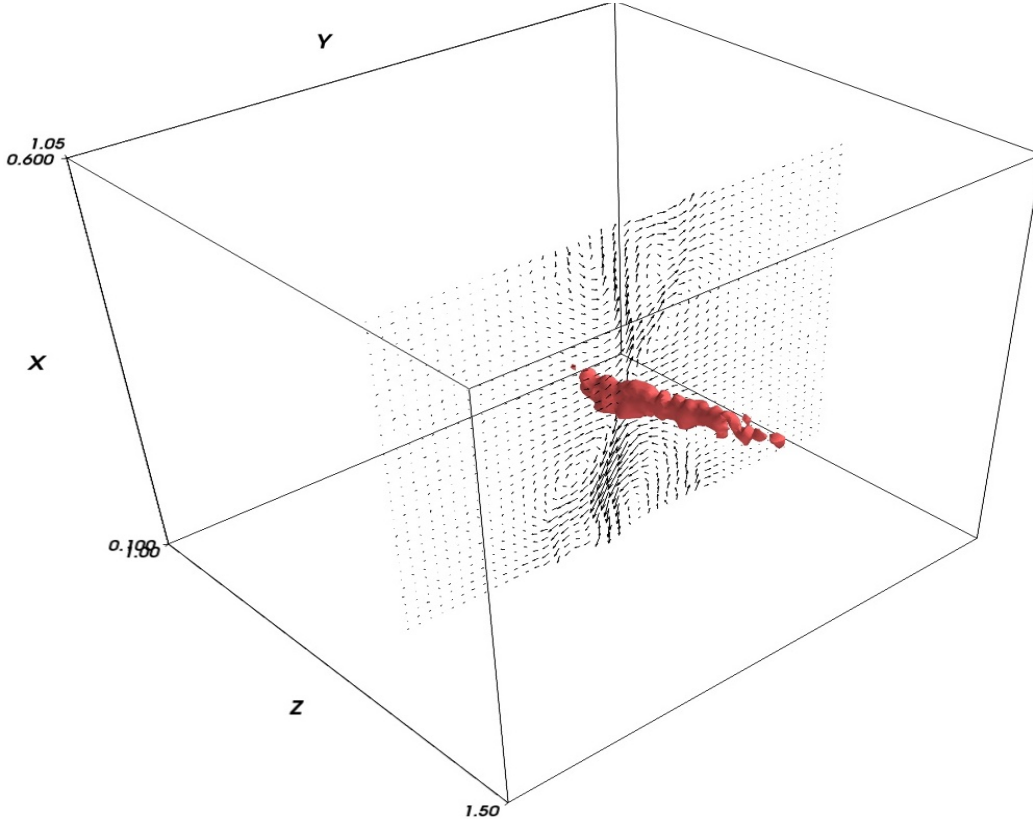
**Figure 5.3:** Isosurface of $E_{\parallel} = 2.5$ of the 3D magnetic reconnection simulation shown with perpendicular vector field $\vec{V}_{e\perp}$ in the xy-plane at $z = 1.29$. The $E_{\parallel}$ structure extends in $z$.

In the 3D simulation, on either side ($x$-direction) of the x-line, the reconnected field lines are not only constrained to evolve in the $xy$-plane but also evolve and traverse in the $z$-direction. This dramatically makes 3D simulation more turbulent while the 2.5D simulation does not have this property because $\frac{d}{dz} = 0$, implying no structures are formed in the $z$-direction, i.e., $k_z = 0$ [Drake and Swisdak, 2012, Dahlin et al., 2015]. Close to the x-line, both in 2.5D and 3D simulations, quadrupolar like structures of the out of plane magnetic field $B_z$ are also seen in Figure 5.2(c) & (f).

In Figure 5.3, an isosurface of $E_{\parallel} = 2.5$ is shown to extend in the $z$-direction. This $E_{\parallel}$ structure extends roughly from $z = 1.2$ to $z = 1.4$. At any point in time $t$ during the evolution of simulation, we do not find that $E_{\parallel}$ measured in the 2.5D simulation exceeds a value of 1.8. This leads us to conclude that the three dimensional

configuration plays a fundamental role in the enhancement of $E_\parallel$. Why do we observe larger $E_\parallel$ in the 3D versus 2.5D simulation? Before exploring this question, we examine the overall structure of magnetic reconnection in 3D. Figure 5.3 shows perpendicular electron flows $\vec{V}_{e\perp}$ in the $xy$-plane at $z = 1.29$. The inflowing plasma is shown to be pointing in the $-\hat{y}$ direction above $y = 0.75$ and in the $+\hat{y}$ direction below $y = 0.75$. To compare this perpendicular vector field $\vec{V}_{e\perp}$ in the 3D simulation with that in the 2.5D simulation, the same vector field is drawn in Figure 5.4(a) with the 2.5D simulation perpendicular electron flows $\vec{V}_{e\perp}$ drawn in Figure 5.4(b). The characteristics of perpendicular flows which show the electrons being ejected away from the x-line due to magnetic reconnection are somewhat similar in the 2.5D and 3D simulations. In 3D, however, the vector fields have additional vortex-like structures on either side of the direction of primary perpendicular flows of the electrons. For example, such prominent structures are located at about $(x, y) = (0.2, 0.74)$, $(0.26, 0.8)$ and $(0.4, 0.7)$ in Figure 5.4(a). This complicated structure extends in the $z$-direction in 3D giving an almost-spiral electron flow dubbed as "electron vorticity" [Hwang et al., 2019]. By virtue of reduced dimensionality, such structures are absent in 2.5D simulations as seen in Figure 5.4(b). These structures have only recently been discovered in MMS observations owing to its unprecedented time resolution [Hwang et al., 2019] and can be used as a proxy for the electron diffusion region.

To examine the complete three-dimensional structure of the 3D simulation, it is illuminating to plot electron flows in the $xz$ and $yz$-planes as well. Figure 5.5(a) shows the total electron flows where the primary flow is directed along $\hat{z}$. This is not so surprising as the electron flows are dominated by the equilibrium flows. On top of the equilibrium flows, the vector arrows clearly point away from the x-point at $x = 0.33$. To see the diverging electron jets due to the magnetic reconnection, we decompose the total flows once again into components parallel and perpendicular to the local magnetic field directions. A planar cut of the perpendicular electron flows in the $xz$-plane at $y = 0.75$ is shown in Figure 5.5(b). The extension of x-line is about $0.2d_i \sim 8.5d_e$ in the $z$-direction which corresponds to the length of the isosurface of $E_\parallel$ along $z$ shown
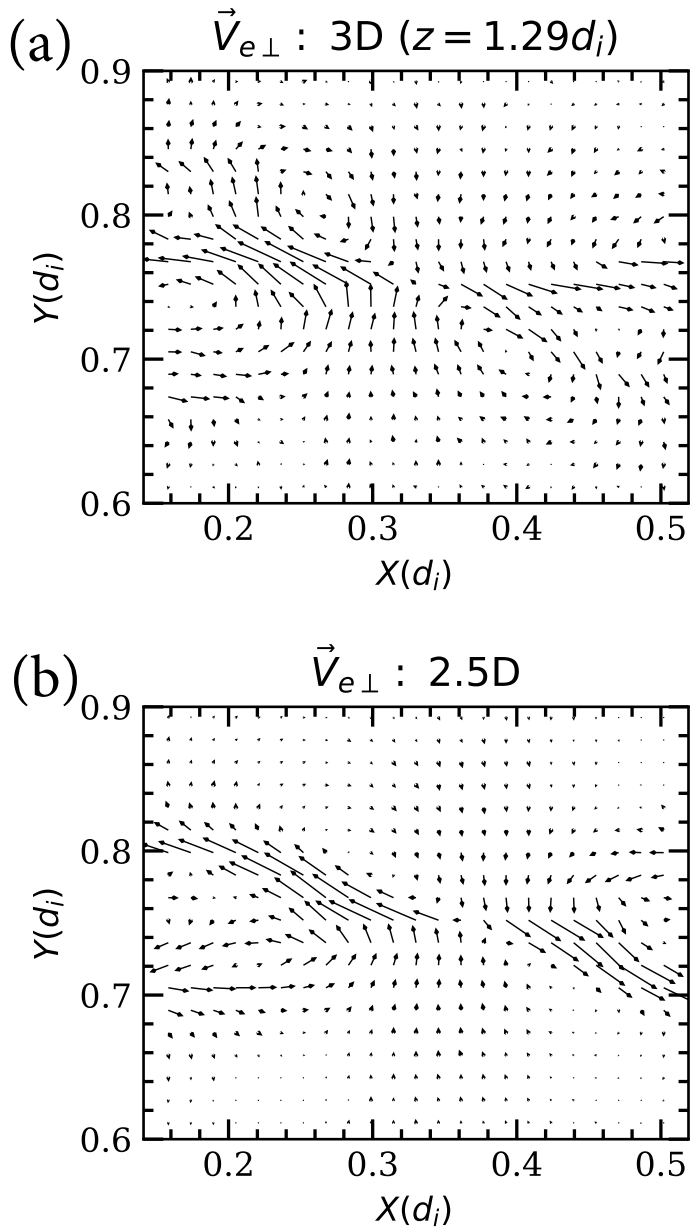
**Figure 5.4:** Similar perpendicular flows are seen in 3D and 2D simulations. (a) Spiralling vector field above $y = 0.76$ in 3D, not present in 2D simulations shown in (b).
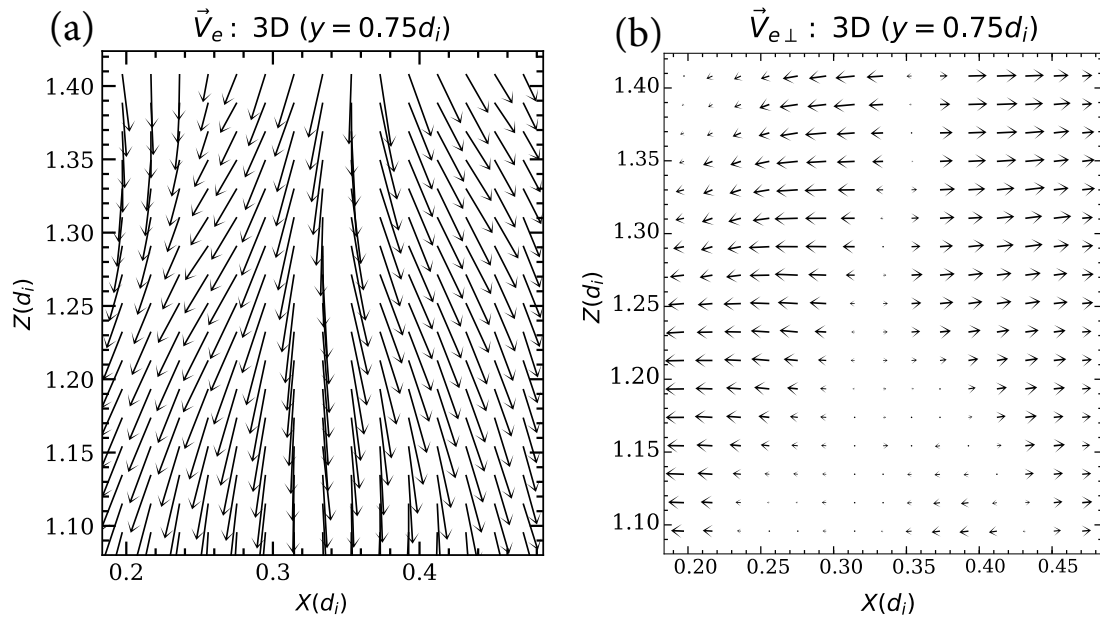
**Figure 5.5:** (a) Electron flows at $y = 0.75$ in the $xz$-plane. Diverging electron flows $\vec{V_e}$ seen along $x = 0.33$. (b) Perpendicular electron flows at $y = 0.75$ in the $xz$-plane is shown. Diverging electron flows $\vec{V}_{e\perp}$ are seen at $x = 0.33$ around which the maximum value of $E_\parallel$ is measured.
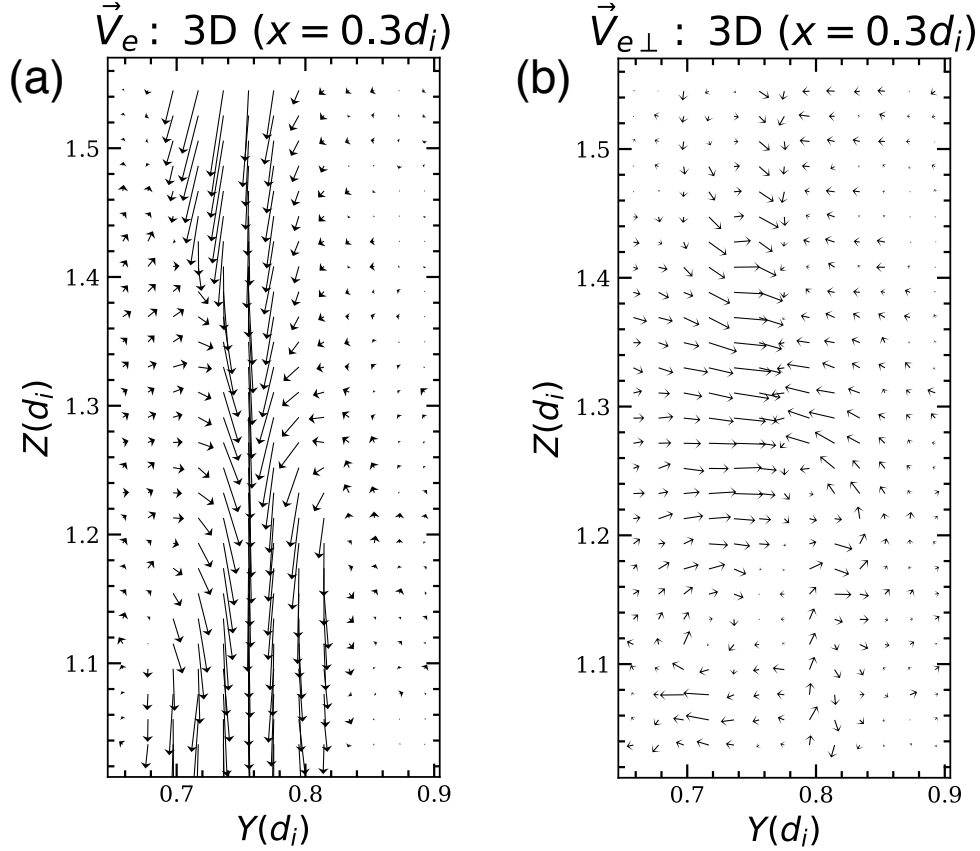
**Figure 5.6:** (a)Electron flows at $x = 0.3$ in the $yz$-plane: The flows converge around $y = 0.75$. (b) Perpendicular electron flows at $x = 0.33$ in the $yz$-plane is shown. Converging electron flows $\vec{V}_{e\perp}$ are seen along $y = 0.77$.

in Figure 5.3. Diverging electron flows at $x = 0.33$ are seen in Figure 5.5(b) which lie almost purely in the $x$-direction.

To examine the inflowing plasma that feeds the magnetic reconnection with electrons, the total electron flows velocities $\vec{V}_e$ are shown in Figure 5.6(a) in the $yz$-plane. This planar cut is taken at $x = 0.33$ right through the x-line. Once again, the vector field is dominated by the equilibrium flows, however, when the perpendicular flows $\vec{V}_{e\perp}$ are drawn, the direction of the inflowing plasma upstream of the x-line becomes very clear. This feature is seen in Figure 5.6(b). When $z < 1.2$, there are no inflowing plasma converging along $y \sim 0.77$. Thus, this 3D magnetic reconnection is
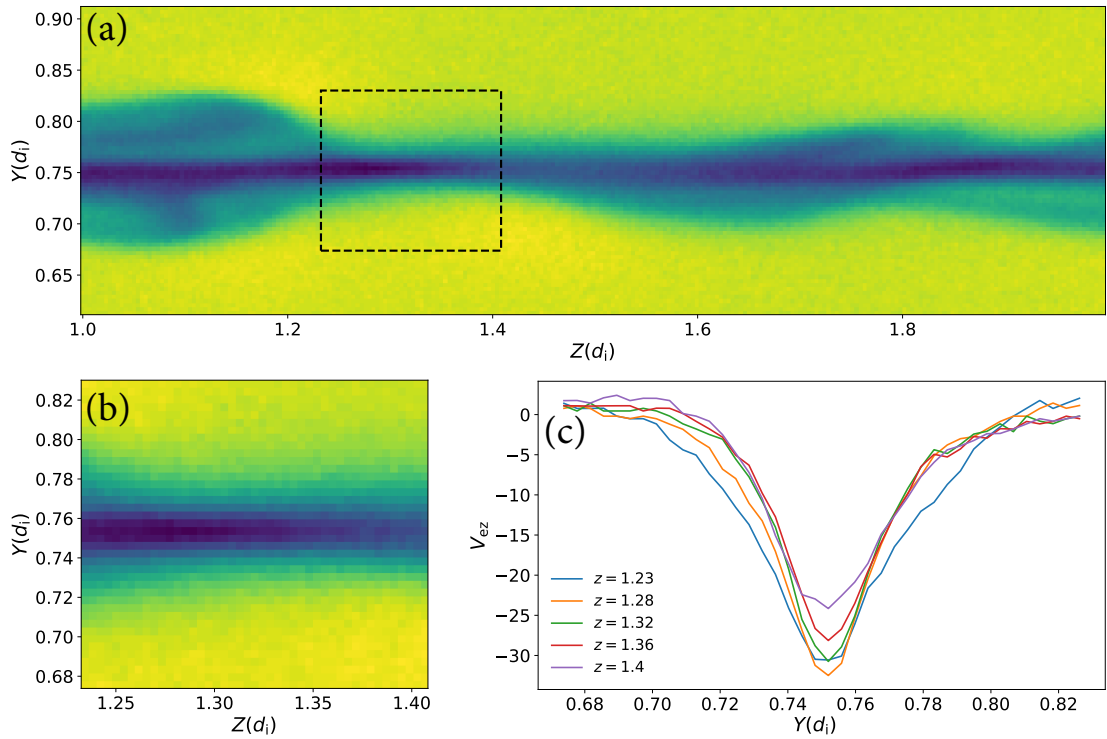
**Figure 5.7:** (a) $V_{ez}$ in the $yz$-plane at $x = 0.33$ is shown where $E_\parallel$ is localized along $z$. The dotted black rectangular box has the same length in $z$ as the diffusion region. (b) Zoomed-in $V_{ez}$ structure. (c) Cuts along $y$ at different $z$-locations are plotted. The electron flows $V_{ez}$ increase roughly from $-31$ to $-23$.
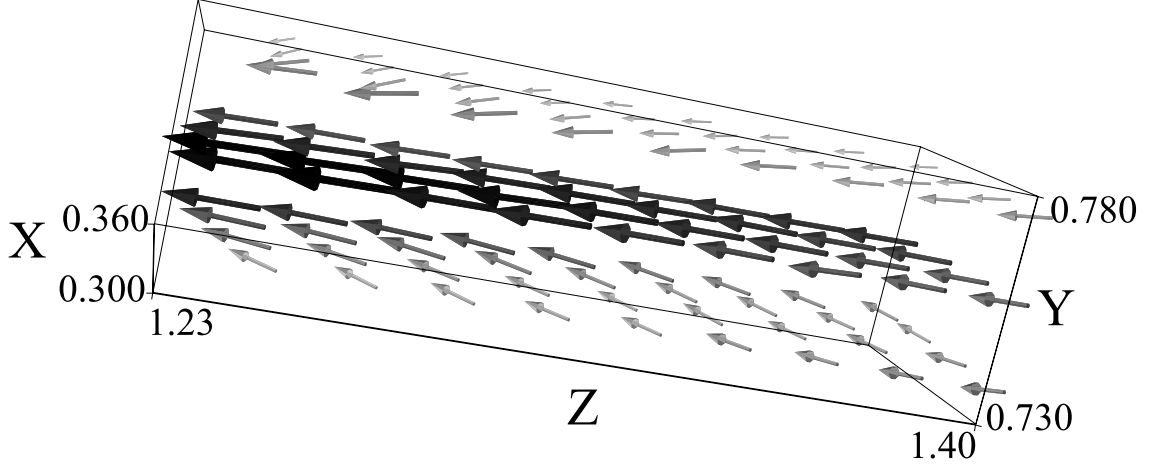
**Figure 5.8:** Three dimensional structure of $\vec{V_e}$ in the diffusion box: The vector arrows represent electron flows $\vec{V_e}$. The arrows are longer closer to $z = 1.24$ compared to $z = 1.4$.

highly localized. In addition, the extension of spiraling electron vorticity structure in the $z$-direction is seen at about $(y, z) = (0.75, 1.1)$.

Finally, we touch upon the mechanism of faster magnetic reconnection in three dimensions versus two dimensions by examining the structure of out of plane electron flows $V_{ez}$ along the $z$-direction. Figure 5.7(a) shows $V_{ez}$ in the $yz$-plane at $x = 0.33$. There are significant variations in $V_{ez}$ along $\hat{z}$. The dashed black rectangular box in this figure is identified as a local magnetic reconnection site. A zoomed-in figure of this region is shown in Figure 5.7(b). The length in the $z$-direction is chosen where $E_\parallel$ is enhanced. We take 1D cuts along $y$ at various $z$ locations in Figure 5.7(b) as shown in Figure 5.7(c). The magnitude of out of plane electron flow $V_{ez}$ decreases from $\sim 31$ to $\sim 23$ along these cuts. The flows to the left of $z = 1.24$ are larger than the flows to the right of $z = 1.4$. However, they point in the same direction: i.e., in the $-\hat{z}$ direction. This necessarily means that there is a net mass flux in $-\hat{z}$. In the two-dimensional configuration, this net mass flux is simply not possible. Thus the inflowing plasma in 3D has one more direction into which it is released without being replenished, which enables it to be faster than 2D configuration. Further, in steady state Sweet Parker

analysis of the 2D configuration, the plasma that flow in has to be ejected in a 2D plane. Under the steady state assumption, this is usually written as $v_{in}/v_{out} = \delta/\Delta$, where $\delta$ is the width of the diffusion box and $\Delta$ is the length of the diffusion box. While this assumption holds true for many magnetic reconnection events found in nature, it fails when significant variations along the direction of the current sheet are present. For example, in the present 3D simulation, the flows of electrons are not uniform in the $z$-direction. This is seen in Figure 5.8, where the arrows represent the total electron flows $\vec{V}_e$. This three-dimensional region is where the $E_\parallel$ structure is large and can be viewed as a 3D diffusion box. We now extend the steady state Sweet Parker analysis to 3D configuration. From the continuity equation, we have $\vec{\nabla} \cdot \vec{V}_e \sim 0$. The diffusion box now has length $l_z$ in the $z$-direction and a net flow which we denote by $V_{ez}^*$. Assuming that $\frac{\delta}{\Delta}$ stays constant, it can be shown that $V_{in} \sim \frac{\delta}{\Delta} V_{out} + \frac{\delta}{2l_z} V_{ez}^*$. If $l_z$ is large, we recover the 2D result.

## 5.4  Conclusions

We have explored the structure and properties of 3D electron-only reconnection soon after the initial onset of reconnection in a 1D force-free equilibrium. As discussed in Section 5.1, this work is motivated by the extremely large $E_\parallel$ observed during MMS crossings of electron exhausts in the magnetosheath. Normalized to the simulation upstream magnetic field and the electron exhaust velocity, we find that the normalized $E_\parallel$ in the 2D simulation is $\sim 0.25$ while the 3D simulation shows enhanced $E_\parallel \sim 0.6$. Though the reconnection rate is still considerably below the recent MMS observations, we find that 3D magnetic reconnection is clearly faster reconnection than 2.5D reconnection.

We explore the reasons for this larger reconnection rate and find that it is due relaxed constraints on electron mass continuity in the $xy$ plane. In 2D, all plasma enters the diffusion region by flowing roughly in the $y$ direction, and this same plasma must exit along the $x$ direction in a limited region of width comparable to the electron inertial length. In contrast, the inherently three-dimensional electron diffusion region

allows some plasma flowing along $y$ to ultimately escape from the diffusion region along the $z$ direction. This relaxes the constraint for flow along $y$, allowing the reconnection rate to be larger.

However, significant differences in reconnection inflow conditions exist between our simulations and the Phan et al. [2018] event. Those MMS observations measured a guide field eight times larger than the reconnection magnetic field and $\beta \sim 4$. This regime is not yet computationally tractable in three dimensions. It is possible that in this more realistic regime, simulations will show a much larger $E_\parallel$.

## Chapter 6

## CONCLUSIONS

Chapter 1 and 2 are basic plasma physics backgrounds that aid in understanding the magnetic reconnection phenomenon. In Chapter 1, we study the properties of magnetic reconnection in 2D configurations. A brief survey of magnetic reconnection events in the Earth's magnetosphere is presented, in which we list some important prior theoretical/simulation findings that explore reconnection rate in magnetic reconnection in various parameter regimes (high $\beta$, low $\beta$ and inclusion of guide field). We have also listed some important observational findings regarding magnetic reconnection. Sweet-Parker scaling analysis of the electron diffusion region is explored and the role of dispersive wave physics is presented in some detail. First, standing whistler wave dynamics is explored and its dynamical equations are derived. Second, a similar extension is laid out for standing kinetic Alfvén wave in the guide field limit. In this latter extension, using Sweet-Parker like scaling analysis, we have shown that the reconnection rate is independent of the width of the electron diffusion region. This result has not been presented in the literature to the best of our knowledge.

In Chapter 2, the properties of linear waves, including whistler waves and kinetic Alfvén waves, are explored using the two-fluid and kinetic models. We have used two-fluid model because it gives us an in-depth understanding of the relationships between electron and ion flows with respect to the magnetic field, the electric field and the density. It also helps us establish causal relationships. These causal relationships are presented in the form of causality diagrams, largely stemming from Professor Michael Shay's plasma physics coursework. Though they are not presented in plasma physics textbooks, I have found them to be extremely useful in understanding wave dynamics. There remains an open question as to why the ion flows are different in the two-fluid

117

model and the kinetic Vlasov model in the high $\beta$ regime at $k_\perp \rho_i \gtrsim 1$. It is seen that the dispersion relation between these two models differs perhaps due to finite ion Larmor radius effects but a detailed mathematical difference is yet to be worked out and needs to be addressed in the near future. The second half of Chapter 2 concerns with the collisionless damping mechanism of kinetic Alfvén wave. An analytic solution of the Landau damping rate of kinetic Alfvén wave is presented. This damping rate is also derived in Howes et al. [2006] in the gyro-kinetic limit. Along with the derivation of KAW, other ideal MHD waves are also derived to provide some context and clarity.

In Chapter 3, we find that the quadrupolar out-of-plane magnetic field associated with reconnection propagates away from the x-line as a kinetic Alfvén wave, also presented in Shay et al. [2011]. In this Chapter, we extend our findings to answer whether KAWs can propagate global distances before they damp, disperse or transform into some other wave modes. We explore if KAWs can travel $20 - 30 \mathrm{R}_e$ and generate aurora. The attenuation of this KAW is consistent with linear Landau damping theory. For magnetotail plasma conditions, KAWs can propagate tens of Earth radii with little damping with the potential to create white light aurora. Our findings appear to be quite robust, considering that this study uses both quasi-steady and time varying analysis of the magnetic field lines, and also spans a range of plasma parameters and ion to electron mass ratio. This study is however limited to uniform plasma background. The KAW propagation in the inner magnetosphere and auroral region will be the topic of future study. Also, it remains to be seen whether the inclusion of guide field would give consistent linear Landau damping results as is seen in our simulations. It is clear, however, that electron scale KAWs with $kd_s \gg 0.25$ will attenuate completely before reaching the inner magnetosphere. For the solar corona, on the other hand, all KAWs with $kd_s \gtrsim 0.02$ will damp long before reaching the photosphere.

In Chapter 4, we focus on small scale magnetic reconnection found in the turbulent magnetosheath. Dissipation of plasma turbulent energy is a ubiquitous phenomenon in our solar system which may play an important role in heating the solar

corona, the solar wind, and regions of the Earth's magnetosphere. In turbulent plasmas, magnetic reconnection has been suggested as a dissipation mechanism to damp away cascading fluctuations energy at small scales. Recent observations in the Earth's turbulent magnetosheath have shown surprisingly that reconnection can occur with no ion participation, so-called "electron-only" reconnection. Our understanding of the transition from ion-coupled reconnection to electron-only is lacking. In this Chapter, we study the physics controlling the transition from fully ion-coupled reconnection to electron-only reconnection. As the domain size is gradually increased, the coupling of the ion flows to the reconnected magnetic field gradually increases, becoming fully coupled for a domain size of around 40 ion inertial lengths. As the domain size increases, the physics controlling the ion exhaust velocity changes from kinetic Alfvén physics to MHD physics. For smaller systems with higher wave numbers, the magnetic field line acts as a kinetic Alfvén wave as it contracts, with little or no ion response. With larger system sizes and smaller wave numbers, the wave gradually acts as an MHD Alfvén wave with Alfvénic frozen-in ion outflows.

Using geometric arguments, we find that the magnetic bubbles associated with magnetic reconnection have to be greater than about 10 ion inertial lengths to measure any ion response. For fully coupled ions an exhaust width $\gtrsim 5$ is required; thus, fully frozen-in ion exhausts would require a magnetic bubble size of at least several 10s of ion inertial lengths. There are much to be learned when the reconnection is in a more transient onset phase. The time derivatives could have significant effects. In such scenarios, the usual Sweet-Parker like analysis of the diffusion region is no longer valid. This is a topic of future research. An important extension to this work is to study the response of ions in three-dimensional configuration. Chapter 5 is an extension of this work in three dimensions but confined to only electron length scales due to computational limitations.

In Chapter 5, 3D electron-only reconnection is presented and briefly explored. The parallel electric field (reconnection rate) at the x-line is shown to be much larger than its 2D counterpart. We investigate what makes the reconnection rate larger in

3D versus 2D. The inherently three dimensional electron diffusion region allows some plasma flowing along $y$ to ultimately escape from the diffusion region along the $z$-direction. This relaxes the constraint for flow along $y$, allowing the reconnection rate to be larger. The structure of the electron diffusion region is explored. Future extension of this work will be to explore more realistic regimes measured by MMS in the turbulent magnetosheath. In such regimes, it is yet to be seen whether we will measure yet larger $E_\parallel$.

In this PhD thesis, we have made significant breakthroughs associated with effects due to ion decoupling from the reconnection process. However, there are significant gaps in our understanding of what controls the degree of ion coupling and how it affects reconnection properties. Few studies of reconnection as an element of turbulence have been done in three-dimensional configuration. Much remains to be done in regards to understanding transition from ion-coupled to electron-only reconnection. It is yet to be seen whether the KAW scaling analysis in 2D will also hold true in three-dimensions. Can this transition be understood in turbulence simulations where the reconnection geometries are more complex? What role does asymmetric reconnection have in coupling of ions? How does the x-line spread in the $z$-direction in the electron-only reconnection? And lastly, what are the energies of electrons and ions if ions are fully coupled with reconnection in the three dimensional configuration? I end this conclusion with a paragraph from Alice's Adventures In Wonderland - Chapter 1.

> Either the well was very deep, or she fell very slowly, for she had plenty of time as she went down to look about her, and to wonder what was going to happen next. First, she tried to look down and make out what she was coming to, but it was too dark to see anything: then she looked at the sides of the well, and noticed that they were filled with cupboards and book-shelves: here and there she saw maps and pictures hung upon pegs. She took down ajar from one of the shelves as she passed: it was labeled "ORANGE MARMALADE" but to her great disappointment it was empty: she did not like to drop the jar, for fear of killing somebody underneath, so managed to put it into one of the cupboards as she fell past it.

# BIBLIOGRAPHY

H. Alfvén. Existence of Electromagnetic-Hydrodynamic Waves. *Nature*, 150:405–406, October 1942. doi: 10.1038/150405d0.

Tahar Amari, Aurélien Canou, and Jean-Jacques Aly. Characterizing and predicting the magnetic environment leading to solar eruptions. *Nature*, 514(7523):465–469, Oct 2014. doi: 10.1038/nature13815.

V. Angelopoulos, J. P. McFadden, D. Larson, C. W. Carlson, S. B. Mende, H. Frey, T. Phan, D. G. Sibeck, K.-H. Glassmeier, U. Auster, E. Donovan, I. R. Mann, I. J. Rae, C. T. Russell, A. Runov, X.-Z. Zhou, and L. Kepko. Tail Reconnection Triggering Substorm Onset. *Science*, 321:931, August 2008. doi: 10.1126/science. 1160495.

V. Angelopoulos, J. P. McFadden, D. Larson, C. W. Carlson, S. B. Mende, H. Frey, T. Phan, D. G. Sibeck, K.-H. Glassmeier, U. Auster, E. Donovan, I. R. Mann, I. J. Rae, C. T. Russell, A. Runov, X.-Z. Zhou, and L. Kepko. Response to comment on "Tail reconnection triggering substorm onset". *Science*, 324:1391–c, June 2009. doi: 10.1126/science.1168045.

A. Y. Aydemir. Nonlinear studies of m=1 modes in high-temperature plasmas. *Phys. Fluids B*, 4:3469, 1992.

D. N. Baker, T. I. Pulkkinen, V. Angelopoulos, W. Baumjohann, and R. L. McPherron. Neutral line model of substorms: Past results and present view. *J. Geophys. Res.*, 101:12975–13010, June 1996. doi: 10.1029/95JA03753.

D. N. Baker, T. I. Pulkkinen, V. Angelopoulos, W. Baumjohann, and R. L. McPherron. Neutral line model of substorms: Past results and present view. *Journal of Geophysical Research: Space Physics*, 101(A6):12975–13010, 1996. doi: 10.1029/95JA03753. URL https://agupubs.onlinelibrary.wiley.com/doi/abs/10.1029/95JA03753.

N. Bessho and A. Bhattacharjee. Collisionless reconnection in an electron-positron plasma. *Phys. Rev. Lett.*, 95:245001, Dec 2005. doi: 10.1103/PhysRevLett.95.245001. URL https://link.aps.org/doi/10.1103/PhysRevLett.95.245001.

J. W. Bieber, W. Wanner, and W. H. Matthaeus. Dominant two-dimensional solar wind turbulence with implications for cosmic ray transport. *J. Geophys. Res.*, 101:2511, 1996.

C. Birdsall and A. Langdon. *Plasma Physics Via Computer Simulation*. McGraw-Hall, New York, NY, 1985.

J. Birn, J. F. Drake, M. A. Shay, B. N. Rogers, R. E. Denton, M. Hesse, M. Kuznetsova, Z. W. Ma, A. Bhattacharjee, A. Otto, and P. L. Pritchett. GEM magnetic reconnection challenge. *J. Geophys. Res.*, 106:3715, 2001.

D. Biskamp. Magnetic reconnection via current sheets. *Phys. Fluids*, 29:1520, 1986.

D. Biskamp, E. Schwarz, and J. F. Drake. Ion-controlled collisionless magnetic reconnection. *Phys. Rev. Lett.*, 75(21):3850, 1995.

D. Biskamp, E. Schwarz, and J. F. Drake. Two-fluid theory of collisionless magnetic reconnection. *Phys. Plasmas*, 4:1002, 1997.

N. A. Bobrova, S. V. Bulanov, J. I. Sakai, and D. Sugiyama. Force-free equilibria and reconnection of the magnetic field lines in collisionless plasma configurations. *Physics of Plasmas*, 8:759–768, March 2001. doi: 10.1063/1.1344196.

S. Boldyrev and N. F. Loureiro. Magnetohydrodynamic Turbulence Mediated by Reconnection. *The Astrophysical Journal*, 844:125, August 2017. doi: 10.3847/1538-4357/aa7d02.

J. L. Burch, R. B. Torbert, T. D. Phan, L.-J. Chen, T. E. Moore, R. E. Ergun, J. P. Eastwood, D. J. Gershman, P. A. Cassak, M. R. Argall, S. Wang, M. Hesse, C. J. Pollock, B. L. Giles, R. Nakamura, B. H. Mauk, S. A. Fuselier, C. T. Russell, R. J. Strangeway, J. F. Drake, M. A. Shay, Y. V. Khotyaintsev, P.-A. Lindqvist, G. Marklund, F. D. Wilder, D. T. Young, K. Torkar, J. Goldstein, J. C. Dorelli, L. A. Avanov, M. Oka, D. N. Baker, A. N. Jaynes, K. A. Goodrich, I. J. Cohen, D. L. Turner, J. F. Fennell, J. B. Blake, J. Clemmons, M. Goldman, D. Newman, S. M. Petrinec, K. J. Trattner, B. Lavraud, P. H. Reiff, W. Baumjohann, W. Magnes, M. Steller, W. Lewis, Y. Saito, V. Coffey, and M. Chandler. Electron-scale measurements of magnetic reconnection in space. *Science*, 352:aaf2939, June 2016. doi: 10.1126/science.aaf2939.

J.L. Burch, K. Dokgo, K.J. Hwang, R.B. Torbert, D.B. Graham, J.M. Webster, R.E. Ergun, B.L. Giles, R.C. Allen, L.-J. Chen, S. Wang, K.J. Genestreti, C.T. Russell, R.J. Strangeway, and O. Le Contel. High-frequency wave generation in magnetotail reconnection: Linear dispersion analysis. *Geophysical Research Letters*, 46(8):4089–4097, 2019. doi: 10.1029/2019GL082471. URL https://agupubs.onlinelibrary.wiley.com/doi/abs/10.1029/2019GL082471.

F. Califano, S. S. Cerri, M. Faganello, D. Laveder, and M. W. Kunz. Electron-only magnetic reconnection in plasma turbulence. *ArXiv e-prints*, October 2018.

R. C. Carrington. Description of a Singular Appearance seen in the Sun on September 1, 1859. *Monthly Notices of the Royal Astronomical Society*, 20:13–15, November 1859. doi: 10.1093/mnras/20.1.13.

P. A. Cassak and M. A. Shay. Scaling of asymmetric magnetic reconnection: General theory and collisional simulations. *Phys. Plasmas*, 14:102114, 2007.

P. A. Cassak, M. A. Shay, and J. F. Drake. A saddle-node bifurcation model of magnetic reconnection onset. *Physics of Plasmas*, 17(6):062105, June 2010. doi: 10.1063/1.3435269.

P. A. Cassak, R. N. Baylor, R. L. Fermo, M. T. Beidler, M. A. Shay, M. Swisdak, J. F. Drake, and H. Karimabadi. Fast magnetic reconnection due to anisotropic electron pressure. *Physics of Plasmas*, 22(2):020705, February 2015. doi: 10.1063/1.4908545.

C. Cattell, J. Dombeck, J. Wygant, J. F. Drake, M. Swisdak, M. L. Goldstein, W. Keith, A. Fazakerley, M. André, E. Lucek, and A. Balogh. Cluster observations of electron holes in association with magnetotail reconnection and comparison to simulations. *J. Geophys. Res.*, 110:A01211, 2005. doi: 10.1029/2004JA010519.

S. S. Cerri and F. Califano. Reconnection and small-scale fields in 2D-3V hybrid-kinetic driven turbulence simulations. *New Journal of Physics*, 19(2):025007, February 2017. doi: 10.1088/1367-2630/aa5c4a.

L. Chacón, Andrei N. Simakov, and A. Zocco. Steady-state properties of driven magnetic reconnection in 2d electron magnetohydrodynamics. *Phys. Rev. Lett.*, 99: 235001, Dec 2007. doi: 10.1103/PhysRevLett.99.235001. URL https://link.aps.org/doi/10.1103/PhysRevLett.99.235001.

L. Chacón, Andrei N. Simakov, V. S. Lukin, and A. Zocco. Fast reconnection in nonrelativistic 2d electron-positron plasmas. *Phys. Rev. Lett.*, 101:025003, Jul 2008. doi: 10.1103/PhysRevLett.101.025003. URL https://link.aps.org/doi/10.1103/PhysRevLett.101.025003.

C. C. Chaston, J. W. Bonnell, C. W. Carlson, J. P. McFadden, R. E. Ergun, R. J. Strangeway, and E. J. Lund. Auroral ion acceleration in dispersive Alfvén waves. *J. Geophys. Res.*, 109:A04205, April 2004. doi: 10.1029/2003JA010053.

C. C. Chaston, T. D. Phan, J. W. Bonnell, F. S. Mozer, M. Acuńa, M. L. Goldstein, A. Balogh, M. Andre, H. Reme, and A. Fazakerley. Drift-Kinetic Alfvén Waves

Observed near a Reconnection X Line in the Earth's Magnetopause. *Physical Review Letters*, 95(6):065002, August 2005. doi: 10.1103/PhysRevLett.95.065002.

C. C. Chaston, J. R. Johnson, M. Wilber, M. Acuna, M. L. Goldstein, and H. Reme. Kinetic Alfvén Wave Turbulence and Transport through a Reconnection Diffusion Region. *Phys. Rev. Lett.*, 102(1):015001–+, January 2009. doi: 10.1103/PhysRevLett. 102.015001.

Francis F. Chen. *Introduction to plasma physics*. New York: Plenum Press, 1974.

L.-J. Chen, A. Bhattacharjee, P. A. Puhl-Quinn, H. Yang, N. Bessho, S. Imada, S. Mühlbachler, P. W. Daly, B. Lefebvre, Y. Khotyaintsev, A. Vaivads, A. Fazakerley, and E. Georgescu. Observation of energetic electrons within magnetic islands. *Nature Physics*, 4:19–23, January 2008. doi: 10.1038/nphys777.

E. W. Cliver and L. Svalgaard. The 1859 Solar-Terrestrial Disturbance And the Current Limits of Extreme Space Weather Activity. *Solar Physics*, 224:407–422, October 2004. doi: 10.1007/s11207-005-4980-z.

F. V. Coroniti. Laminar wave-train structure of collisionless magnetic slow shocks. *Nucl. Fusion*, 11:261, 1971.

S. Cowley. Frozen field lines and diffusion. *Lecture Notes in Physics, CMPD and CMSO Winter School*, 2006.

J. T. Dahlin, J. F. Drake, and M. Swisdak. Electron acceleration in three-dimensional magnetic reconnection with a guide field. *Physics of Plasmas*, 22(10):100704, October 2015. doi: 10.1063/1.4933212.

L. Dai. *Wave Dynamics in the Geomagnetic Tail*. PhD thesis, University of Minnesota, December 2009.

P. A. Damiano, J. R. Johnson, and C. C. Chaston. Ion temperature effects on magnetotail Alfvén wave propagation and electron energization. *J. Geophys. Res.*, 120: 5623–5632, July 2015. doi: 10.1002/2015JA021074.

P. A. Damiano, J. R. Johnson, and C. C. Chaston. Ion gyroradius effects on particle trapping in kinetic Alfvén waves along auroral field lines. *Journal of Geophysical Research (Space Physics)*, 121, November 2016. doi: 10.1002/2016JA022566.

W. Daughton and H. Karimabadi. Collisionless magnetic reconnection in large-scale electron-positron plasmas. *Physics of Plasmas*, 14(7):072303, July 2007. doi: 10. 1063/1.2749494.

W. Daughton, V. Roytershteyn, H. Karimabadi, L. Yin, BJ Albright, B. Bergen, and KJ Bowers. Role of electron physics in the development of turbulent magnetic reconnection in collisionless plasmas. *Nature Physics*, 7(7):539–542, 2011.

John Dawson. On landau damping. *The Physics of Fluids*, 4(7):869–874, 1961. doi: 10.1063/1.1706419. URL https://aip.scitation.org/doi/abs/10.1063/1. 1706419.

C. Day. Spacecraft probes the site of magnetic reconnection in earth's magnetotail. *Physics Today*, 54(10):16–17, October 2001. doi: 10.1063/1.1420541.

S. Donato, S. Servidio, P. Dmitruk, V. Carbone, M. A. Shay, P. A. Cassak, and W. H. Matthaeus. Reconnection events in two-dimensional hall magnetohydrodynamic turbulence. *Physics of Plasmas*, 2012. Submitted.

C. Dong, L. Wang, Y.-M. Huang, L. Comisso, and A. Bhattacharjee. Role of the Plasmoid Instability in Magnetohydrodynamic Turbulence. *Physical Review Letters*, 121(16):165101, October 2018. doi: 10.1103/PhysRevLett.121.165101.

J. C. Dorelli, A. Bhattacharjee, and J. Raeder. Separator reconnection at Earth's dayside magnetopause under generic northward interplanetary magnetic field conditions.

*Journal of Geophysical Research (Space Physics)*, 112:A02202, February 2007. doi: 10.1029/2006JA011877.

J. F. Drake. Magnetic reconnection: a kinetic treatment. In B. U. Ö. Sonnerup, P. Song, and M. Thomsen, editors, *Physics of the Magnetopause*, volume 90 of *Geophysical Monograph*, page 155. American Geophysical Union, 1995.

J. F. Drake and M. Swisdak. Ion Heating and Acceleration During Magnetic Reconnection Relevant to the Corona. *Space Science Reviews*, 172:227–240, November 2012. doi: 10.1007/s11214-012-9903-3.

J. F. Drake, M. A. Shay, W. Thongthai, and M. Swisdak. Production of energetic electrons during magnetic reconnection. *Phys. Rev. Lett.*, 94:095001, 2005.

J. F. Drake, M. Swisdak, H. Che, and M. A. Shay. Electron acceleration from contracting magnetic islands during reconnection. *Nature*, 443:553, 2006.

J. F. Drake, M. A. Shay, and M. Swisdak. The hall fields and fast magnetic reconnection. *Phys. Plasmas*, 15:042306, 2008.

J. W. Dungey. Conditions for the occurrence of electrical discharges in astrophysical systems. *Phil. Mag.*, 44:725, 1953.

J. W. Dungey. The Neutral Point Discharge Theory of Solar Flares. a Reply to Cowling's Criticism. In B. Lehnert, editor, *Electromagnetic Phenomena in Cosmical Physics*, volume 6 of *IAU Symposium*, page 135, 1958.

E. Eriksson, A. Vaivads, D. B. Graham, Yu. V. Khotyaintsev, E. Yordanova, H. Hietala, M. André, L. A. Avanov, J. C. Dorelli, D. J. Gershman, B. L. Giles, B. Lavraud, W. R. Paterson, C. J. Pollock, Y. Saito, W. Magnes, C. Russell, R. Torbert, R. Ergun, P-A. Lindqvist, and J. Burch. Strong current sheet at a magnetosheath jet: Kinetic structure and electron acceleration. *Journal of Geophysical Research: Space Physics*, 121(10):9608–9618, 2016. doi: 10.1002/2016JA023146.

E. Fermi. On the Origin of the Cosmic Radiation. *Physical Review*, 75:1169–1174, April 1949. doi: 10.1103/PhysRev.75.1169.

L. Fletcher and H. S. Hudson. Impulsive Phase Flare Energy Transport by Large-Scale Alfvén Waves and the Electron Acceleration Problem. *Astrophys. J*, 675:1645-1655, March 2008. doi: 10.1086/527044.

V. Formisano and C. F. Kennel. Small amplitude waves in high $\beta$ plasmas. *Journal of Plasma Physics*, 3:55–74, February 1969. doi: 10.1017/S0022377800004189.

Luca Franci, Silvio Sergio Cerri, Francesco Califano, Simone Landi, Emanuele Papini, Andrea Verdini, Lorenzo Matteini, Frank Jenko, and Petr Hellinger. Magnetic reconnection as a driver for a sub-ion-scale cascade in plasma turbulence. *The Astrophysical Journal Letters*, 850(1):L16, 2017. URL http://stacks.iop.org/2041-8205/850/i=1/a=L16.

L. A. Frank, K. L. Ackerson, and R. P. Lepping. On hot tenuous plasmas, fireballs, and boundary layers in the earth's magnetotail. *Journal of Geophysical Research (1896-1977)*, 81(34):5859–5881, 1976. doi: 10.1029/JA081i034p05859. URL https://agupubs.onlinelibrary.wiley.com/doi/abs/10.1029/JA081i034p05859.

H. U. Frey, T. D. Phan, S. A. Fuselier, and S. B. Mende. Continuous magnetic reconnection at earth's magnetopause. *Nature*, 426:533, 2003.

S. P. Gary. *Theory of Space Plasma Microinstabilities*. Cambridge Atmospheric and Space Science Series. Cambridge University Press, New York, NY, 1993.

K. J. Genestreti, T. K. M. Nakamura, R. Nakamura, R. E. Denton, R. B. Torbert, J. L. Burch, F. Plaschke, S. A. Fuselier, R. E. Ergun, B. L. Giles, and C. T. Russell. How accurately can we measure the reconnection rate em for the mms diffusion region event of 11 july 2017? *Journal of Geophysical Research: Space Physics*, 123(11): 9130–9149, 2018. doi: 10.1029/2018JA025711.

D. J. Gershman, A. F-Viñas, J. C. Dorelli, S. A. Boardsen, L. A. Avanov, P. M. Bellan, S. J. Schwartz, B. Lavraud, V. N. Coffey, M. O. Chandler, Y. Saito, W. R. Paterson, S. A. Fuselier, R. E. Ergun, R. J. Strangeway, C. T. Russell, B. L. Giles, C. J. Pollock, R. B. Torbert, and J. L. Burch. Wave-particle energy exchange directly observed in a kinetic Alfvén-branch wave. *Nature Communications*, 8:14719, March 2017. doi: 10.1038/ncomms14719.

R. G. Giovanelli. Magnetic and Electric Phenomena in the Sun's Atmosphere associated with Sunspots. *Monthly Notices of the Royal Astronomical Society*, 107(4):338–355, 11 1947.

M. V. Goldman, G. Lapenta, D. L. Newman, S. Markidis, and H. Che. Jet Deflection by Very Weak Guide Fields during Magnetic Reconnection. *Physical Review Letters*, 107(13):135001, September 2011. doi: 10.1103/PhysRevLett.107.135001.

J. T. Gosling, S. Eriksson, T. D. Phan, D. E. Larson, R. M. Skoug, and D. J. McComas. Direct evidence for prolonged magnetic reconnection at a continuous x-line within the heliospheric current sheet. *Geophys. Res. Lett.*, 34:L06102, March 2007. doi: 10.1029/2006GL029033.

C. C. Haggerty, M. A. Shay, J. F. Drake, T. D. Phan, and C. T. McHugh. The competition of electron and ion heating during magnetic reconnection. *Geophys. Res. Lett.*, 42:9657–9665, November 2015. doi: 10.1002/2015GL065961.

C. C. Haggerty, T. N. Parashar, W. H. Matthaeus, M. A. Shay, Y. Yang, M. Wan, P. Wu, and S. Servidio. Exploring the statistics of magnetic reconnection X-points in kinetic particle-in-cell turbulence. *Physics of Plasmas*, 24(10):102308, October 2017. doi: 10.1063/1.5001722.

A. Hasegawa and L. Chen. Kinetic process of plasma heating due to Alfvén wave excitation. *Physical Review Letters*, 35:370–373, August 1975. doi: 10.1103/PhysRevLett. 35.370.

C. T. Haynes, D. Burgess, and E. Camporeale. Reconnection and Electron Temperature Anisotropy in Sub-proton Scale Plasma Turbulence. *The Astrophysical Journal*, 783: 38, March 2014. doi: 10.1088/0004-637X/783/1/38.

M. Hesse and D. Winske. Hybrid simulations of collisionless ion tearing. *GRL*, 20: 1207–1210, June 1993. doi: 10.1029/93GL01250.

M. Hesse and D. Winske. Electron dissipation in collisionless magnetic reconnection. *JGR*, 103:26479–26486, November 1998. doi: 10.1029/98JA01570.

M. Hesse, K. Schindler, J. Birn, and M. Kuznetsova. The diffusion region in collisionless magnetic reconnection. *Phys. Plasmas*, 6:1781, 1999.

Michael Hesse and Seiji Zenitani. Dissipation in relativistic pair-plasma reconnection. *Physics of Plasmas*, 14(11):112102, 2007. doi: 10.1063/1.2801482. URL https://doi.org/10.1063/1.2801482.

Michael Hesse, Nicolas Aunai, David Sibeck, and Joachim Birn. On the electron diffusion region in planar, asymmetric, systems. *Geophysical Research Letters*, 41(24):8673–8680, 2014. doi: 10.1002/2014GL061586. URL https://agupubs.onlinelibrary.wiley.com/doi/abs/10.1002/2014GL061586.

R. Hodgson. On a curious Appearance seen in the Sun. *Monthly Notices of the Royal Astronomical Society*, 20:15–16, November 1859. doi: 10.1093/mnras/20.1.15.

E. W. Hones, Jr. Plasma flow in the magnetotail and its implications for substorm theories. In S.-I. Akasofu, editor, *Dynamics of the Magnetosphere*, pages 545–562, 1980.

E. W. Hones, Jr., S. J. Bame, and J. R. Asbridge. Proton flow measurements in the magnetotail plasma sheet made with Imp 6. *Journal of Geophysical Research*, 81: 227–234, January 1976. doi: 10.1029/JA081i001p00227.

R. Horiuchi and T. Sato. Particle simulation study of driven magnetic reconnection in a collisionless plasma. *Phys. Plasmas*, 1(11):3587, November 1994.

G. G. Howes, S. C. Cowley, W. Dorland, G. W. Hammett, E. Quataert, and A. A. Schekochihin. Astrophysical Gyrokinetics: Basic Equations and Linear Theory. *The Astrophysical Journal*, 651:590–614, November 2006. doi: 10.1086/506172.

J. D. Huba and L. I. Rudakov. Three-dimensional Hall magnetic reconnection. *Phys. Plasmas*, 9(11):4435–4438, 2002.

K.-J. Hwang, E. Choi, K. Dokgo, J. L. Burch, D. G. Sibeck, B. L. Giles, M. L. Goldstein, W. R. Paterson, C. J. Pollock, Q. Q. Shi, H. Fu, H. Hasegawa, D. J. Gershman, Y. Khotyaintsev, R. B. Torbert, R. E. Ergun, J. C. Dorelli, L. Avanov, C. T. Russell, and R. J. Strangeway. Electron vorticity indicative of the electron diffusion region of magnetic reconnection. *Geophysical Research Letters*, 0(0), 2019. doi: 10.1029/2019GL082710.

S. Imada, R. Nakamura, P. W. Daly, M. Hoshino, W. Baumjohann, S. Mühlbachler, A. Balogh, and H. RèMe. Energetic electron acceleration in the downstream reconnection outlow region. *Journal of Geophysical Research (Space Physics)*, 112:A03202, March 2007. doi: 10.1029/2006JA011847.

N. Jain, A. S. Sharma, L. M. Zelenyi, and H. V. Malova. Electron scale structures of thin current sheets in magnetic reconnection. *Annales Geophysicae*, 30:661–666, April 2012. doi: 10.5194/angeo-30-661-2012.

H. Karimabadi, D. Krauss-Vargan, N. Omidi, and H. X. Vu. Magnetic structure of the reconnection layer and core field generation in plasmoids. *J. Geophys. Res.*, 104 (A6):12313–12326, 1999.

H. Karimabadi, J. Dorelli, V. Roytershteyn, W. Daughton, and L. Chacón. Flux pileup in collisionless magnetic reconnection: Bursty interaction of large flux ropes. *Physical Review Letters*, 107(2):25002, 2011.

H. Karimabadi, V. Roytershteyn, M. Wan, W. H. Matthaeus, W. Daughton, P. Wu, M. Shay, B. Loring, J. Borovsky, E. Leonardis, S. C. Chapman, and T. K. M. Nakamura. Coherent structures, intermittent turbulence, and dissipation in high-temperature plasmas. *Phys. Plasmas*, 20(1):012303, January 2013. doi: 10.1063/1. 4773205.

A. Keiling, J. R. Wygant, C. A. Cattell, F. S. Mozer, and C. T. Russell. The Global Morphology of Wave Poynting Flux: Powering the Aurora. *Science*, 299:383–386, January 2003. doi: 10.1126/science.1080073.

L. Kepko, E. Spanswick, V. Angelopoulos, E. Donovan, J. McFadden, K.-H. Glassmeier, J. Raeder, and H. J. Singer. Equatorward moving auroral signatures of a flow burst observed prior to auroral onset. *Geophys. Res. Lett.*, 36:24104–+, December 2009. doi: 10.1029/2009GL041476.

Y. Khotyaintsev, S. Buchert, K. Stasiewicz, A. Vaivads, S. Savin, V. O. Papitashvili, C. J. Farrugia, B. Popielawska, and Y.-K. Tung. Transient reconnection in the cusp during strongly negative IMF $B_y$. *Journal of Geophysical Research (Space Physics)*, 109:A04204, April 2004. doi: 10.1029/2003JA009908.

Yu. V. Khotyaintsev, A. Vaivads, A. Retinò, M. André, C. J. Owen, and H. Nilsson. Formation of inner structure of a reconnection separatrix region. *Phys. Rev. Lett.*, 97:205003, Nov 2006. doi: 10.1103/PhysRevLett.97.205003. URL https://link. aps.org/doi/10.1103/PhysRevLett.97.205003.

K. G. Klein and G. G. Howes. Predicted impacts of proton temperature anisotropy on solar wind turbulence. *Physics of Plasmas*, 22(3):032903, March 2015. doi: 10.1063/1.4914933.

R. Kleva, J. Drake, and F. Waelbroeck. Fast reconnection in high temperature plasma. *Phys. Plasma*, 2:23, 1995.

Nicholas A. Krall and Alvin W. Trivelpiece. *Principles of Plasma Physics*. San Francisco Press, Inc., San Francisco, CA, 1986.

L. Landau. On the vibrations of the electronic plasma. *Journal of Physics*, 1946.

G. Lapenta, M. V. Goldman, D. L. Newman, and S. Markidis. Propagation speed of rotation signals for field lines undergoing magnetic reconnection. *Physics of Plasma(1994-present)*, 20(102113), 2013.

Y.-H. Liu, W. Daughton, H. Karimabadi, H. Li, and V. Roytershteyn. Bifurcated Structure of the Electron Diffusion Region in Three-Dimensional Magnetic Reconnection. *Physical Review Letters*, 110(26):265004, June 2013. doi: 10.1103/PhysRevLett.110. 265004.

Y.-H. Liu, W. Daughton, H. Karimabadi, H. Li, and S. Peter Gary. Do dispersive waves play a role in collisionless magnetic reconnection? *Physics of Plasmas*, 21(2): 022113, February 2014. doi: 10.1063/1.4865579.

Yi-Hsin Liu, M. Hesse, F. Guo, W. Daughton, H. Li, P. A. Cassak, and M. A. Shay. Why does steady-state magnetic reconnection have a maximum local rate of order 0.1? *Phys. Rev. Lett.*, 118:085101, Feb 2017. doi: 10.1103/PhysRevLett.118.085101. URL https://link.aps.org/doi/10.1103/PhysRevLett.118.085101.

A. T. Y. Lui. Current disruption in the earth's magnetosphere: Observations and models. *J. Geophys. Res.*, 101:13067, 1996.

A. T. Y. Lui. Comment on "Tail reconnection triggering substorm onset". *Science*, 324:1391–b, June 2009. doi: 10.1126/science.1167726.

L. R. Lyons and D. C. Pridmore Brown. Force balance near an x line in a collisionless plasma. *J. Geophys. Res.*, 95:20903, 1990.

R. L. Lysak and W. Lotko. On the kinetic dispersion relation for shear alfvén waves. *Geophys. Res. Lett.*, 101:5085–5094, 1996.

R. L. Lysak and Y. Song. Propagation of alfvén waves at the plasma sheet boundary layer. In T. Pulkinnen and N. Ganushkina, editors, *Substorms 7: Proceedings of the 7th International Conference on Substorms*, page 81. Finnish Meteorological Institute, 2004.

R. L. Lysak and Y. Song. Development of parallel electric fields at the plasma sheet boundary layer. *J. Geophys. Res.*, 116:A00K14, September 2011. doi: 10.1029/2010JA016424.

R. L. Lysak, Y. Song, and T. W. Jones. Propagation of Alfvén waves in the magnetotail during substorms. *Annales Geophysicae*, 27:2237–2246, May 2009. doi: 10.5194/angeo-27-2237-2009.

Z. W. Ma and A. Bhattacharjee. Fast impulsive reconnection and current sheet intensification due to electron pressure gradients in semi-collisional plasmas. *Geophys. Res. Lett.*, 23:1673, 1996.

A. Mallet, A. A. Schekochihin, and B. D. G. Chandran. Disruption of sheet-like structures in Alfvénic turbulence by magnetic reconnection. *Monthly Notices of the Royal Astronomical Society*, 468:4862–4871, July 2017. doi: 10.1093/mnras/stx670.

J. H. Malmberg and C. B. Wharton. Collisionless damping of electrostatic plasma waves. *Phys. Rev. Lett.*, 13:184–186, Aug 1964. doi: 10.1103/PhysRevLett.13.184. URL https://link.aps.org/doi/10.1103/PhysRevLett.13.184.

M. E. Mandt, R. E. Denton, and J. F. Drake. Transition to whistler mediated magnetic reconnection. *Geophys. Res. Lett.*, 21:73–76, January 1994. doi: 10.1029/93GL03382.

W. H. Matthaeus and S. L. Lamkin. Turbulent magnetic reconnection. *Physics of Fluids*, 29:2513–2534, August 1986. doi: 10.1063/1.866004.

W. H. Matthaeus, M. L. Goldstein, and D. A. Roberts. Evidence for the presence of quasi-two-dimensional nearly incompressible fluctuations in the solar wind. *Journal of Geophys. Res.*, 95:20673–20683, December 1990. doi: 10.1029/JA095iA12p20673.

P. A. Muñoz, D. Told, P. Kilian, J. Büchner, and F. Jenko. Gyrokinetic and kinetic particle-in-cell simulations of guide-field reconnection. i. macroscopic effects of the electron flows. *Physics of Plasmas*, 22(8):082110, 2015. doi: 10.1063/1.4928381. URL https://doi.org/10.1063/1.4928381.

T. Nagai, I. Shinohara, M. Fujimoto, M. Hoshino, Y. Saito, S. Machida, and T. Mukai. Geotail observations of the Hall current system: Evidence of magnetic reconnection in the magnetotail. *J. Geophys. Res.*, 106:25929–25950, November 2001. doi: 10.1029/2001JA900038.

T. K. M. Nakamura, K. J. Genestreti, Y.-H. Liu, R. Nakamura, W.-L. Teh, H. Hasegawa, W. Daughton, M. Hesse, R. B. Torbert, J. L. Burch, and B. L. Giles. Measurement of the magnetic reconnection rate in the earth's magnetotail. *Journal of Geophysical Research: Space Physics*, 123(11):9150–9168, 2018. doi: 10.1029/2018JA025713.

Y. Narita, K.-H. Glassmeier, M. L. Goldstein, U. Motschmann, and F. Sahraoui. Three-dimensional spatial structures of solar wind turbulence from 10 000-km to 100-km scales. *Annales Geophysicae*, 29:1731–1738, October 2011. doi: 10.5194/angeo-29-1731-2011.

A. Nishida, H. Hayakawa, and E. W. Hones Jr. Observed signatures of reconnection in the magnetotail. *Journal of Geophysical Research: Space Physics*, 86(A3):1422–1436, 1981. doi: 10.1029/JA086iA03p01422. URL https://agupubs.onlinelibrary.wiley.com/doi/abs/10.1029/JA086iA03p01422.

Y. Nishimura, L. Lyons, S. Zou, V. Angelopoulos, and S. Mende. Substorm triggering by new plasma intrusion: THEMIS all-sky imager observations. *J. Geophys. Res.*, 115(A14):7222, July 2010. doi: 10.1029/2009JA015166.

M. Oieroset, T. D. Phan, M. Fujimoto, R. P. Lin, and R. P. Lepping. In situ detection of collisionless reconnection in the earth's magnetotail. *Nature*, 412:417, 2001.

M. Øieroset, T. D. Phan, J. F. Drake, J. P. Eastwood, S. A. Fuselier, R. J. Strangeway, C. Haggerty, M. A. Shay, M. Oka, S. Wang, L.-J. Chen, I. Kacem, B. Lavraud, V. Angelopoulos, J. L. Burch, R. B. Torbert, R. E. Ergun, Y. Khotyaintsev, P. A. Lindqvist, D. J. Gershman, B. L. Giles, C. Pollock, T. E. Moore, C. T. Russell, Y. Saito, L. A. Avanov, and W. Paterson. Reconnection with magnetic flux pileup at the interface of converging jets at the magnetopause. *Geophysical Research Letters*, 46(4):1937–1946, 2019. doi: 10.1029/2018GL080994. URL https://agupubs.onlinelibrary.wiley.com/doi/abs/10.1029/2018GL080994.

S. Oughton, E. R. Priest, and W. H. Matthaeus. The influence of a mean magnetic field on three-dimensional MHD turbulence. *J. Fluid Mechanics*, 280:95, 1994.

Emanuele Papini, Luca Franci, Simone Landi, Andrea Verdini, Lorenzo Matteini, and Petr Hellinger. Can Hall Magnetohydrodynamics explain plasma turbulence at sub-ion scales? *arXiv e-prints*, art. arXiv:1810.02210, October 2018.

E. N. Parker. Sweet's mechanism for merging magnetic fields in conducting fluids. *J. Geophys. Res.*, 62:509, 1957.

G. Paschmann, I. Papamastorakis, N. Sckopke, G. Haerendel, B. U. O. Sonnerup, S. J. Bame, J. R. Asbridge, J. T. Gosling, C. T. Russel, and R. C. Elphic. Plasma acceleration at the earth's magnetopause - Evidence for reconnection. *Nature*, 282: 243–246, November 1979. doi: 10.1038/282243a0.

H. E. Petschek. Magnetic field annihilation. In W. N. Ness, editor, *AAS/NASA Symposium on the Physics of Solar Flares*, page 425. NASA, Washington, DC, 1964.

T. D. Phan, J. T. Gosling, M. S. Davis, R. M. Skoug, M. Øieroset, R. P. Lin, R. P. Lepping, D. J. McComas, C. W. Smith, H. Reme, and A. Balogh. A magnetic reconnection X-line extending more than 390 Earth radii in the solar wind. *Nature*, 439:175–178, January 2006. doi: 10.1038/nature04393.

T. D. Phan, J. F. Drake, M. A. Shay, F. S. Mozer, and J. P. Eastwood. Evidence for an elongated (> 60 ion skin depths) electron diffusion region during fast magnetic reconnection. *Phys. Rev. Lett.*, 99:255002, 2007.

T. D. Phan, M. A. Shay, J. T. Gosling, M. Fujimoto, J. F. Drake, G. Paschmann, M. Oieroset, J. P. Eastwood, and V. Angelopoulos. Electron bulk heating in magnetic reconnection at Earth's magnetopause: Dependence on the inflow Alfvén speed and magnetic shear. *Geophys. Res. Lett.*, 40:4475–4480, September 2013. doi: 10.1002/grl.50917.

T. D. Phan, J. F. Drake, M. A. Shay, J. T. Gosling, G. Paschmann, J. P. Eastwood, M. Oieroset, M. Fujimoto, and V. Angelopoulos. Ion bulk heating in magnetic reconnection exhausts at Earth's magnetopause: Dependence on the inflow Alfvén speed and magnetic shear angle. *Geophys. Res. Lett.*, 41:7002–7010, October 2014. doi: 10.1002/2014GL061547.

T. D. Phan, J. P. Eastwood, M. A. Shay, J. F. Drake, B. U. Ö. Sonnerup, M. Fujimoto, P. A. Cassak, M. Øieroset, J. L. Burch, R. B. Torbert, A. C. Rager, J. C. Dorelli, D. J. Gershman, C. Pollock, P. S. Pyakurel, C. C. Haggerty, Y. Khotyaintsev, B. Lavraud, Y. Saito, M. Oka, R. E. Ergun, A. Retino, O. Le Contel, M. R. Argall, B. L. Giles, T. E. Moore, F. D. Wilder, R. J. Strangeway, C. T. Russell, P. A. Lindqvist, and W. Magnes. Electron magnetic reconnection without ion coupling in Earth's turbulent magnetosheath. *Nature*, 557:202–206, May 2018. doi: 10.1038/s41586-018-0091-5.

T. D. Phan et al. Extended magnetic reconnection at the earth's magnetopause from detection of bi-directional jets. *Nature*, 404:848, 2000.

E. R. Priest, G. Hornig, and D. I. Pontin. On the nature of three-dimensional magnetic reconnection. *Journal of Geophysical Research (Space Physics)*, 108:1285, July 2003. doi: 10.1029/2002JA009812.

P. L. Pritchett. Collisionless magnetic reconnection in a three-dimensional open system. *J. Geophys. Res.*, 106(A11):25961, 2001.

P. L. Pritchett and F. V. Coroniti. Three-dimensional collisionless magnetic reconnection in the presence of a guide field. *J. Geophys. Res.*, 109: 1220,doi10.1029/2003JA009999, 2004.

P. S. Pyakurel, M. A. Shay, C. C. Haggerty, T. N. Parashar, J. F. Drake, P. A. Cassak, and S. Peter Gary. Super-alfvénic propagation and damping of reconnection onset signatures. *Journal of Geophysical Research: Space Physics*, 123(1):341–349, 2018. doi: 10.1002/2017JA024606.

A. C. Rager, J. C. Dorelli, D. J. Gershman, V. Uritsky, L. A. Avanov, R. B. Torbert, J. L. Burch, R. E. Ergun, J. Egedal, C. Schiff, J. R. Shuster, B. L. Giles, W. R. Paterson, C. J. Pollock, R. J. Strangeway, C. T. Russell, B. Lavraud, V. N. Coffey, and Y. Saito. Electron Crescent Distributions as a Manifestation of Diamagnetic Drift in an Electron-Scale Current Sheet: Magnetospheric Multiscale Observations Using New 7.5 ms Fast Plasma Investigation Moments. *GRL*, 45:578–584, January 2018. doi: 10.1002/2017GL076260.

A. Retinò, M. B. Bavassano Cattaneo, M. F. Marcucci, A. Vaivads, M. André, Y. Khotyaintsev, T. Phan, G. Pallocchia, H. Rème, E. Möbius, B. Klecker, C. W. Carlson, M. McCarthy, A. Korth, R. Lundin, and A. Balogh. Cluster multispacecraft observations at the high-latitude duskside magnetopause: implications for continuous and component magnetic reconnection. *Annales Geophysicae*, 23:461–473, February 2005. doi: 10.5194/angeo-23-461-2005.

A. Retinò, D. Sundkvist, A. Vaivads, F. Mozer, M. André, and C. J. Owen. In situ evidence of magnetic reconnection in turbulent plasma. *Nature Physics*, 3:236–238, April 2007. doi: 10.1038/nphys574.

B. N. Rogers, R. E. Denton, J. F. Drake, and M. A. Shay. Role of dispersive waves in collisionless magnetic reconnection. *Phys. Rev. Lett.*, 87(19):195004, 2001.

F. Sahraoui, M. L. Goldstein, G. Belmont, P. Canu, and L. Rezeau. Three Dimensional Anisotropic k Spectra of Turbulence at Subproton Scales in the Solar Wind. *Physical Review Letters*, 105(13):131101, September 2010. doi: 10.1103/PhysRevLett.105. 131101.

A. A. Schekochihin, S. C. Cowley, W. Dorland, G. W. Hammett, G. G. Howes, E. Quataert, and T. Tatsuno. ASTROPHYSICAL GYROKINETICS: KINETIC AND FLUID TURBULENT CASCADES IN MAGNETIZED WEAKLY COLLISIONAL PLASMAS. *The Astrophysical Journal Supplement Series*, 182(1):310–377, may 2009. doi: 10.1088/0067-0049/182/1/310.

S. Servidio, W. H. Matthaeus, M. A. Shay, P. A. Cassak, and P. Dmitruk. Magnetic reconnection in two-dimensional magnetohydrodynamic turbulence. *Phys. Rev. Letters*, 102:115003, 2009.

S. Servidio, W. H. Matthaeus, M. A. Shay, P. Dmitruk, P. A. Cassak, and M. Wan. Statistics of magnetic reconnection in two-dimensional magnetohydrodynamic turbulence. *Phys. Plasma*, 17:032315, 2010.

P. Sharma Pyakurel, M. A. Shay, T. D. Phan, W. H. Matthaeus, J. F. Drake, J. M. TenBarge, C. C. Haggerty, P. A. K. Klein, and Cassak, T. N. Parashar, M. Swisdak, and A. Chasapis. Transition from ion-coupled to electron-only reconnection: Basic physics and implications for plasma turbulence. *Physics of Plasmas*, 2019.

M. A. Shay and J. F. Drake. The role of electron dissipation on the rate of collisionless magnetic reconnection. *Geophys. Res. Lett.*, 25:3759, 1998.

M. A. Shay, J. F. Drake, R. E. Denton, and D. Biskamp. Structure of the dissipation region during collisionless magnetic reconnection. *J. Geophys. Res.*, 103:9165, 1998.

M. A. Shay, J. F. Drake, B. N. Rogers, and R. E. Denton. The scaling of collisionless, magnetic reconnection for large systems. *Geophys. Res. Lett.*, 26:2163, 1999.

M. A. Shay, J. F. Drake, B. N. Rogers, and R. E. Denton. Alfvénic collisionless reconnection and the Hall term. *J. Geophys. Res.*, 106:3759, 2001a.

M. A. Shay, J. F. Drake, B. N. Rogers, and M. Swisdak. The three dimensional nature of reconnection. *Eos. Trans. AGU*, 82(47), 2001b. Fall Meet. Suppl., Abstract SM21A-0772.

M. A. Shay, J. F. Drake, M. Swisdak, W. Dorland, and B. N. Rogers. Inherently three-dimensional magnetic reconnection: A mechanism for bursty bulk flows? *Geophys. Res. Lett.*, 30(6):1345, doi:10.1029/2002GL016267, 2003.

M. A. Shay, J. F. Drake, and M. Swisdak. Two-scale structure of the electron dissipation region during collisionless magnetic reconnection. *Phys. Rev. Lett.*, 99:155002, 2007.

M. A. Shay, J. F. Drake, J. P. Eastwood, and T. D. Phan. Super-Alfvénic Propagation of Substorm Reconnection Signatures and Poynting Flux. *Phys. Rev. Lett.*, 107(6): 065001, August 2011. doi: 10.1103/PhysRevLett.107.065001.

M. A. Shay, C. C. Haggerty, T. D. Phan, J. F. Drake, P. A. Cassak, P. Wu, M. Oieroset, M. Swisdak, and K. Malakit. Electron heating during magnetic reconnection: A simulation scaling study. *Physics of Plasmas*, 21(12):122902, December 2014. doi: 10.1063/1.4904203.

M. A. Shay, C. C. Haggerty, W. H. Matthaeus, T. N. Parashar, M. Wan, and P. Wu. Turbulent heating due to magnetic reconnection. *Physics of Plasmas*, 25(1):012304, 2018. doi: 10.1063/1.4993423.

B. U. Ö. Sonnerup. Magnetic field reconnection. In L. J. Lanzerotti, C. F. Kennel, and E. N. Parker, editors, *Solar System Plasma Physics*, volume 3, page 46. North Halland Pub., Amsterdam, 1979.

T. W. Speiser. Particle Trajectories in Model Current Sheets, 1, Analytical Solutions. *Journal of Geophysical Research*, 70:4219–4226, September 1965. doi: 10.1029/JZ070i017p04219.

A. Stanier, Andrei N. Simakov, L. Chacón, and W. Daughton. Fluid vs. kinetic magnetic reconnection with strong guide fields. *Physics of Plasmas*, 22(10):101203, 2015. doi: 10.1063/1.4932330. URL https://doi.org/10.1063/1.4932330.

T. H. Stix. *Waves in Plasmas.* American Institute of Physics, New York, 1992.

X. Sun, T. P. Intrator, L. Dorf, J. Sears, I. Furno, and G. Lapenta. Flux rope dynamics: Experimental study of bouncing and merging. *Phys. Rev. Lett.*, 105:255001, Dec 2010. doi: 10.1103/PhysRevLett.105.255001. URL https://link.aps.org/doi/10.1103/PhysRevLett.105.255001.

D. Sundkvist, A. Retino, A. Vaivads, and S. D. Bale. Dissipation in turbulent plasma due to reconnection in thin current sheets. *Phys. Rev. Lett.*, 99:025004, 2007. doi: 10.1103/PhysRevLett.99.025004.

P. A. Sweet. The neutral point theory of solar flares. In B. Lehnert, editor, *Electromagnetic Phenomena in Cosmical Physics*, page 123. Cambridge University Press, New York, 1958.

M. Swisdak, J. F. Drake, J. G. McIlhargey, and M. A. Shay. The transition from anti-parallel to component magnetic reconnection. *J. Geophys. Res.*, 110:A05210, 2005. doi: 10.1029/2004JA010748.

M. Swisdak, Yi-Hsin Liu, and J. F. Drake. Development of a turbulent outflow during electron-positron magnetic reconnection. *The Astrophysical Journal*, 680(2):999–1008, jun 2008. doi: 10.1086/588088.

S. I. Syrovatsky. Formation of current sheets in a plasma with a frozen-in strong magnetic field. *Sov. Phys. JETP*, 33:933, 1971.

J. M. TenBarge and G. G. Howes. Evidence of critical balance in kinetic Alfvén wave turbulence simulations a). *Physics of Plasmas*, 19(5):055901, May 2012. doi: 10.1063/1.3693974.

J. M. TenBarge, W. Daughton, H. Karimabadi, G. G. Howes, and W. Dorland. Collisionless reconnection in the large guide field regime: Gyrokinetic versus particle-in-cell simulations. *Physics of Plasmas*, 21(2):020708, 2014. doi: 10.1063/1.4867068. URL https://doi.org/10.1063/1.4867068.

T. Terasawa. Hall current effect on tearing mode instability. *Geophys. Res. Lett.*, 10: 475, 1983.

Masayuki Ugai and Takao Tsuda. Magnetic field-line reconnexion by localized enhancement of resistivity: Part 1. evolution in a compressible mhd fluid. *Journal of Plasma Physics*, 17(3):337–356, 1977. doi: 10.1017/S0022377800020663.

A. Vaivads, Y. Khotyaintsev, M. André, A. Retinò, S. C. Buchert, B. N. Rogers, P. Décréau, G. Paschmann, and T. D. Phan. Structure of the Magnetic Reconnection Diffusion Region from Four-Spacecraft Observations. *Physical Review Letters*, 93 (10):105001–+, August 2004. doi: 10.1103/PhysRevLett.93.105001.

V. M. Vasyliunas. Theoretical models of magnetic field line merging, 1. *Rev. Geophys.*, 13(1):303, Feb. 1975.

Daniel Verscharen, Sofiane Bourouaine, Benjamin D. G. Chandran, and Bennett A. Maruca. A PARALLEL-PROPAGATING ALFVéNIC ION-BEAM INSTABILITY IN THE HIGH-BETA SOLAR WIND. *The Astrophysical Journal*, 773(1):8, jul 2013. doi: 10.1088/0004-637x/773/1/8.

Z. Vörös, E. Yordanova, A. Varsani, K. J. Genestreti, Yu. V. Khotyaintsev, W. Li, D. B. Graham, C. Norgren, R. Nakamura, Y. Narita, F. Plaschke, W. Magnes, W. Baumjohann, D. Fischer, A. Vaivads, E. Eriksson, P.-A. Lindqvist, G. Marklund, R. E. Ergun, M. Leitner, M. P. Leubner, R. J. Strangeway, O. LeContel, C. Pollock, B. J.

Giles, R. B. Torbert, J. L. Burch, L. A. Avanov, J. C. Dorelli, D. J. Gershman, W. R. Paterson, B. Lavraud, and Y. Saito. Mms observation of magnetic reconnection in the turbulent magnetosheath. *Journal of Geophysical Research: Space Physics*, 122 (11):11,442–11,467, 2017. doi: 10.1002/2017JA024535.

M. Wan, A. F. Rappazzo, W. H. Matthaeus, S. Servidio, and S. Oughton. Dissipation and reconnection in boundary-driven reduced magnetohydrodynamics. *Astrophys. J.*, 797:63, 2014. doi: 10.1088/0004-637X/797/1/63.

C. E. J. Watt and R. Rankin. Electron Trapping in Shear Alfvén Waves that Power the Aurora. *Physical Review Letters*, 102(4):045002, January 2009. doi: 10.1103/ PhysRevLett.102.045002.

C. E. J. Watt and R. Rankin. Do magnetospheric shear Alfvén waves generate sufficient electron energy flux to power the aurora? *Journal of Geophysical Research (Space Physics)*, 115:A07224, July 2010. doi: 10.1029/2009JA015185.

F. D. Wilder, R. E. Ergun, S. Eriksson, T. D. Phan, J. L. Burch, N. Ahmadi, K. A. Goodrich, D. L. Newman, K. J. Trattner, R. B. Torbert, B. L. Giles, R. J. Strangeway, W. Magnes, P.-A. Lindqvist, and Yu-V. Khotyaintsev. Multipoint measurements of the electron jet of symmetric magnetic reconnection with a moderate guide field. *Phys. Rev. Lett.*, 118:265101, Jun 2017. doi: 10.1103/PhysRevLett.118.265101. URL https://link.aps.org/doi/10.1103/PhysRevLett.118.265101.

J. R. Wygant, C. A. Cattell, R. Lysak, Y. Song, J. Dombeck, J. McFadden, F. S. Mozer, C. W. Carlson, G. Parks, E. A. Lucek, A. Balogh, M. Andre, H. Reme, M. Hesse, and C. Mouikis. Cluster observations of an intense normal component of the electric field at a thin reconnecting current sheet in the tail and its role in the shock-like acceleration of ions fluid into the separatrix region. *J. Geophys. Res.*, 110:A09206, doi:10.1029/2004JA010708, 2005.

M. Yamada, R. Kulsrud, and H. Ji. Magnetic reconnection. *Rev. Modern Phys.*, 82: 603, January 2010. doi: 10.1103/RevModPhys.82.603.

E. Yordanova, Z. Vörös, A. Varsani, D. B. Graham, C. Norgren, Y. V. Khotyaintsev, A. Vaivads, E. Eriksson, R. Nakamura, P.-A. Lindqvist, G. Marklund, R. E. Ergun, W. Magnes, W. Baumjohann, D. Fischer, F. Plaschke, Y. Narita, C. T. Russell, R. J. Strangeway, O. Le Contel, C. Pollock, R. B. Torbert, B. J. Giles, J. L. Burch, L. A. Avanov, J. C. Dorelli, D. J. Gershman, W. R. Paterson, B. Lavraud, and Y. Saito. Electron scale structures and magnetic reconnection signatures in the turbulent magnetosheath. *Geophysical Research Letters*, 43:5969–5978, June 2016. doi: 10.1002/2016GL069191.

A. Zeiler, D. Biskamp, J. F. Drake, B. N. Rogers, M. A. Shay, and M. Scholer. Three-dimensional particle simulations of collisionless magnetic reconnection. *J. Geophys. Res.*, 107:1230, 2002. doi:10.1029/2001JA000287.

V. Zhdankin, D. A. Uzdensky, J. C. Perez, and S. Boldyrev. Statistical Analysis of Current Sheets in Three-dimensional Magnetohydrodynamic Turbulence. *Astrophy. J.*, 771:124, July 2013. doi: 10.1088/0004-637X/771/2/124.

# Appendix

# PERMISSION

## JOHN WILEY AND SONS LICENSE
## TERMS AND CONDITIONS

Jul 24, 2019

This Agreement between University of Delaware -- Prayash Sharma Pyakurel ("You") and John Wiley and Sons ("John Wiley and Sons") consists of your license details and the terms and conditions provided by John Wiley and Sons and Copyright Clearance Center.

| | |
|---|---|
| License Number | 4635381421740 |
| License date | Jul 24, 2019 |
| Licensed Content Publisher | John Wiley and Sons |
| Licensed Content Publication | Journal of Geophysical Research: Space Physics |
| Licensed Content Title | Super-Alfvénic Propagation and Damping of Reconnection Onset Signatures |
| Licensed Content Author | P. Sharma Pyakurel, M. A. Shay, C. C. Haggerty, et al |
| Licensed Content Date | Jan 15, 2018 |
| Licensed Content Volume | 123 |
| Licensed Content Issue | 1 |
| Licensed Content Pages | 9 |
| Type of use | Dissertation/Thesis |
| Requestor type | Author of this Wiley article |
| Format | Electronic |
| Portion | Full article |
| Will you be translating? | Yes, without English rights |
| Number of languages | 1 |
| Languages | English |
| Title of your thesis / dissertation | Ion-Coupling During Collisionless Magnetic Reconnection: Causes and Consequences |
| Expected completion date | Aug 2019 |
| Expected size (number of pages) | 160 |
| Requestor Location | University of Delaware 104 The Green |
| | NEWARK, DE 19716 United States Attn: Dr. |
| Publisher Tax ID | EU826007151 |

145

Total                    0.00 USD

Terms and Conditions

## TERMS AND CONDITIONS

This copyrighted material is owned by or exclusively licensed to John Wiley & Sons, Inc. or one of its group companies (each a"Wiley Company") or handled on behalf of a society with which a Wiley Company has exclusive publishing rights in relation to a particular work (collectively "WILEY"). By clicking "accept" in connection with completing this licensing transaction, you agree that the following terms and conditions apply to this transaction (along with the billing and payment terms and conditions established by the Copyright Clearance Center Inc., ("CCC's Billing and Payment terms and conditions"), at the time that you opened your RightsLink account (these are available at any time at http://myaccount.copyright.com).

**Terms and Conditions**

- The materials you have requested permission to reproduce or reuse (the "Wiley Materials") are protected by copyright.

- You are hereby granted a personal, non-exclusive, non-sub licensable (on a stand-alone basis), non-transferable, worldwide, limited license to reproduce the Wiley Materials for the purpose specified in the licensing process. This license, **and any CONTENT (PDF or image file) purchased as part of your order,** is for a one-time use only and limited to any maximum distribution number specified in the license. The first instance of republication or reuse granted by this license must be completed within two years of the date of the grant of this license (although copies prepared before the end date may be distributed thereafter). The Wiley Materials shall not be used in any other manner or for any other purpose, beyond what is granted in the license. Permission is granted subject to an appropriate acknowledgement given to the author, title of the material/book/journal and the publisher. You shall also duplicate the copyright notice that appears in the Wiley publication in your use of the Wiley Material. Permission is also granted on the understanding that nowhere in the text is a previously published source acknowledged for all or part of this Wiley Material. Any third party content is expressly excluded from this permission.

- With respect to the Wiley Materials, all rights are reserved. Except as expressly granted by the terms of the license, no part of the Wiley Materials may be copied, modified, adapted (except for minor reformatting required by the new Publication), translated, reproduced, transferred or distributed, in any form or by any means, and no derivative works may be made based on the Wiley Materials without the prior permission of the respective copyright owner.**For STM Signatory Publishers clearing permission under the terms of the STM Permissions Guidelines only, the terms of the license are extended to include subsequent editions and for editions in other languages, provided such editions are for the work as a whole in situ and does not involve the separate exploitation of the permitted figures or extracts,** You may not alter, remove or suppress in any manner any copyright, trademark or other notices displayed by the Wiley Materials. You may not license, rent, sell, loan, lease, pledge, offer as security, transfer or assign the Wiley Materials on a stand-alone

146

basis, or any of the rights granted to you hereunder to any other person.

- The Wiley Materials and all of the intellectual property rights therein shall at all times remain the exclusive property of John Wiley & Sons Inc, the Wiley Companies, or their respective licensors, and your interest therein is only that of having possession of and the right to reproduce the Wiley Materials pursuant to Section 2 herein during the continuance of this Agreement. You agree that you own no right, title or interest in or to the Wiley Materials or any of the intellectual property rights therein. You shall have no rights hereunder other than the license as provided for above in Section 2. No right, license or interest to any trademark, trade name, service mark or other branding ("Marks") of WILEY or its licensors is granted hereunder, and you agree that you shall not assert any such right, license or interest with respect thereto

- NEITHER WILEY NOR ITS LICENSORS MAKES ANY WARRANTY OR REPRESENTATION OF ANY KIND TO YOU OR ANY THIRD PARTY, EXPRESS, IMPLIED OR STATUTORY, WITH RESPECT TO THE MATERIALS OR THE ACCURACY OF ANY INFORMATION CONTAINED IN THE MATERIALS, INCLUDING, WITHOUT LIMITATION, ANY IMPLIED WARRANTY OF MERCHANTABILITY, ACCURACY, SATISFACTORY QUALITY, FITNESS FOR A PARTICULAR PURPOSE, USABILITY, INTEGRATION OR NON-INFRINGEMENT AND ALL SUCH WARRANTIES ARE HEREBY EXCLUDED BY WILEY AND ITS LICENSORS AND WAIVED BY YOU.

- WILEY shall have the right to terminate this Agreement immediately upon breach of this Agreement by you.

- You shall indemnify, defend and hold harmless WILEY, its Licensors and their respective directors, officers, agents and employees, from and against any actual or threatened claims, demands, causes of action or proceedings arising from any breach of this Agreement by you.

- IN NO EVENT SHALL WILEY OR ITS LICENSORS BE LIABLE TO YOU OR ANY OTHER PARTY OR ANY OTHER PERSON OR ENTITY FOR ANY SPECIAL, CONSEQUENTIAL, INCIDENTAL, INDIRECT, EXEMPLARY OR PUNITIVE DAMAGES, HOWEVER CAUSED, ARISING OUT OF OR IN CONNECTION WITH THE DOWNLOADING, PROVISIONING, VIEWING OR USE OF THE MATERIALS REGARDLESS OF THE FORM OF ACTION, WHETHER FOR BREACH OF CONTRACT, BREACH OF WARRANTY, TORT, NEGLIGENCE, INFRINGEMENT OR OTHERWISE (INCLUDING, WITHOUT LIMITATION, DAMAGES BASED ON LOSS OF PROFITS, DATA, FILES, USE, BUSINESS OPPORTUNITY OR CLAIMS OF THIRD PARTIES), AND WHETHER OR NOT THE PARTY HAS BEEN ADVISED OF THE POSSIBILITY OF SUCH DAMAGES. THIS LIMITATION SHALL APPLY NOTWITHSTANDING ANY FAILURE OF ESSENTIAL PURPOSE OF ANY LIMITED REMEDY PROVIDED HEREIN.

- Should any provision of this Agreement be held by a court of competent jurisdiction to be illegal, invalid, or unenforceable, that provision shall be deemed amended to achieve as nearly as possible the same economic effect as the original provision, and the legality, validity and enforceability of the remaining provisions of this Agreement shall not be affected or impaired thereby.

- The failure of either party to enforce any term or condition of this Agreement shall not constitute a waiver of either party's right to enforce each and every term and condition of this Agreement. No breach under this agreement shall be deemed waived or excused by either party unless such waiver or consent is in writing signed by the party granting such waiver or consent. The waiver by or consent of a party to a breach of any provision of this Agreement shall not operate or be construed as a waiver of or consent to any other or subsequent breach by such other party.

- This Agreement may not be assigned (including by operation of law or otherwise) by you without WILEY's prior written consent.

- Any fee required for this permission shall be non-refundable after thirty (30) days from receipt by the CCC.

- These terms and conditions together with CCC's Billing and Payment terms and conditions (which are incorporated herein) form the entire agreement between you and WILEY concerning this licensing transaction and (in the absence of fraud) supersedes all prior agreements and representations of the parties, oral or written. This Agreement may not be amended except in writing signed by both parties. This Agreement shall be binding upon and inure to the benefit of the parties' successors, legal representatives, and authorized assigns.

- In the event of any conflict between your obligations established by these terms and conditions and those established by CCC's Billing and Payment terms and conditions, these terms and conditions shall prevail.

- WILEY expressly reserves all rights not specifically granted in the combination of (i) the license details provided by you and accepted in the course of this licensing transaction, (ii) these terms and conditions and (iii) CCC's Billing and Payment terms and conditions.

- This Agreement will be void if the Type of Use, Format, Circulation, or Requestor Type was misrepresented during the licensing process.

- This Agreement shall be governed by and construed in accordance with the laws of the State of New York, USA, without regards to such state's conflict of law rules. Any legal action, suit or proceeding arising out of or relating to these Terms and Conditions or the breach thereof shall be instituted in a court of competent jurisdiction in New York County in the State of New York in the United States of America and each party hereby consents and submits to the personal jurisdiction of such court, waives any objection to venue in such court and consents to service of process by registered or

certified mail, return receipt requested, at the last known address of such party.

**WILEY OPEN ACCESS TERMS AND CONDITIONS**
Wiley Publishes Open Access Articles in fully Open Access Journals and in Subscription journals offering Online Open. Although most of the fully Open Access journals publish open access articles under the terms of the Creative Commons Attribution (CC BY) License only, the subscription journals and a few of the Open Access Journals offer a choice of Creative Commons Licenses. The license type is clearly identified on the article.
**The Creative Commons Attribution License**
The Creative Commons Attribution License (CC-BY) allows users to copy, distribute and transmit an article, adapt the article and make commercial use of the article. The CC-BY license permits commercial and non-
**Creative Commons Attribution Non-Commercial License**
The Creative Commons Attribution Non-Commercial (CC-BY-NC)License permits use, distribution and reproduction in any medium, provided the original work is properly cited and is not used for commercial purposes.(see below)

**Creative Commons Attribution-Non-Commercial-NoDerivs License**
The Creative Commons Attribution Non-Commercial-NoDerivs License (CC-BY-NC-ND) permits use, distribution and reproduction in any medium, provided the original work is properly cited, is not used for commercial purposes and no modifications or adaptations are made. (see below)
**Use by commercial "for-profit" organizations**
Use of Wiley Open Access articles for commercial, promotional, or marketing purposes requires further explicit permission from Wiley and will be subject to a fee.
Further details can be found on Wiley Online Library
http://olabout.wiley.com/WileyCDA/Section/id-410895.html

**Other Terms and Conditions:**

**v1.10 Last updated September 2015**

**Questions? customercare@copyright.com or +1-855-239-3415 (toll free in the US) or +1-978-646-2777.**

149